Fe-N-C SINGLE-ATOMIC SITE CATALYSTS: ENZYME-LIKE ACTIVITIES AND

BIOSENSING APPLICATIONS

By

ZHAOYUAN LYU

A dissertation submitted in partial fulfillment of
the requirements for the degree of

DOCTOR OF PHILOSOPHY

WASHINGTON STATE UNIVERSITY
School of Mechanical and Materials Engineering

MAY 2022

To the Faculty of Washington State University:

  The members of the Committee appointed to examine the dissertation of ZHAOYUAN LYU find it satisfactory and recommend that it be accepted.

<div style="text-align: right;">

_____

Yuehe Lin, Ph.D., Chair

_____

Scott Beckman, Ph.D.

_____

Kaiyan Qiu, Ph.D.

</div>

Fe-N-C SINGLE-ATOMIC SITE CATALYSTS: ENZYME-LIKE ACTIVITIES AND

BIOSENSING APPLICATIONS

Abstract

by Zhaoyuan Lyu, Ph.D.
Washington State University
May 2022

Chair: Yuehe Lin

From diagnosis of life-threatening diseases to detection of biological agents in the human body

and environment, biosensors are becoming a critical part of modern life. The fast detection

process and accurate detection results have posed high requirements in the sensitivity and

specificity of the biosensors. Recently, some nanomaterials have been found to possess

unexpected peroxidase-like activities, and great progress has been made to fabricate colorimetric

biosensors based on the peroxidase-like activities of these nanomaterials. These nanomaterials

exhibit flexibility in structural design and composition, easy separation and storage, high

stability, simple preparation, and tunable catalytic activity. Fe-based single-atomic site catalysts

(SASCs), with the natural metalloproteases-like active site structure, have attracted widespread

attention in biosensing applications. Precisely controlling the isolated single-atomic Fe-N-C

active site density and structure is crucial to improving the SASCs' performance.

In this dissertation, different strategies are used to increase the enzyme-like activity of Fe-N-C

SASCs. Using ion-imprinting technology to precisely control ions at the atomic level, form

numerous well-defined single-atomic Fe-N-C sites, and achieve in situ detection of H_2O_2

generated from cells. The use of nanoconfinement force can greatly increase the number of Fe-N_x active sites in the material, thereby greatly improving the enzyme-like properties of the material, which can then be used for biosensing and sensitive and selective detection of disease biomarkers. Furthermore, harnessing the advantages of two-dimensional (2D) materials to synthesize SASCs can further enhance their activity, as the 2D structure can help expose more single-atomic sites that can directly participate in the reaction. This strategy has been successfully used to fabricate biosensing systems for herbicide detection. More importantly, different SASCs can be further designed by using appropriate precursors to achieve structural mimicry of the natural enzyme, through control size and morphology to achieve point-of-care detection via lateral-flow immunoassay.

Fe-N-C SASCs synthesized in this work have significant potential to replace natural enzymes for high-sensitive biosensing applications. Their unique single-atomic geometrical structure exhibits significant advantages in biocatalytic activity, stability, and selectivity. We believe the continuously developed strategies can enable the Fe-N-C SASCs to explore their wider applications in various biosensing applications with excellent detection performance.

TABLE OF CONTENTS

APPENDIX

LIST OF TABLES

Page

Dedication

To my dear parents, sister, and my lifelong beloved husband Shichao

CHAPTER ONE: INTRODUCTION

Over the years, the development of highly sensitive biosensors has received increasing attention, and some major breakthroughs in biosensing have been recognized due to the application of nanomaterials with enzyme-like properties that can amplify signals. In which Single-atomic site catalysts (SASCs), containing atomically dispersed metal active sites, holding great promise in biosensors.

1.1 Introduction of biosensors

A biosensor is an analytical device consisting of biological elements, biological receptors, and physicochemical detectors for the detection of chemical substances in biosensing applications. It combines biological elements and physicochemical detectors to convert biological reactions into optical, electrical, and other detectable signals, electrochemical and colorimetric signals.[1-3] Biomolecules capable of detecting or recognizing target analytes, such as antibodies, aptamers, enzymes, nucleic acids or cells, are used as biological receptors. These sensors have advantages such as high selectivity towards the target analyte, this is due to the specific interaction between the biological receptors present in their structure and the target analyte.[4]

Figure 1.1[5] shows the schematic diagram of biosensors. The first biosensor was invented by Clark Jr. in 1956 to continuously detect oxygen in the blood during cardiopulmonary bypass surgery,[6, 7] the mechanism was that the oxygen could be reduced on a metal electrode by the gas permeable membrane. Clark also built the first prototype glucose sensor in 1962 using glucose oxidase.[8] Since then, numerous efforts have been put into developing various biosensors.
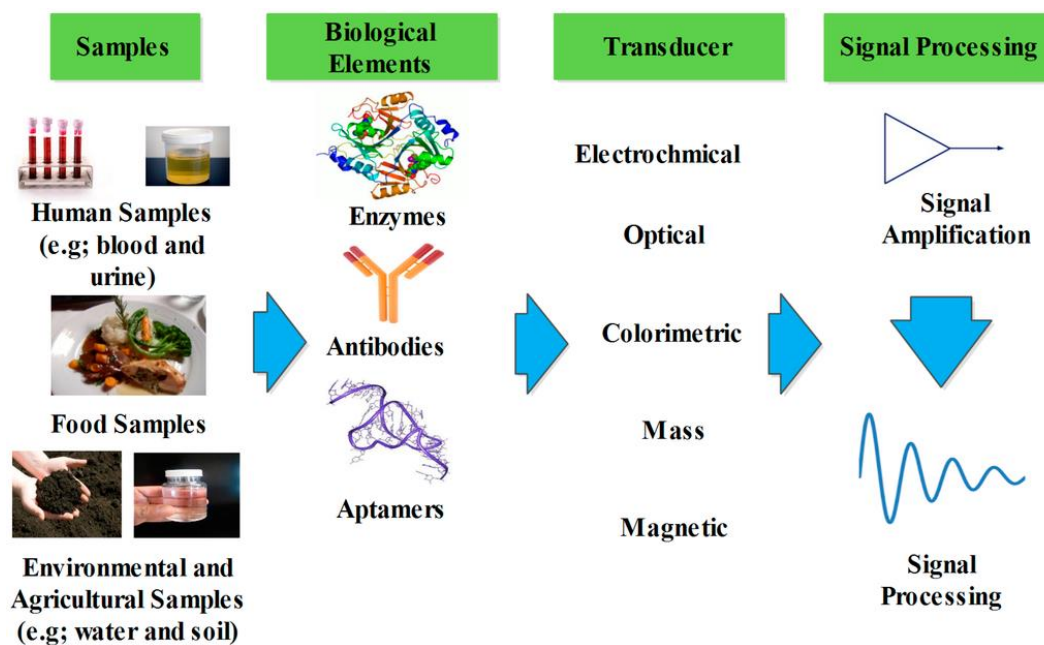
Figure 1.1 Schematic diagram of biosensors [5]

Compared to traditional analytical methods, the main advantages of biosensors are miniaturization, portability, and minimal sample preparation.[9, 10] Biosensors have a wide range of applications ranging from medical diagnostics,[11] to drug discovery,[12, 13] food quality,[14] environmental monitoring.[15, 16] More importantly, biosensors need to meet stringent requirements, such as good selectivity, high sensitivity, portability, reproducibility, low-cost, chemical and mechanical stability.[17, 18]

According to the principle of biometrics, biosensors are divided into catalytic biosensors and affinity or non-catalytic biosensors.[19] In catalytic biosensors, analyte-bioreceptor interactions lead to the development of new biochemical reaction products. Such biosensors include enzymes, microorganisms, tissues, and whole cells.

Enzymes are common biocatalysts that can effectively increase the rate of biological reactions. The working principle of enzyme-based biosensors relays on the catalytic reaction and binding

capacity of analyte detection.[20] Due to the long history of enzyme-based biosensors development, various biosensors can be produced on the basis of enzyme specificity, and the most common enzyme-based biosensors are glucose and urea biosensors. However, enzyme structures are extremely sensitive, and improving the sensitivity, stability, and adaptability of enzyme is expensive and complex.

With advances in nanotechnology, exploring nanomaterials, different nanomaterials with various characteristics provide the possibility of improving the performance of biosensors and increase the power of detection through size and morphology control.

1.2 Enzyme-like nanomaterials in boosted biosensors

As an emerging alternative to natural enzymes that require stringent physiological conditions to perform catalytic functions, nanomaterials with intrinsic enzyme-like activity (also known as Nanozyme) have attracted much attention due to their unique advantages such as high catalytic stability, easy modification, and low fabrication cost, showing great potential in biosensors to enhance signal and improve the detection performance. The properties of various nanozymes and their advantages over enzymes are shown in **Figure 1.2**.[21]
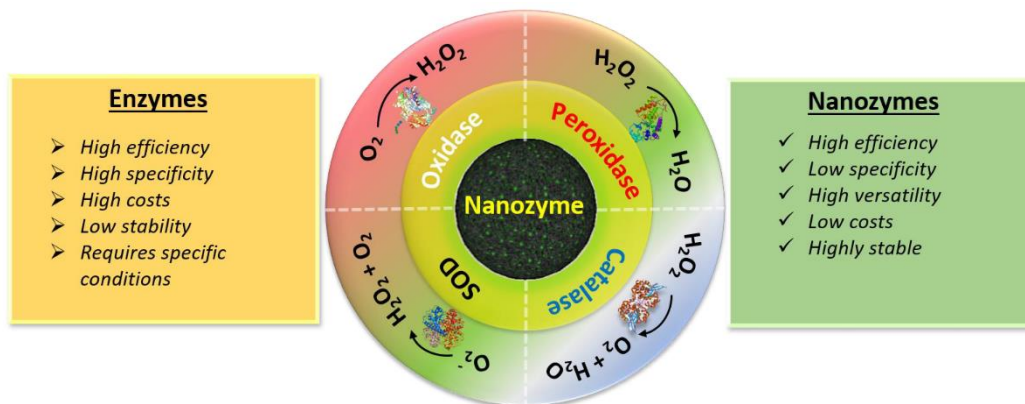
Figure 1.2 The properties of various nanozymes and the comparison between nanozyme and enzymes.[21]

1.2.1 Enzyme-like properties

Peroxidase-like (POD-like) activity is an important enzyme-like activity for nanomaterials. Peroxidase [22] is a natural enzyme that enables the substrate of hydrogen peroxide (H_2O_2) to be converted to H_2O in the presence of reducing substrate, and the substrate is oxidized to its corresponding oxide during this process.[23, 24] The peroxidases reactions can be simply summarized as the following equation:[25] $2RH + H_2O_2 \rightarrow 2R^{\cdot} + 2H_2O$, (RH represents a reducing substrate, $R^{\cdot}$ stands for the formed free radical). Horseradish peroxidase (HRP), as a typical peroxidase, has been studied over the years as a useful tool to catalyze H_2O_2.[26] However, the disadvantages such as difficulty in extraction and purification, weak environmental stability, high cost and poor reusability have limited its application in many fields.[27-29] Nanomaterial-based peroxidase mimics have received great attention in biomedical applications for the past few years.[30] Compared with natural peroxidase, these nanomaterials are easier to produce at a low cost and have outstanding catalytic stability, high specific surface area, and good stability against harsh environmental conditions.

One of the catalytic mechanisms of nanomaterials with POD-like activity can be described as reactive oxygen species (ROS) generated through some specific catalyzing reactions such as Fenton (hydroxide (OH^-) and hydroxyl radical formed from a reaction between Iron (II) (Fe^{2+}) and H_2O_2) and Haber-Weiss reactions (•OH (hydroxyl radicals) generated from H_2O_2 and superoxide (•O_2^-) catalyzed by iron ions), thus catalyzing the peroxidase substrate 3,3',5,5'-tetramethylbenzidine (TMB) to produce a blue color reaction.[22, 31] The other mechanism is the electron transfer between reducing substrates like TMB and H_2O_2.[32, 33]

Besides peroxidase, another major enzyme-like nanomaterial is oxidase-like.[34] Substrates can be directly catalyzed to their oxidation form without H_2O_2 participation.

Instead, dissolved oxygen is often involved in the reactions catalyzed by these mimetic oxidases.[35] To some extent, oxidase mimetics are more suitable for biochemical assays than peroxidases due to their simpler reaction conditions. Other than the above two important enzyme-like activities, superoxide dismutase (SOD), as a type of enzyme, can catalyze the dismutation of unstable superoxide radicals to O_2 and H_2O_2. SOD catalyzes the dismutation of superoxide anion to molecular oxygen and H_2O.[36] Catalase (CAT) is a common enzyme found in nearly all oxygen-exposed organisms (such as bacteria, plants, and animals) that catalyzes the breakdown of hydrogen peroxide into water and oxygen.[37] Catalase is essential for the removal of H_2O_2, which is produced in peroxisomes by photorespiration. [38, 39]

1.2.2 Biosensing applications

In the past decade, the application of nanomaterials in various biosensors is considered to have great potential to improve the detection performance of the biosensors. In this part, we will focus on the introduction of biosensors using nanomaterial with POD-like activities. The various types of biosensors, such as nanozyme-enzyme cascade, enzyme-based immunosensors, and lateral flow assay, have been deliberated to highlight their indispensable applications.

Enzyme immunoassays (EIAs) and enzyme-linked immunosorbent assays (ELISAs) have become the gold standard for medical laboratories, in vitro diagnostic products, regulatory agencies, and external quality assessment and proficiency testing organizations.[40, 41] ELISA are derived from radioimmunoassay (RIA) which was firstly described by Yalow and Berson in 1960.[42] In consideration of the radioactivity safety, RIA analysis was improved by replacing radioisotopes with enzymes, thereby creating the modern ELISA, representing a simple, reliable, and sensitive analytical tool for the rapid detection of target analytes.[43, 44] EIA/ELISA uses the basic immunological concept of the binding of an antigen to its specific antibody, and the interaction

5

between the antigen and antibody can be converted into a visible color change,[45] allowing detection of very small amounts of antigens such as proteins, peptides, antibodies in virus, hormone, or fluid samples.[46, 47]

In general, ELISA models can be classified into three types: direct ELISA, sandwich ELISA, and competitive ELISA (**Figure 1.3**).[48] In a direct ELISA, the antigen is directly immobilized on the plate, and a conjugated detection antibody binds to the target protein.[49, 50] The detection process is quick and simple but has the disadvantage of low specificity because only one antibody is used, and there can be high background produced.

Sandwich ELISA is the most commonly used type of ELISA, which is often used for large molecular detection. A sandwich ELISA measures antigen between two layers of antibodies (capture and detection antibody).[51, 52] This type of ELISA has the highest sensitivity and specificity, and is compatible with complex sample matrices.

Lastly, competitive ELISA is widely used for small molecules when the detection target is too small and has only one epitope or antibody binding site. Competitive ELISA is a powerful and effective tool for small molecule detection. Competitive ELISA relies on the competition between the antigen of interest (the analyte) and the same antigen that is coated to the multi-well plate.[53, 54] The more antigen present in the sample the less bound antigen will be bound to the capture antibody.
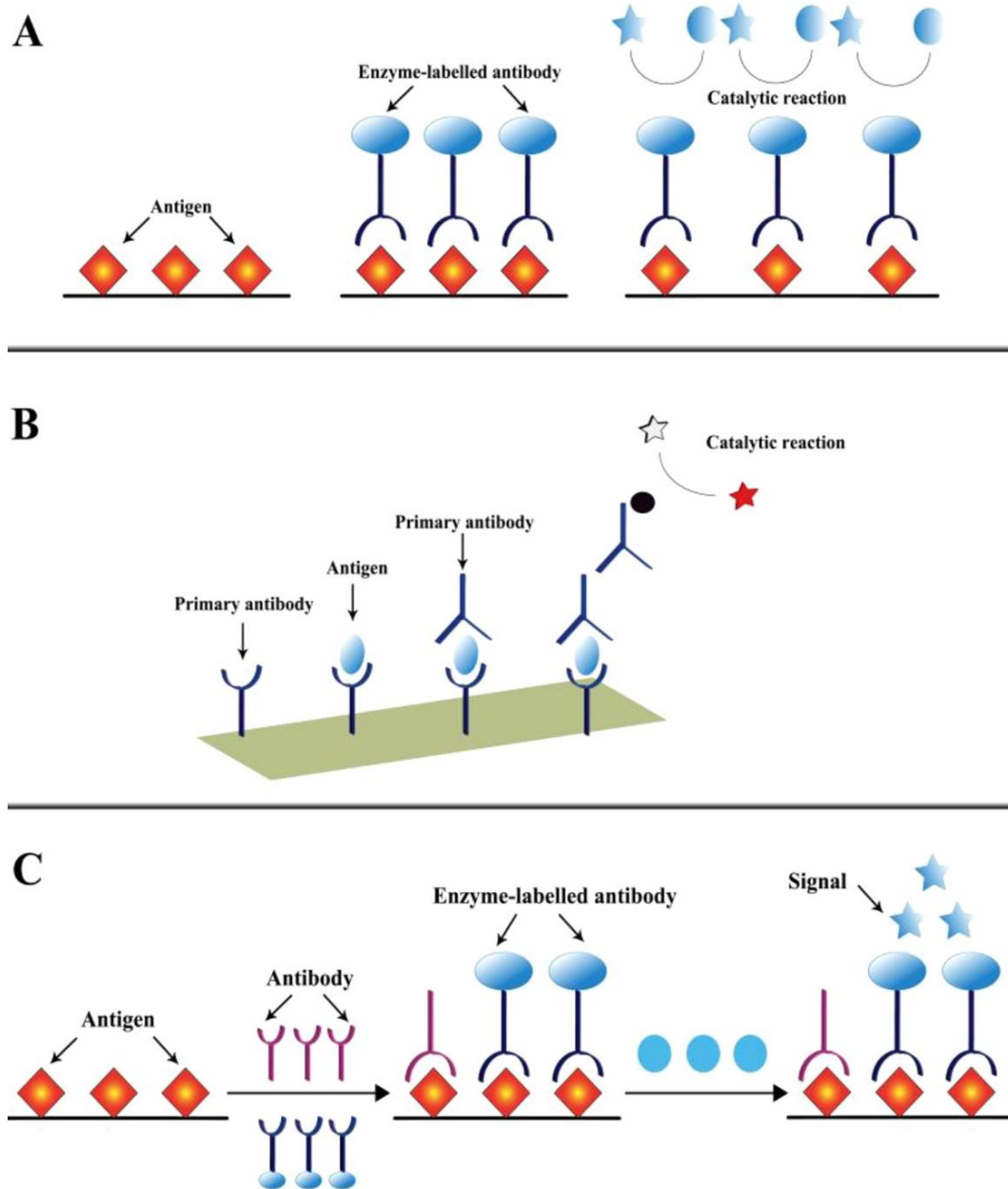
Figure 1.3 Scheme of the basic steps of direct ELISA (A) Sandwich ELISA (B) and competitive ELISA (C).[48]

Although ELISA has outstanding advantages of high sensitivity and high throughput, it is time-consuming and not favorable for point-of-care testing (POCT). Compared with the ELISA, lateral-flow immunoassay (LFIA) is a simple, rapid, cost-effective, and sensitive detection method to

detect a specific biomarker that can overcome these limitations, making LFIA a widely used paper-based immunochromatographic test strip suitable for POCT.[55, 56]

The first lateral flow immunoassay (LFIA) was described and patented in late 1970. A few years later, LFIAs measuring levels of the human hormone chorionic gonadotropin in urine to determine pregnancy entered the market. Since then, the concept of "point-of-care testing" and eventually "personalized medicine" has been a popular research field.[57, 58] LFIA is based on the recognition of one or more analytes of interest, mainly proteins, through the use of antibodies. Antibodies are immobilized on nitrocellulose membranes and interact with the analyte in a sandwich (for detecting relatively large analytes) or competition format (used when the analyte is too small for two antibodies to bind simultaneously) using appropriate labels, the mechanism is shown in **Figure 1.4**.[59]
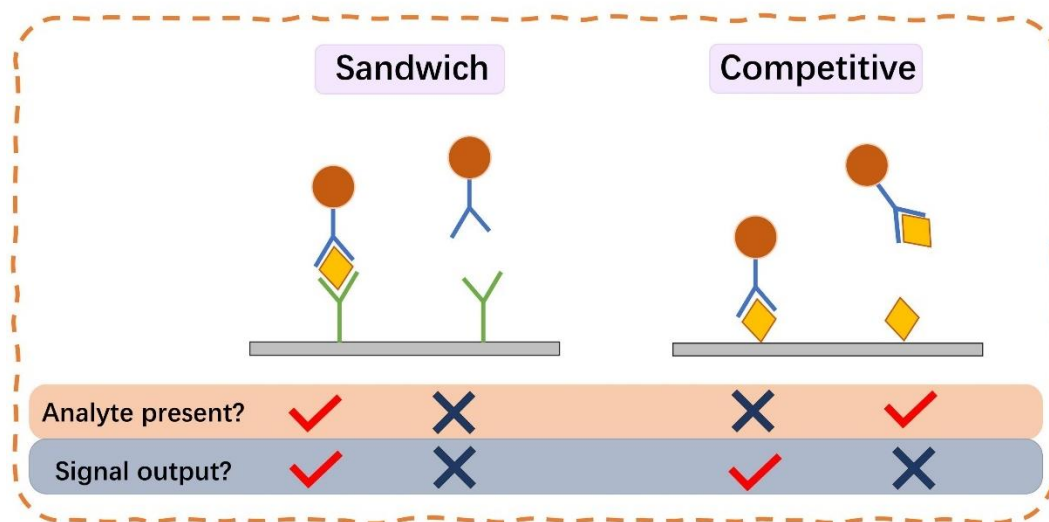
Figure 1.4 Illustration of the sandwich and competitive lateral-flow immunoassay

1.3 Single-atom engineering

Nanomaterials with POD-like activity have received great attention in biomedical applications due to the advantages such as low cost and outstanding catalytic stability, high specific surface area, and good stability against harsh environmental conditions.[60] However, the bulk nanomaterials

have suffered from relatively limited surface areas exposure and restricted active sites for enzymatic catalysis, which would hinder the reaction efficiency.

Single-atomic site catalysts (SASCs), on the other hand, own completely isolated active metal sites through precise design at the atomic level, have attracted widespread attention for their remarkable catalytic activity, satisfactory stability, homogeneous active sites, maximum metal atom utilization, and specialty geometric structure.[61, 62] Recently, some single-atomic site catalysts, especially Fe-based SASC with isolated Fe atoms, have shown superior enzyme-like characteristics due to the following two reasons. From the catalysis perspective, single-atom engineering can be used to decrease the size of the metal particles and own a low-coordinated metal atom, thereby increasing the intrinsic activity of each metal atom.[63] In our group, Ding et al. designed a Fe-N-C-based SAC with atomically dispersed $Fe-N_x$ active sites, the synthesized SASC can effectively mimic the active sites of heme enzymes and the peroxidase-mimic activity of SASC reached 42.8 U mg^{-1}.[64] From the enzyme-mimic perspective, the $Fe-N_x$ active sites of Fe-N-C-based SACs can mimic the active center of natural HRP, further enhancing the catalytic specificity.[65] Fe-SASCs have been developed to achieve theoretically maximum atom utilization and utilized as a promising alternative to natural HRP.[66, 67] Nowadays, the SASCs have found their extensive application in immunoassays,[68] environmental treatment,[69] biodetection and biosensing,[70] as shown in **Figure 1.5**. [71]
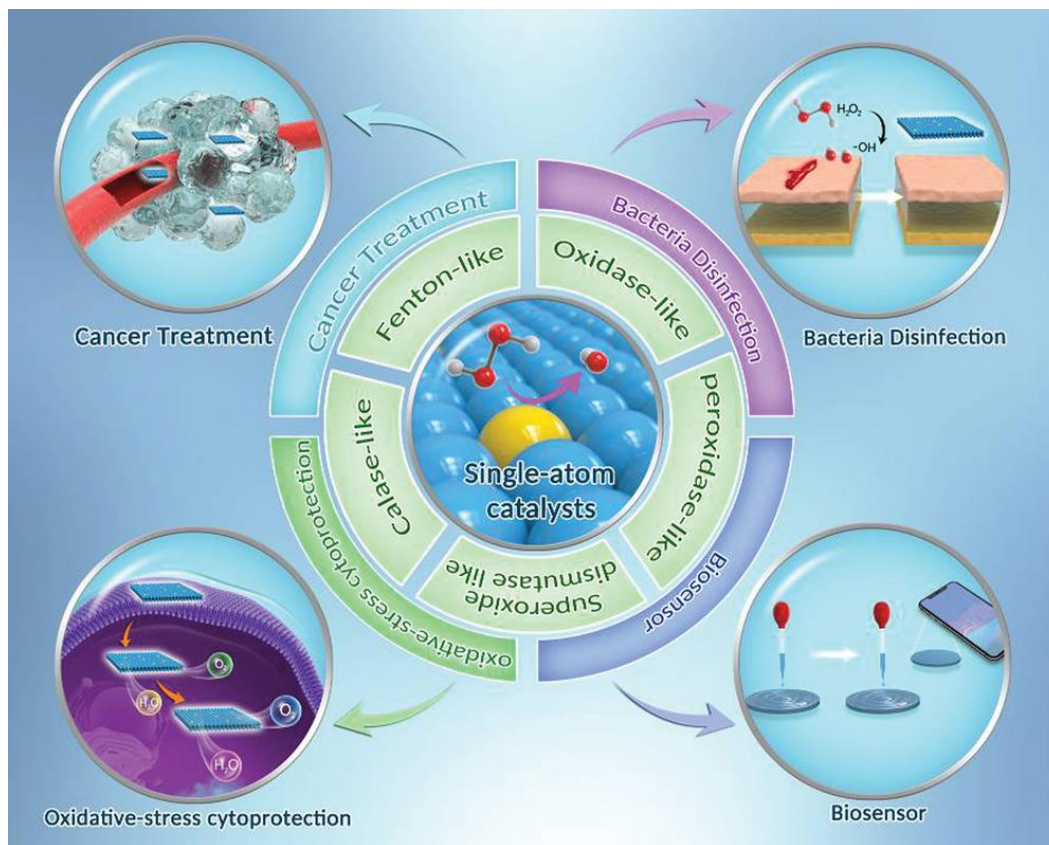
Figure 1.5 Schematic illustration of single-atom catalysts (SACs)-triggered catalysis for versatile biomedical applications. [71]

1.4 Research projects

In this dissertation, my research work mainly focused on designing single atomic site catalysts (SASCs) with high POD-like activity through different approaches. A series of characterizations proved that the Fe-N-C single atomic sites could achieve structural mimic of natural HRP. Also, different strategies to increase the density of single-atomic sites and expose the active sites on the surface to better participate in the reaction. Then, we used the synthesized SASC in different biosensing applications. Specific research work on structure controlling, specific activity, and biosensing applications are shown as follows.

1.4.1 Project I: Iron-Imprinted Single-Atomic Site Catalyst Based Nanoprobe for Hydrogen Peroxide Detection in Living Cells

In this work, precisely controlling the isolated single-atom Fe-N-C active site structure is crucial to improving the SASCs' performance. A facile ion-imprinting method (IIM) is used to synthesize isolated Fe-N-C single-atomic site catalysts and realize the structural mimic of natural HRP. Then, the designed Fe-N-C SASC was used as a nanoprobe in colorimetric biosensing of hydrogen peroxide (H_2O_2) generated from cells.

1.4.2 Project II: Single-Atomic Site Catalyst Enhanced Immunosorbent Assay for Alzheimer's Disease Detection

From work I, it was proved that the Fe-N-C single-atomic sites could mimic the structure of active sites in natural HRP. In this work, the density of single-atomic sites was enhanced to increase the enzyme-like activity of SASC further. Herein, we have developed a novel Fe-N-C single atom site catalyst (Fe-N_x SASCs) with increased active sites density through the surface coating to introduce the nanoconfinement effect and used to substitute the enzymes in the ELISA kit to enhance the detection sensitivity of amyloid beta 1-40, which is a biomarker of Alzheimer's disease.

1.4.3 Project III: Two-Dimensional Fe-N-C Single Atomic Site Catalysts with Boosted Peroxidase-Like Activity for Sensitive Immunoassay

It's well known that the active sites on the surface can easily participate in the reaction. Thus, a better catalytic behavior can be achieved by exposing more sites on the surface. In this project, we combined the advantage of two-dimensional nanomaterials and SASC to get the 2D Fe-N-C SASC, this novel SASC possesses high POD-like activity due to the more exposed single-atomic sites. What's more, we have used iron (II) phthalocyanine (FePc) in preparing the precursor, in this way,

11

the Fe-N structure has been induced into our SASCs, thus achieving a structural mimic of natural HRP. Later, the SASC was used for sensitive detection of 2,4-Dichlorophenoxyacetic acid (2,4-D).

1.4.4 Project IV: Single-Atomic Site Catalyst Enhanced Lateral-flow Immunoassay for Herbicide Detection

The biosensing platform used in the previous work is time-consuming and requires laboratory equipment and fails to realize the on-site detection. The lateral-flow immunoassay (LFIA) developed in this work can be used as an effective point-of-care detection method. To be specific, SASC with excellent enzyme-like activity is designed and synthesized from hemin-doped ZIF-8, creating active sites that mimic the Fe active center coordination environment of natural enzyme and their functions. Utilizing its outstanding catalytic activity, the Fe-SASC is used as the label to construct LFIA (Fe-SASC-LFIA) for herbicide detection.

REFERENCE

1. A.A. Zuber, E. Klantsataya, A. Bachhuka, 3.06 - Biosensing, in: D.L. Andrews, R.H. Lipson, T. Nann (Eds.) Comprehensive Nanoscience and Nanotechnology (Second Edition), Academic Press, Oxford, 2019, 105-126.

2. S. Zeng, K.-T. Yong, I. Roy, X.-Q. Dinh, X. Yu, F. Luan, A review on functionalized gold nanoparticles for biosensing applications, Plasmonics, 6 (2011) 491-506.

3. M. Holzinger, A. Le Goff, S. Cosnier, Nanomaterials for biosensing applications: a review, Frontiers in Chemistry, 2 (2014) 63.

4. D. Buerk, Biosensors: Theory and Applications; Technomic Publish. Co, Inc.: Lancaster, UK, (1993).

5. G. Luka, A. Ahmadi, H. Najjaran, E. Alocilja, M. DeRosa, K. Wolthers, A. Malki, H. Aziz, A. Althani, M. Hoorfar, Microfluidics integrated biosensors: A leading technology towards lab-on-a-chip and sensing applications, Sensors, 15 (2015) 30011-30031.

6. W.R. Heineman, W.B. Jensen, Leland c. clark jr.(1918-2005), Biosensors and Bioelectronics, 8 (2006) 1403-1404.

7. L.C. Clark Jr, C. Lyons, Electrode systems for continuous monitoring in cardiovascular surgery, Annals of the New York Academy of Sciences, 102 (1962) 29-45.

8. L.C. Clark Jr, E.W. Clark, A personalized history of the Clark oxygen electrode, International Anesthesiology Clinics, 25 (1987) 1-29.

9. C.R. Lowe, Biosensors, Trends in Biotechnology, 2 (1984) 59-65.

10. P.T. Kissinger, Biosensors-a perspective, Biosensors and Bioelectronics, 20 (2005) 2512-2516.

11. S. Afsahi, M.B. Lerner, J.M. Goldstein, J. Lee, X. Tang, D.A. Bagarozzi, D. Pan, L. Locascio, A. Walker, F. Barron, B.R. Goldsmith, Novel graphene-based biosensor for early detection of Zika virus infection, Biosensors and Bioelectronics, 100 (2018) 85-88.

12. M.A. Cooper, Optical biosensors in drug discovery, Nature Reviews Drug Discovery, 1 (2002) 515-528.

13. M. Keusgen, Biosensors: new approaches in drug discovery, Naturwissenschaften, 89 (2002) 433-444.

14. W. Wang, S. Gunasekaran, Nanozymes-based biosensors for food quality and safety, TrAC Trends in Analytical Chemistry, 126 (2020) 115841.

15. K. Rogers, J. Lin, Biosensors for environmental monitoring, Biosensors and Bioelectronics, 7 (1992) 317-321.

16. M. Badihi-Mossberg, V. Buchner, J. Rishpon, Electrochemical biosensors for pollutants in the environment, Electroanalysis: An International Journal Devoted to Fundamental and Practical Aspects of Electroanalysis, 19 (2007) 2015-2028.

17. S.K. Vashist, A. Venkatesh, K. Mitsakakis, G. Czilwik, G. Roth, F. von Stetten, R. Zengerle, Nanotechnology-based biosensors and diagnostics: technology push versus industrial/healthcare requirements, Bionanoscience, 2 (2012) 115-126.

18. B.E. Rapp, F.J. Gruhl, K. Länge, Biosensors with label-free detection designed for diagnostic applications, Analytical and Bioanalytical Chemistry, 398 (2010) 2403-2412.

19. H.H. Nguyen, S.H. Lee, U.J. Lee, C.D. Fermin, M. Kim, Immobilized enzymes in biosensor applications, Materials, 12 (2019) 121.

20. D.W. Morrison, M.R. Dokmeci, U. Demirci, A. Khademhosseini, Clinical applications of micro-and nanoscale biosensors, Biomedical Nanostructures, (2007) 439-460.

21. S. Thangudu, C.-H. Su, Peroxidase mimetic nanozymes in cancer phototherapy: Progress and perspectives, Biomolecules, 11 (2021) 1015.

22. L. Gao, J. Zhuang, L. Nie, J. Zhang, Y. Zhang, N. Gu, T. Wang, J. Feng, D. Yang, S. Perrett, Intrinsic peroxidase-like activity of ferromagnetic nanoparticles, Nature Nanotechnology, 2 (2007) 577-583.

23. M. Hamid, Potential applications of peroxidases, Food Chemistry, 115 (2009) 1177-1186.

24. M. Khanmohammadi, M.B. Dastjerdi, A. Ai, A. Ahmadi, A. Godarzi, A. Rahimi, J. Ai, Horseradish peroxidase-catalyzed hydrogelation for biomedical applications, Biomaterials Science, 6 (2018) 1286-1298.

25. G.R. Lopes, D.C. Pinto, A.M. Silva, Horseradish peroxidase (HRP) as a tool in green chemistry, RSC Advances, 4 (2014) 37244-37265.

26. C. Dong, J. Ji, B. Shen, M. Xing, J. Zhang, Enhancement of H_2O_2 Decomposition by the Co-catalytic Effect of WS2 on the Fenton Reaction for the Synchronous Reduction of Cr (VI) and Remediation of Phenol, Environmental Science & Technology, 52 (2018) 11297-11308.

27. H. Lechner, N. Ferruz, B. Höcker, Strategies for designing non-natural enzymes and binders, Current Opinion in Chemical Biology, 47 (2018) 67-76.

28. F. Rigoldi, S. Donini, A. Redaelli, E. Parisini, A. Gautieri, Engineering of thermostable enzymes for industrial applications, APL Bioengineering, 2 (2018) 011501.

29. Z.-T. Liu, S.-K. Li, R.-T. Wei, A.-Y. Chen, Y.-Q. Chai, R. Yuan, Y. Zhuo, CuS porous nanospheres as a novel noble metal-free co-reaction accelerator for enhancing electrochemiluminescence and sensitive immunoassay of mucin 1, Sensors and Actuators B: Chemical, 274 (2018) 110-115.

30. Z. Wang, R. Zhang, X. Yan, K. Fan, Structure and activity of nanozymes: Inspirations for de novo design of nanozymes, Materials Today, (2020) 81-119.

31. D. Jiang, D. Ni, Z.T. Rosenkrans, P. Huang, X. Yan, W. Cai, Nanozyme: new horizons for responsive biomedical applications, Chemical Society Reviews, 48 (2019) 3683-3704.

32. J. Mu, Y. Wang, M. Zhao, L. Zhang, Intrinsic peroxidase-like activity and catalase-like activity of Co 3 O 4 nanoparticles, Chemical Communications, 48 (2012) 2540-2542.

33. W. Zhang, S. Hu, J.-J. Yin, W. He, W. Lu, M. Ma, N. Gu, Y. Zhang, Prussian blue nanoparticles as multienzyme mimetics and reactive oxygen species scavengers, Journal of the American Chemical Society, 138 (2016) 5860-5865.

34. A. Asati, S. Santra, C. Kaittanis, S. Nath, J.M. Perez, Oxidase-like activity of polymer-coated cerium oxide nanoparticles, Angewandte Chemie, 121 (2009) 2344-2348.

35. J. Chen, Q. Ma, M. Li, D. Chao, L. Huang, W. Wu, Y. Fang, S. Dong, Glucose-oxidase like catalytic mechanism of noble metal nanozymes, Nature communications, 12 (2021) 1-9.

36. P. Samanta, S. Pal, A.K. Mukherjee, A.R. Ghosh, Biochemical effects of glyphosate based herbicide, Excel Mera 71 on enzyme activities of acetylcholinesterase (AChE), lipid peroxidation (LPO), catalase (CAT), glutathione-S-transferase (GST) and protein content on teleostean fishes, Ecotoxicology and Environmental Safety, 107 (2014) 120-125.

37. P. Chelikani, I. Fita, P.C. Loewen, Diversity of structures and properties among catalases, Cellular and Molecular Life Sciences CMLS, 61 (2004) 192-208.

38. C.M. Luna, G.M. Pastori, S. Driscoll, K. Groten, S. Bernard, C.H. Foyer, Drought controls on H_2O_2 accumulation, catalase (CAT) activity and CAT gene expression in wheat, Journal of Experimental Botany, 56 (2005) 417-423.

39. J. Zhang, R. Chen, Z. Yu, L. Xue, Superoxide dismutase (SOD) and catalase (CAT) activity assay protocols for caenorhabditis elegans, Bio-Protocol, 7 (2017) 2505.

40. J.E. Butler, Enzyme-linked immunosorbent assay, Journal of Immunoassay, 21 (2000) 165-209.

41. Q. Zhao, D. Lu, G. Zhang, D. Zhang, X. Shi, Recent improvements in enzyme-linked immunosorbent assays based on nanomaterials, Talanta, 223 (2021) 121722.

42. R.S. Yalow, S.A. Berson, Immunoassay of endogenous plasma insulin in man, The Journal of Clinical Investigation, 39 (1960) 1157-1175.

43. J. Ghassemi Nejad, K.-H. Park, F. Forghani, H.-G. Lee, J.-S. Lee, K.-I. Sung, Measuring hair and blood cortisol in sheep and dairy cattle using RIA and ELISA assay: a comparison, Biological Rhythm Research, 51 (2020) 887-897.

44. S. Hosseini, P. Vázquez-Villegas, M. Rito-Palomares, S.O. Martinez-Chapa, Advantages, disadvantages and modifications of conventional ELISA, Enzyme-linked Immunosorbent Assay (ELISA), Springer2018. 67-115.

45. H.-N. Chan, D. Xu, S.-L. Ho, D. He, M.S. Wong, H.-W. Li, Highly sensitive quantification of Alzheimer's disease biomarkers by aptamer-assisted amplification, Theranostics, 9 (2019) 2939.

46. S.D. Gan, K.R. Patel, Enzyme immunoassay and enzyme-linked immunosorbent assay, J Invest Dermatol, 133 (2013) 12.

47. S. Zhao, C. Smits, N. Schuurman, S. Barnum, N. Pusterla, F. Van Kuppeveld, B.-J. Bosch, K. Van Maanen, H. Egberink, Development and validation of a S1 protein-based ELISA for the specific detection of antibodies against equine coronavirus, Viruses, 11 (2019) 1109.

48. L. Wu, G. Li, X. Xu, L. Zhu, R. Huang, X. Chen, Application of nano-ELISA in food analysis: Recent advances and challenges, TrAC Trends in Analytical Chemistry, 113 (2019) 140-156.

49. A.V. Lin, Direct ELISA, ELISA, Springer2015. 61-67.

50. F. Rubio, L.J. Veldhuis, B.S. Clegg, J.R. Fleeker, J.C. Hall, Comparison of a direct ELISA and an HPLC method for glyphosate determinations in water, Journal of Agricultural and Food chemistry, 51 (2003) 691-696.

51. C.K. Fæste, C. Plassen, Quantitative sandwich ELISA for the determination of fish in foods, Journal of Immunological Methods, 329 (2008) 45-55.

52. C.K. Dixit, S.K. Vashist, F.T. O'Neill, B. O'Reilly, B.D. MacCraith, R. O'Kennedy, Development of a high sensitivity rapid sandwich ELISA procedure and its comparison with the conventional approach, Analytical Chemistry, 82 (2010) 7049-7052.

53. Y. Xiong, Y. Leng, X. Li, X. Huang, Y. Xiong, Emerging strategies to enhance the sensitivity of competitive ELISA for detection of chemical contaminants in food samples, TrAC Trends in Analytical Chemistry, 126 (2020) 115861.

54. I. Segura-Gil, A. Blázquez-Soro, P. Galán-Malo, L. Mata, A.P. Tobajas, L. Sánchez, M.D. Pérez, Development of sandwich and competitive ELISA formats to determine β-conglycinin: Evaluation of their performance to detect soy in processed food, Food Control, 103 (2019) 78-85.

55. L. Anfossi, F. Di Nardo, S. Cavalera, C. Giovannoli, C. Baggiani, Multiplex lateral flow immunoassay: an overview of strategies towards high-throughput point-of-need testing, Biosensors, 9 (2019) 2.

56. R. Banerjee, A. Jaiswal, Recent advances in nanoparticle-based lateral flow immunoassay as a point-of-care diagnostic tool for infectious agents and diseases, Analyst, 143 (2018) 1970-1996.

57. A. St John, C.P. Price, Existing and emerging technologies for point-of-care testing, The Clinical Biochemist Reviews, 35 (2014) 155.

58. C.P. Price, A.S. John, Point-of-care testing: making innovation work for patient-centered care, American Association for Clinical Chemistry 2012.

59. C. Parolo, A. de la Escosura-Muñiz, A. Merkoçi, Enhanced lateral flow immunoassay using gold nanoparticles loaded with enzymes, Biosensors and Bioelectronics, 40 (2013) 412-416.

60. X. Wang, H. Wang, S. Zhou, Progress and Perspective on Carbon-Based Nanozymes for Peroxidase-like Applications, The Journal of Physical Chemistry Letters, 12 (2021) 11751-11760.

61. Z. Lyu, S. Ding, N. Zhang, Y. Zhou, N. Cheng, M. Wang, M. Xu, Z. Feng, X. Niu, Y. Cheng, C. Zhang, D. Du, Y. Lin, Single-Atom Nanozymes Linked Immunosorbent Assay for Sensitive Detection of Aβ1-40: A Biomarker of Alzheimer's Disease, Research, 2020 (2020) 4724505.

62. S. Ding, Z. Lyu, H. Zhong, D. Liu, E. Sarnello, L. Fang, M. Xu, M.H. Engelhard, H. Tian, T. Li, X. Pan, S.P. Beckman, S. Feng, D. Du, J.-C. Li, M. Shao, Y. Lin, An Ion-Imprinting Derived Strategy to Synthesize Single-Atom Iron Electrocatalysts for Oxygen Reduction, Small, 17 (2021) 2004454.

63. S. Ding, Z. Lyu, E. Sarnello, M. Xu, L. Fang, H. Tian, S.E. Karcher, T. Li, X. Pan, J. McCloy, G. Ding, Q. Zhang, Q. Shi, D. Du, J.-C. Li, X. Zhang, Y. Lin, A MnOx enhanced atomically dispersed iron-nitrogen-carbon catalyst for the oxygen reduction reaction, Journal of Materials Chemistry A, (2022).

64. S. Ding, Z. Lyu, L. Fang, T. Li, W. Zhu, S. Li, X. Li, J.-C. Li, D. Du, Y. Lin, Single-atomic site catalyst with heme enzymes-like active sites for electrochemical sensing of hydrogen peroxide, Small, 17 (2021) 2100664.

65. Z. Lyu, S. Ding, M. Wang, X. Pan, Z. Feng, H. Tian, C. Zhu, D. Du, Y. Lin, Iron-imprinted single-atomic site catalyst-based nanoprobe for detection of hydrogen peroxide in Living Cells, Nano-Micro Letters, 13 (2021) 146.

66. Y. Wu, L. Jiao, X. Luo, W. Xu, X. Wei, H. Wang, H. Yan, W. Gu, B.Z. Xu, D. Du, Oxidase-like Fe-N-C single-atom nanozymes for the detection of acetylcholinesterase activity, Small, 15 (2019) 1903108.

67. X. Niu, Q. Shi, W. Zhu, D. Liu, H. Tian, S. Fu, N. Cheng, S. Li, J.N. Smith, D. Du, Unprecedented peroxidase-mimicking activity of single-atom nanozyme with atomically dispersed Fe-N_x moieties hosted by MOF derived porous carbon, Biosensors and Bioelectronics, 142 (2019) 111495.

68. N. Cheng, J.C. Li, D. Liu, Y. Lin, D. Du, Single-atom nanozyme based on nanoengineered Fe-N-C aatalyst with superior peroxidase-like activity for ultrasensitive bioassays, Small, 15 (2019) 1901485.

69. H. Yan, H. Lv, H. Yi, W. Liu, Y. Xia, X. Huang, W. Huang, S. Wei, X. Wu, J. Lu, Understanding the underlying mechanism of improved selectivity in Pd_1 single-atom catalyzed hydrogenation reaction, Journal of Catalysis, 366 (2018) 70-79.

70. Y. Wu, J. Wu, L. Jiao, W. Xu, H. Wang, X. Wei, W. Gu, G. Ren, N. Zhang, Q. Zhang, Cascade reaction system integrating single-atom nanozymes with abundant Cu sites for enhanced biosensing, Analytical Chemistry, 92 (2020) 3373-3379.

71. H. Xiang, W. Feng, Y. Chen, Single-atom catalysts in catalytic biomedicine, Advanced Materials, 32 (2020) 1905994.

CHAPTER TWO: IRON-IMPRINTED SINGLE-ATOMIC SITE CATALYST BASED

NANOPROBE FOR HYDROGEN PEROXIDE DETECTION IN LIVING CELLS

This chapter is published as: **Zhaoyuan Lyu**, Shichao Ding, Maoyu Wang, Xiaoqing Pan, Zhenxing Feng, Hangyu Tian, Chengzhou Zhu, Dan Du, Yuehe Lin. Iron-Imprinted Single-Atomic Site Catalyst-Based Nanoprobe for Detection of Hydrogen Peroxide in Living Cells. Nano-micro letters, 2021, 13(1): 1-13.

Contributions: **Zhaoyuan Lyu**: Conceptualization, Methodology, Investigation, Formal analysis, Validation, Writing-original draft, Writing-review & editing. Shichao Ding: Resources, Formal analysis, Investigation, Writing-review & editing. Maoyu Wang: Resources. Xiaoqing Pan: Resources. Zhenxing Feng: Resources. Hangyu Tian: Writing-review & editing. Chengzhou Zhu: Writing-review & editing. Dan Du: Supervision, Writing-review & editing, Project administration, Funding acquisition. Yuehe Lin: Conceptualization, Supervision, Project administration, Writing-review & editing, Funding acquisition.

2.1 Introduction

Hydrogen peroxide (H_2O_2), playing an important role in physiological processes and as a messenger molecule for cellular effects, is crucial for immune response and cell growth/senescence, [1, 2] and also serve as potential biomarkers for diagnosis or monitoring diseases, such as diabetes, cancers, inflammation, cardiovascular and neurodegenerative diseases.[3, 4] Therefore, sensing H_2O_2 generated from living cells with high sensitivity and specificity will be of vital clinical value for disease diagnosis and better comprehension of disease mechanisms.[5, 6] However, due to the relatively low concentration of H_2O_2 in physiological environments, *in vivo* H_2O_2 sensing for clinical applications remains a challenge.[7] Developing highly sensitive H_2O_2-responsive probes has paramount importance for biosensing in living cells.

Single-atomic site catalysts (SASCs) containing atomically dispersed metal active sites demonstrate distinctive advantages in catalytic activities and selectivity for various catalytic reactions.[8-14] Recently, SASCs with peroxidase-like activity characteristics have attracted numerous attentions in the biosensing field due to their attractive properties of high stability and unprecedented catalytic performance towards H_2O_2.[15-18] Therefore, Fe-based SASCs are considered as substitutes of natural horseradish peroxidase (HRP) owing to their maximum specific activity and atomic utilization and have been applied in biosensing and bioremediation. [19-22]

To rationally design Fe-based SASCs, researchers are usually devoted to selecting special precursors that either already contain single-atom metal species or use the coordination between the complex ligands and surface groups of support materials.[23, 24] Moreover, adsorbing iron ions to bulk materials or using a top-down synthetic method to peel off iron from metal bulk can also synthesize SASCs.[25-27] These methods have drawbacks of using expensive organic macromolecule complexes and running the risk of aggregating single-atom metal species into nanosized metal counterparts.[28, 29] The resulted SASCs either require high cost or possess a relatively low density of the active sites, which limit their large-scale practical applications. Therefore, new strategies for constructing coordination sites for preparing Fe-based SASCs are urgently needed.

Ion-imprinting technology (IIT) is a type of molecularly imprinted technology that involves self-assembly of the interested ion (the template), complementary functional monomers, and cross-linkers to synthesize imprinted materials.[30-32] Generally, pre-polymerized complex systems can be formed during the preassembled system with each isolated template ion interacting with function monomer independently, and the template ions are embedded and isolated in the cross-

linked matrix after the polymerization process. Due to the pro-coordination process between ions and functional monomers, the activate sites are precisely controlled at the atomic level and high-density single-atom irons are obtained. Hence, based on the advantages of IIT, it is believed that utilizing IIT can effectively confine the ion in the matrix and achieve a high yield of SASCs with a low-cost and straightforward process.[33]

Hence, a facile ion-imprinting approach was used to synthesize the Fe-based single-atomic site catalyst (IIM-Fe-SASC),[34] and the developed Fe-SASC was used as a nanoprobe for *in situ* intracellular H_2O_2 detections (**Figure 2.1**). For synthesizing the IIM-Fe-SASC, the mesoporous silica was used as the matrix in the imprinted materials to prevent aggregation of the isolated iron ions. The [3-(2-Aminoethylamino)propyl]trimethoxysilane (A-Tri-EOS) was selected as functional monomers for that it could provide coordination sites to immobilize the iron atom. Precisely controlled high density single atomic activate sites were achieved during the pro-coordination process between iron ions and A-Tri-EOS. IIM-Fe-SASC with inherent peroxidase-like activity could catalyze H_2O_2 to reactive oxygen species. In this paper, we successfully applied IIM-Fe-SASC as the sensing probe in a typical colorimetric assay to detect H_2O_2 with ultrahigh sensitivity and specificity. The IIM-Fe-SASC showed better peroxidase-like ability than that of non-imprinted references. Importantly, *in situ* detection of H_2O_2 generated from breast cancer cells (MDA-MB-231) was performed using the IIM-Fe-SASC based assay, which demonstrates the practical clinic applications of SASC nanoprobe.
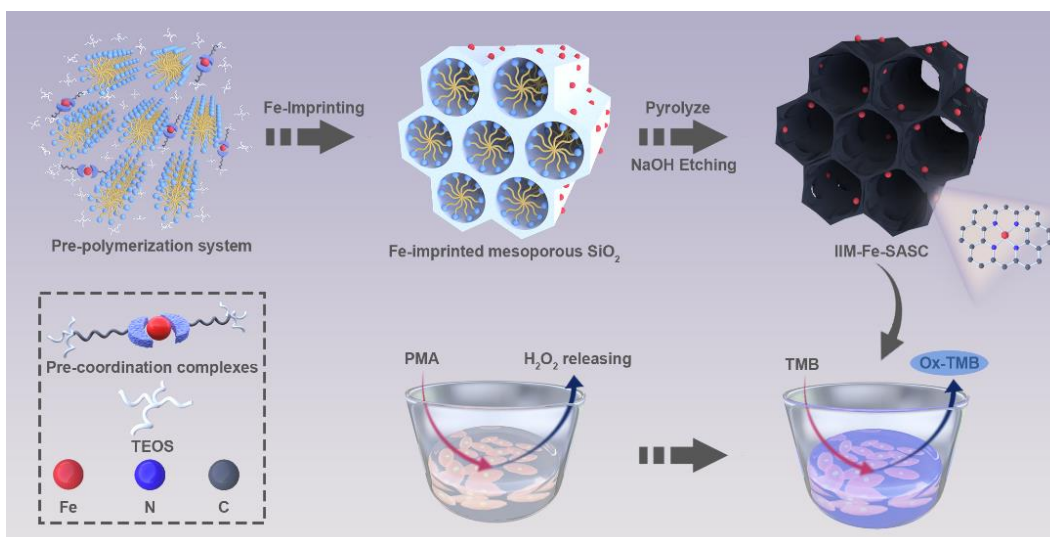
Figure 2.1 Schematic diagram of the process steps for IIM-Fe-SASC nanoprobe synthesis and in situ intracellular hydrogen peroxide detection.

2.2 Experimental

2.2.1 Preparation of single-atomic site catalyst nanoprobe

To prepare IIM-Fe-SASC, the mesoporous structure-directing micelles (solution 1) was first prepared by adding 0.6 g cetyltrimethylammonium bromide (CTAB) in a NaOH solution under vigorous stirring. 11 mg ion template Fe $(NO_3)_3$ and 0.25 mL functional monomers A-Tri-EOS were dissolved together and shaken for 15 min (solution 2), aiming to form the pre-coordination complexes of iron ions-functional monomers. Then, solution 2 and 2.5 mL cross-linking agent tetraethyl orthosilicate (TEOS) were added dropwise to solution 1, and the Fe-imprinted mesoporous SiO_2 could be obtained through filtration after reaction for 2 h. Meanwhile, to analyze and compare the performance of IIM-Fe-SASC, two more materials were synthesized and used as compare samples: Fe-based SASC synthesized using an adsorbing method (NIM-Fe-SASC) and a non-imprinted nanomaterial without Fe ions (NIM).

For the adsorbing method, non-imprinted mesoporous SiO_2 was prepared with the same route without adding iron ions. Subsequently, the obtained mesoporous SiO_2 was used to absorb the

same amount of Fe $(NO_3)_3$ solution and then the Fe-adsorbed mesoporous SiO_2 was collected after filtration. The Fe-imprinted mesoporous SiO_2, Fe-adsorbed mesoporous SiO_2, and mesoporous SiO_2 were pyrolyzed at 900^oC for 30 min in N_2 atmosphere and then 30 min in NH_3 atmosphere. Then, the isolation matrix SiO_2 was removed by soaking in 3 M NaOH at 80^oC for 48 hours. The synthesized samples are named IIM-Fe-SASC (by imprinting method), NIM-Fe-SASC (by adsorbing method), and NIM (without adding Fe iron), respectively.

2.2.2 Detect H_2O_2 produced from the breast cancer cells

In order to evaluate the H_2O_2 released from MDA-MB-231 cells, the cells were placed in a 96-well plate for 24 hours. After that, the plates were washed three times using PBS solution. Then, PMA solution (20μL, 2μM) and 100μL PBS were sequentially added, and incubated for 30 minutes. Finally, IIM-Fe-SASC (10 mg/mL, 50μL), TMB (1 mM, 100μL) and HAC-NaAC buffer (100μL, pH 4.0) were subsequently added and incubated for 5 minutes. Finally, a multi-mode reader was used to record the absorbance at 652 nm.

2.2.3 Intracellular imaging

For live/dead cell imaging, MDA-MB-231 cells were seeded in 6-well plates and incubated overnight at 37^oC in a cell culture incubator. Adding IIM-Fe-SASC nanoprobe or TMB with 10 mg/mL and 1 mM and incubate in the dark for 30 minutes, respectively. Subsequently, the calcein-AM (2 μM) and EthD-1 (4 μM) solutions from the live/dead viability kit were added to each well and incubated for 15 minutes. Finally, after washing thoroughly with PBS, observe the cells with CLSM (Leica TCS SP8). Here, the green fluorescence from Calcein-AM represents living cells, and the red fluorescence from EthD-1 represents dead cells. For the intracellular ROS imaging, DCFH-DA was used to stain cells as a ROS fluorescent probe. MDA-MB-231 cells were seeded in 12-well plates and incubated for 24 h in a cell culture incubator containing 5% CO_2 and 95%

humidity. Then the cells were incubated with IIM-Fe-SASC nanoprobe for 4 h under 0 μg mL-1, 2.5 μg mL^{-1}, 5 μg mL^{-1}, and 10 μg mL^{-1}, respectively. Herein, the IIM-Fe-SASC nanoprobe was broken down to nanosize via an intense ultrasound treatment for use in endocytosis. 10 μM DCFH-DA was added to each well, followed by incubation for 20 min. The cells were washed using PBS. Finally, fluorescence images were obtained by CLSM.

2.3. Results and discussion

2.3.1 Materials characterizations

Transmission electron microscopy (TEM) was used to study the structures and morphologies of as-prepared samples. **Figure 2.2** shows that well-defined mesoporous structures in both Fe-imprinted and non-Fe-imprinted mesoporous SiO_2 precursors. No obvious structural difference is found, indicating that the sol-gel polymerization and mesoporous SiO_2 precursor structures are not affected when adding Fe ions.
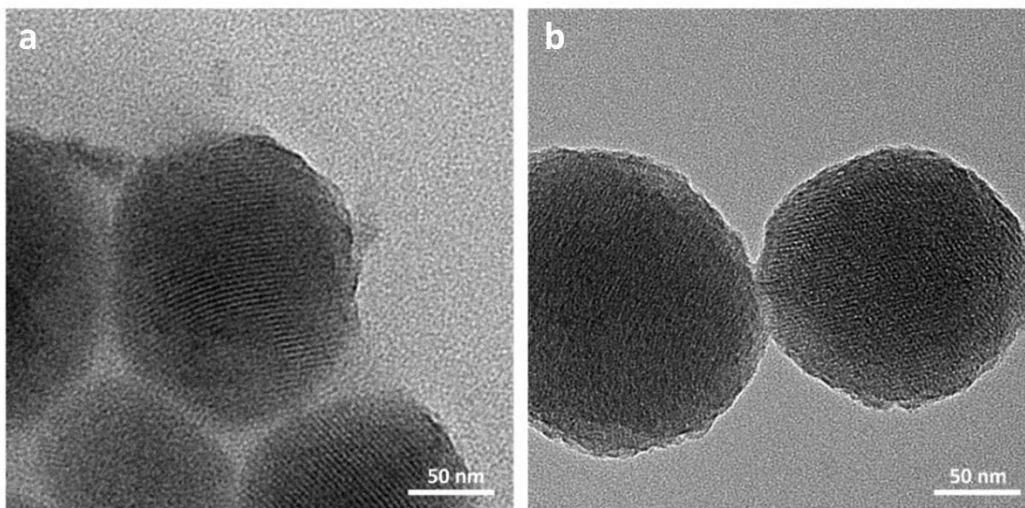
Figure 2.2 TEM images of Fe-doped (a) and without doped (b) mesoporous SiO_2 precursor.
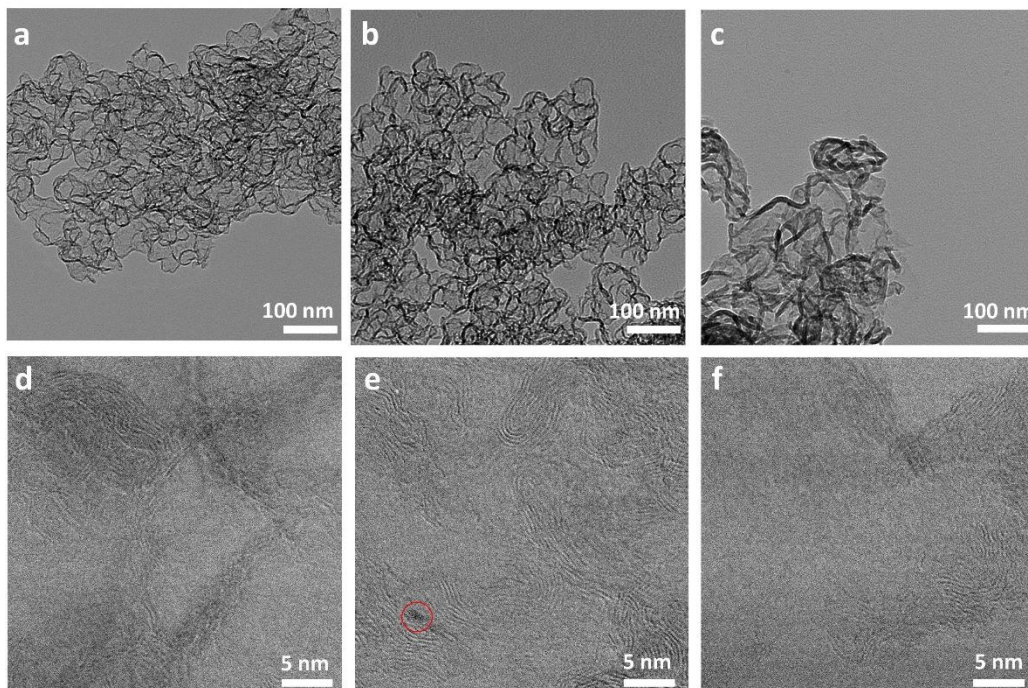
Figure 2.3 (a-c) TEM images of IIM-Fe-SASC, NIM-Fe-SASC, and NIM in different resolutions, respectively. (d-f) STEM bright-field images for IIM-Fe-SASC, NIM-Fe-SASC, and NIM at higher magnification, respectively.
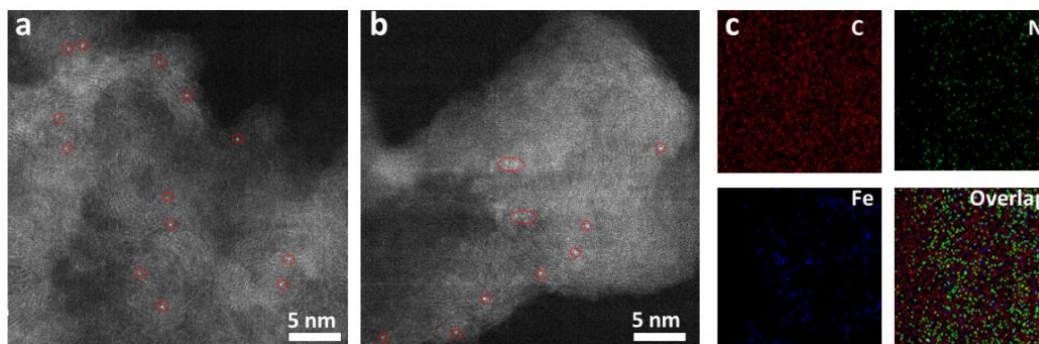
Figure 2.4 (a-b) HAADF-STEM images of IIM-Fe-SASC and NIM-Fe-SASC, respectively. (c) Elemental -mapping images of IIM-Fe-SASC.

The obtained IIM-Fe-SASC, NIM-Fe-SASC, and NIM show the inhomogeneous structure (**Figure 2.3a-c**). Moreover, in **Figure 2.3d** and **f**, distorted graphite layers were observed by scanning TEM (STEM), which makes the catalysts rich in defects and nanopores, thus accommodates a large amount of single-atomic active sites. The STEM images of IIM-Fe-SASC are the same as that of NIM, where no nanoparticles are observed, suggesting that iron atoms embed into the IIM-Fe-

SASC as dispersive isolated atoms. However, nanocrystal can be found in NIM-Fe-SASC and is marked in the red circle in **Figure 2.3e**, illustrating that the adsorption method can easily produce metal clusters and are hard to remove.

To further prove the state of single iron atom, aberration-corrected high-angle annular dark-field STEM (HAADF-STEM) was employed to investigate the wall structure of the as-made IIM-Fe-SASC and NIM-Fe-SASC at the atomic level. For IIM-Fe-SASC, as marked in red circles in **Figure 2.4a**, uniformly dispersed single-atomic Fe sites show on the carbon matrix. Nevertheless, NIM-Fe-SASC, prepared by the traditional adsorption method, has both single iron atoms and some stacked metal crystals (**Figure 2.4b**), further demonstrating that the doped Fe species are not purely single atoms. Elemental composition and distribution in IIM-Fe-SASC were detected by Auxiliary Energy-dispersive X-ray spectroscopy (EDS) elemental analysis. **Figure 2.4c** shows the corresponding element maps of carbon, nitrogen, and iron in IIM-Fe-SASC. All elements uniformly distribute in the IIM-Fe-SASC, indicating that nitrogen coordinated with Fe atoms can be doped into the carbon matrix.
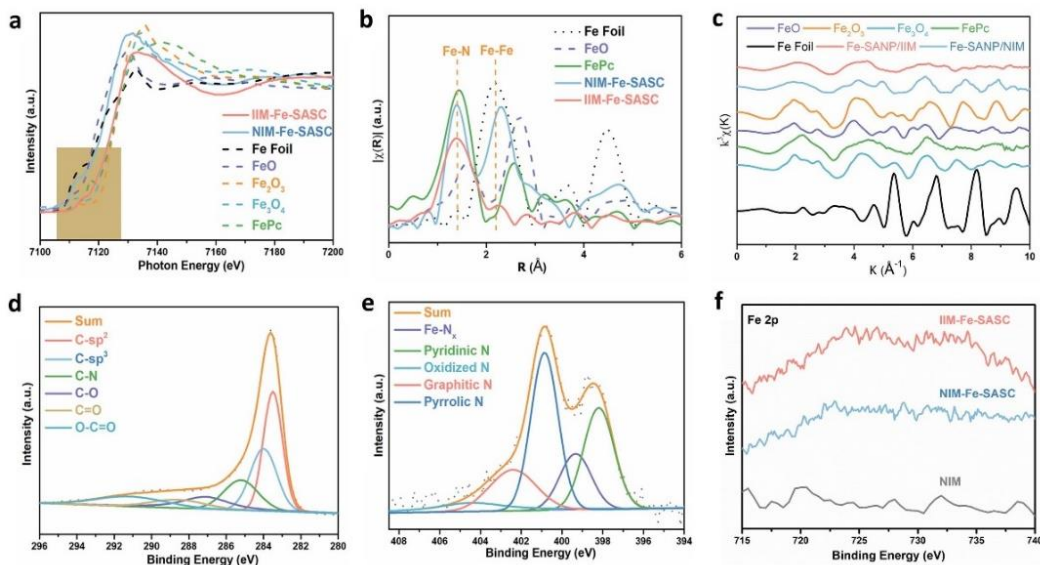
Figure 2.5 (a) Fe K-edge XANES spectra of IIM-Fe-SASC, and reference samples of FePc, Fe foil, FeO, Fe_2O_3, and Fe_3O_4. (b) FT k^2-weighted EXAFS R-space spectra of IIM-Fe-SASC, NIM-

X-ray absorption spectroscopy (XAS) measurements[35, 36] were performed to determine the local structural and electronic states of Fe atoms in the as-synthesized catalysts. The absorption edge of Fe K-edge X-ray absorption near edge structure (XANES) spectrum of IIM-Fe-SASC is located at higher energy compared to that of Fe foil, but in between two reference samples (FeO and Fe_2O_3), indicating that the Fe atoms in IIM-Fe-SASC have a positive charge (**Figure 2.5a**) that is between +2 and +3. Note that the absorption edge of IIM-Fe-SASC almost overlaps with that of FePc, which may indicate the similarity of their local structure surrounding Fe atoms.

Moreover, in **Figure 2.5b**, the Fourier-transformed (FT) k^2-weighted EXAFS curve of IIM-Fe-SASC only shows a main peak at about 1.4 Å, which is aligned with the Fe-N peak in the FePc reference sample, suggesting that Fe is in single-atom dispersed form with Fe-N bonding. In comparison, besides the Fe-N scattering path, a Fe-Fe peak at 2.2 Å (comparing with Fe foil) exists in NIM-Fe-SASC, demonstrating Fe exists as both Fe-N_x motifs and metallic Fe clusters. These results are consistent with the HAADF-STEM results shown above.

It is also noted that the k-space EXAFS oscillations (**Figure 2.5c**) reveal that IIM-Fe-SASC spectrum is different from those of Fe foil and Fe oxides, but similar to that of Fe single atom reference FePc, which mainly due to the fact that the selected functional monomers effectively coordinate iron atoms during the ion imprinting process.[23]

The chemical composition of the obtained IIM-Fe-SASC was conducted by X-ray photoelectron spectroscopy (XPS). The high-resolution C 1s spectrum of the IIM-Fe-SASC (**Figure 2.5d**) can be deconvoluted into four components of C-sp^2 (283.6 eV), C-sp^3 (284.0 eV), C-N (285.2 eV), C-O (287.1 eV), C=O (288.6 eV) and O-C=O (289.1 eV). [37-39] The ratio of C-sp^2 in IIM-Fe-SASC

is 33.4%, much lower than the reported high graphitized carbon materials (like graphene),[40, 41] indicating that the IIM-Fe-SASC has a lower degree of graphitization and abundant defects and edges. The complex N 1s spectrum of IIM-Fe-SASC is deconvoluted into several main peaks (**Figure 2.5e**), which correspond to pyridinic N (398.2 eV), pyrrolic N (400.9 eV), graphitic N (402.4 eV), and oxidized N (404.7 eV), respectively.[23, 42] Most important, a spectral valley between two dominating pyridinic peak and pyrrolic peak at 399.3 eV indicates the presence of Fe-N_x single-atomic sites,[43] which is in good agreement with the result of EXAFS. Besides, the Fe 2p spectra are shown in **Figure 2.5f**, which further illustrates the successful Fe doping.

2.3.2 Peroxidase-like activities evaluation

The peroxidase-like activities of the IIM-Fe-SASC, NIM-Fe-SASC, and NIM are verified, and the results of the chromogenic reaction are shown in **Figure 2.6a**. The obvious color change of IIM-Fe-SASC can be observed and is caused by the oxidation of colorless substrates to their corresponding oxidized products. Notably, NIM cannot trigger any chromogenic reaction regardless of the existence of H_2O_2, which proves that the peroxidase-like property of IIM-Fe-SASC is mainly originated from Fe-N_x sites. The peroxidase-like activity of IIM-Fe-SASC and control samples were conducted, the results are shown in **Figure 2.6b**. Absorbance at 652 nm increases along with reaction time, and linear relations with R^2 coefficient close to 1 are obtained by linear regression analysis during the first minute. It is clear that IIM-Fe-SASC has the best peroxidase-like catalytic performance.

Then the catalytic activities expressed in units (U) of IIM-Fe-SASC, NIM-Fe-SASC, and NIM were further evaluated (**Figure 2.6c**). The peroxidase-mimic activity of IIM-Fe-SASC is calculated to be 48.5 U mg^{-1}, which is much higher than that of NIM-Fe-SASC (16.6 U mg^{-1}) and NIM (4.4 U mg^{-1}). The peroxidase-mimic activity of IIM-Fe-SASC is more than ten-fold than that

of NIM, which further illustrates that the activity is derived from $Fe-N_x$ active sites. What's more, the huge activity gap between IIM-Fe-SASC and NIM-Fe-SASC proves that applying IIT results in relatively high-density atomic $Fe-N_x$ active sites, thus boosting the peroxidase-like performance. For comparison, the specific activity of natural HRP is evaluated to be 263.8 mg/mL under the same process, which is in accordance with the manufacture's value (≥ 250 U mg^{-1}), and the specific activity of the IIM-Fe-SASC is approaching that of natural HRP.

By comparing the detection performances of H_2O_2 (100 mM) and its interfering substrates (500 mM) of cysteine, ascorbic acid, NaCl, glucose, alanine, and sucrose, the selectivity of IIM-Fe-SASC towards H_2O_2 was revealed and shown in **Figure 2.6d**, indicating IIM-Fe-SASC has a satisfactory selectivity towards H_2O_2.
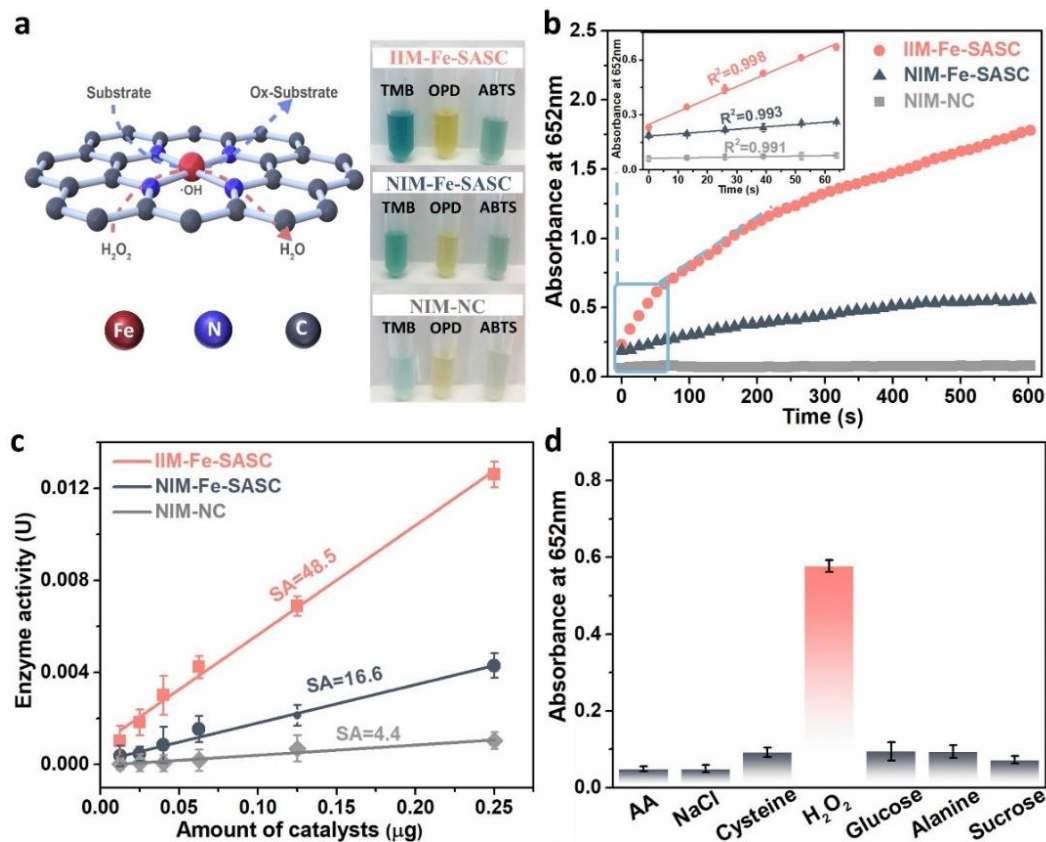
Figure 2.6 (a) Mechanism illustration of IIM-Fe-SASC catalyzed and chromogenic reaction with different substrates. (b) Absorbance-time curves and magnified initial linear portion of TMB chromogenic reaction catalyzed by IIM-Fe-SASC, NIM-Fe-SASC and NIM.(c) Specific

activities of IIM-Fe-SASC, NIM-Fe-SASC and NIM. (d) Specificity evaluation of IIM-Fe-SASC for various interferences

Furthermore, the steady-state kinetics curves of IIM-Fe-SASC towards H_2O_2 and TMB substrates were obtained and shown in **Figure 2.7a** and **b**. Michaelis-Menten parameters of IIM-Fe-SASC and nature HRP towards TMB and H_2O_2 are obtained (**Table 2.1**). IIM-Fe-SASC shows a comparable K_m towards H_2O_2 compare with natural HRP, and K_m of IIM-Fe-SASC to TMB is lower than that of natural HRP, indicating the IIM-Fe-SASC has a higher affinity toward TMB and a similar affinity level towards H_2O_2. As shown in **Figure 2.7c** and **d** IIM-Fe-SASC can preserve their activity in a wide pH range of 2.5-8.5, while maintained above 80% activity from 4 to 80°C, which shows satisfaction robustness against the harsh environment.
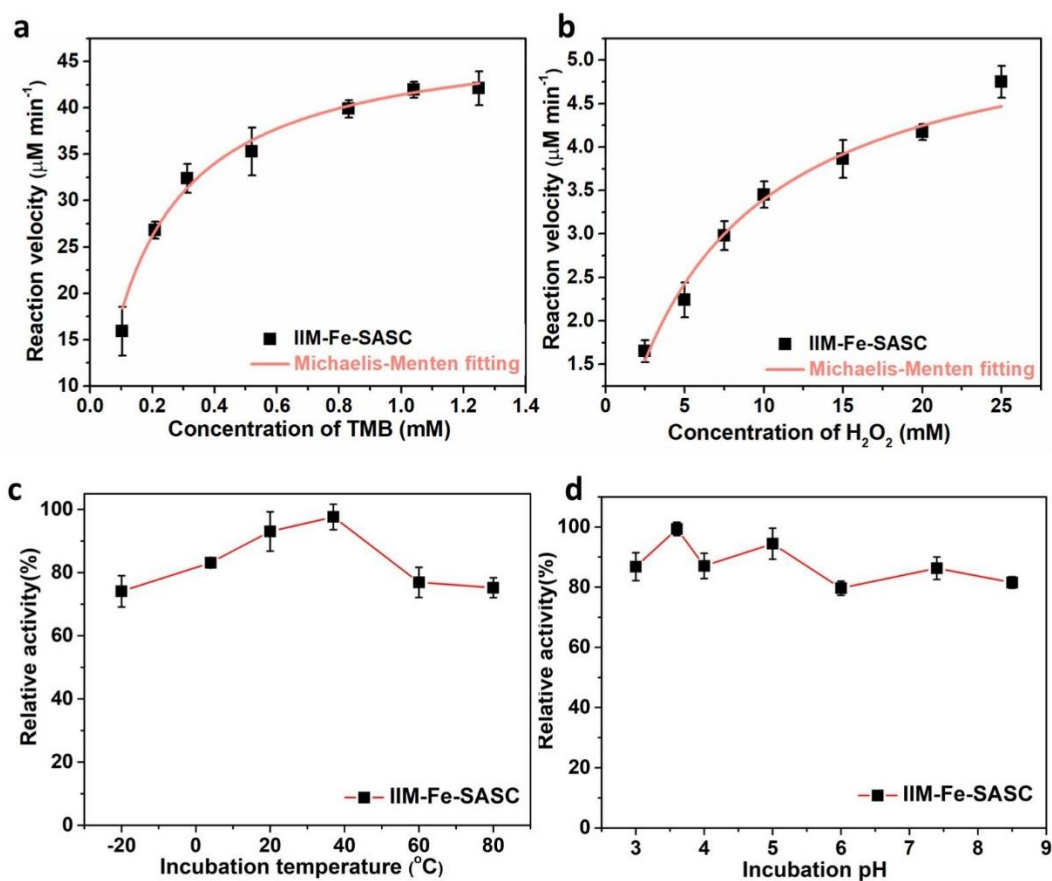
Figure 2.7 (a) and (b) Steady-state kinetics curves of IIM-Fe-SASC toward TMB and H_2O_2, respectively. (c) and (d) Robustness of IIM-Fe-SASC against the harsh environment of temperature and pH, respectively.

Table 2.1. Steady-state kinetics parameters of IIM-Fe-SASC and the natural HRP.

Materials	[E] (M)	Substrate	K_m (mM)	v_{max} ($\mu M\ min^{-1}$)	K_{cat} (min^{-1})	K_{cat}/K_m ($M^{-1}\ min^{-1}$)
IIM-Fe-SASC	2.23×10^{-11}	H_2O_2	6.63	5.65	2.49×10^5	3.7×10^7
		TMB	0.17	48.45	2.17×10^5	12.8×10^9
Natural HRP	5.2×10^{-11}	H_2O_2	4.52	64.08	1.23×10^6	27.2×10^7
		TMB	0.439	75.51	1.45×10^6	3.3×10^9

2.3.3 Mechanisms for peroxidase-like activity

Thiocyanate ions (SCN^-) were used to evaluate the role of single atom Fe in catalytic efficiency because SCN^- and Fe-centered catalytic sites can form a stable chelate complex, thereby block Fe activity sites, and fail to decompose H_2O_2. The mechanism illustration is in **Figure 2.8a**. [44].

As shown in **Figure 2.8b**, the inhibitory effect of peroxidase-like activity is significantly enhanced with the increase of SCN^-. These results further prove that the peroxidase-like activity of Fe-SASC is mainly generated from the atomically dispersed $Fe-N_x$ active sites, which is consistent with the huge specific activity difference in **Figure 2.7c**.

The active intermediates were also investigated using various scavengers (**Figure 2.8c-f**). In **Figure 2.8c**, the absorbance value of ox-TMB decreases significantly with the addition of NaN_3, indicating that the participation of $\cdot OH/^1O_2$ is related to the oxidation coloration reaction. [45] The generated $\cdot OH$ was detected by the enhanced isopropanol inhibition ability (**Figure 2.8d**). The higher fluorescent signal of terephthalic acid (TA) catalyzed by IIM-Fe-SASC nanoprobe demonstrated that more $\cdot OH$ is generated (**Figure 2.8e**). [46, 47] Besides, experimental results related to β-carotene verified the little presence of $^1O_2$ (**Figure 2.8f**). [48]
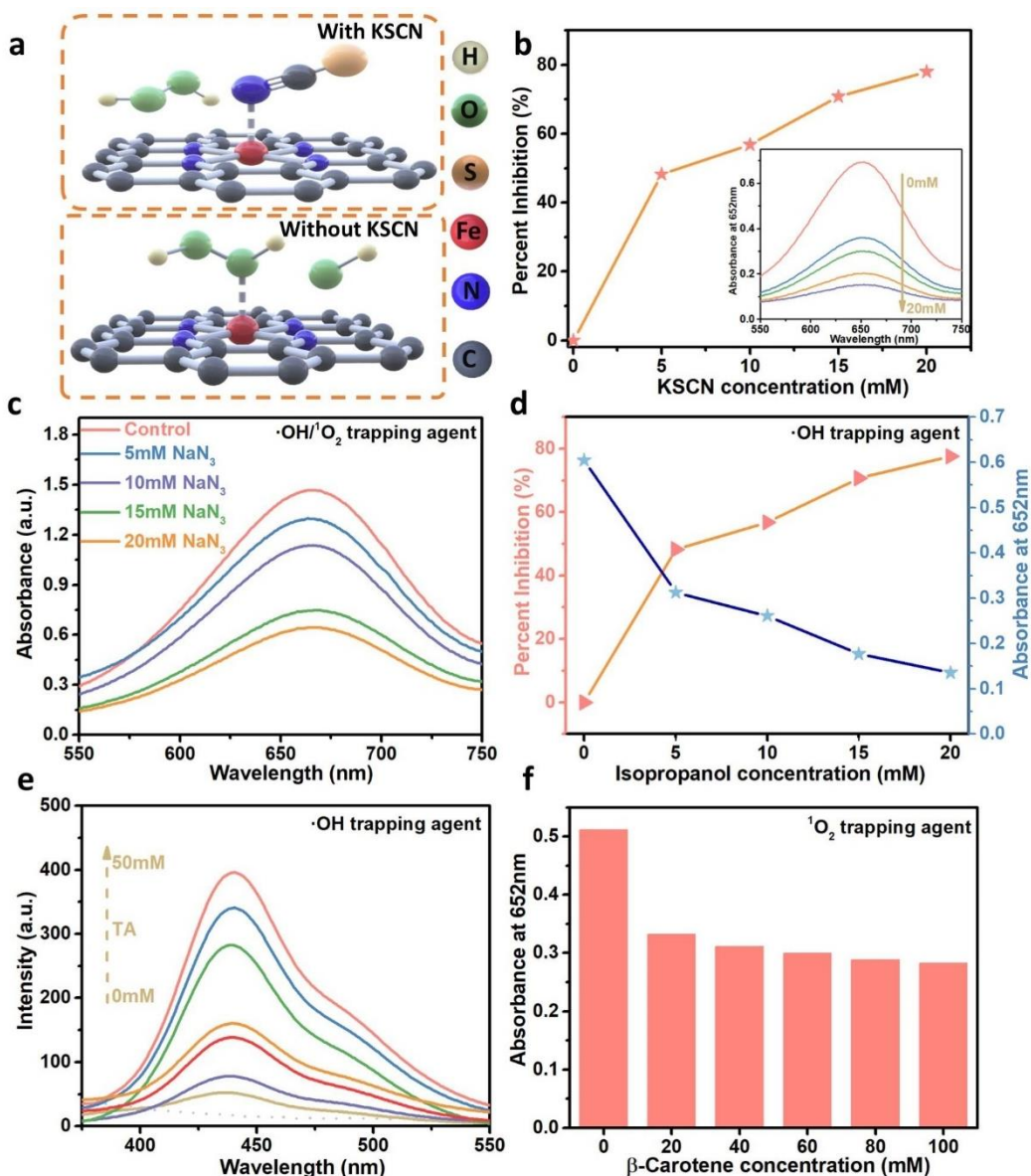
Figure2.8 (a) Schematic illustration of the mechanism of KSCN influence. (b) Percent inhibition and absorption change of IIM-Fe-SASC+TMB+H$_2$O$_2$ solution upon the addition of various concentrations of KSCN. (c) Absorbance changes after adding various amounts of NaN$_3$. (d) Percent inhibition and absorption change after adding isopropanol. (e) TA as a •OH fluorescent probe. (f) Absorption changes after adding β-carotene with different concentrations.

2.3.4 Biocompatibility of IIM-Fe-SASC nanoprobe

A standard MTT assay was carried out to verify the potential toxicity of TMB and IIM-Fe-SASC (**Figure 2.9a-c**). It is clear that the added TMB has little effect on cell viability. Furthermore, after 24 hours of incubation in IIM-Fe-SASC with a concentration range of 1.0 to 10 μg mL^{-1}, MDA-

MB-231 cells can still retain their high viability, revealing the excellent biocompatibility of IIM-Fe-SASC. A standard staining method was also used to evaluate the biocompatibility by a live/dead viability kit. The calcein-AM can combine with the living cell through the cell membrane and green fluorescence can be observed in the cytoplasm through a fluorescent microscope. As shown in **Figure 2.9d**, MDA-MB-231 cells were cultured with IIM-Fe-SASC nanoprobe and TMB under testing concentrations. The CLSM images show that the TMB has minor effects on cell viability. And for IIM-Fe-SASC nanoprobe, no significant cell viability changes.
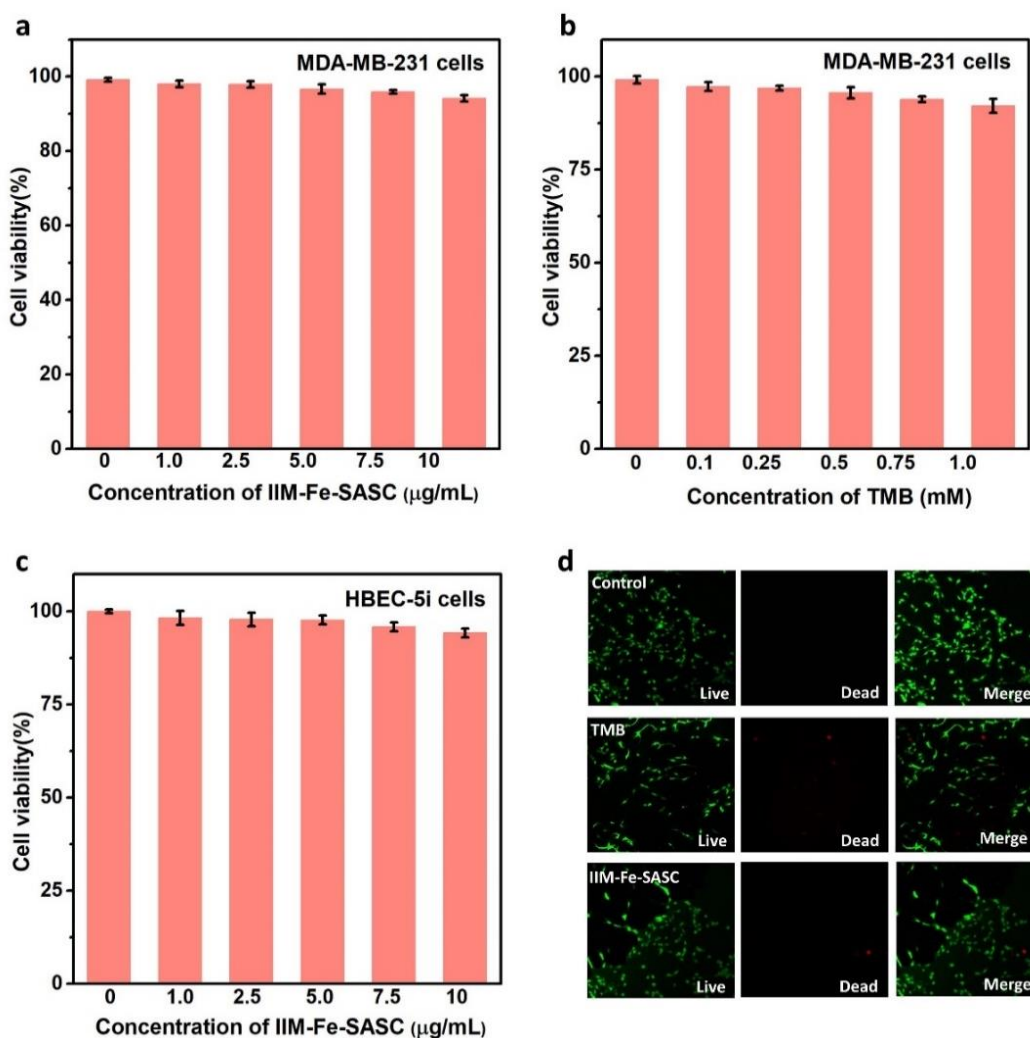
Figure 2.9 MTT assay of IIM-Fe-SASC in MDA-MB-231 cells (a), TMB in MDA-MB-231 cells (b), and IIM-Fe-SASC in HBEC-5i cells (c), respectively. (e)Fluorescence imaging of MDA-MB-231 cancer cells cultured with TMB and IIM-Fe-SASCs nanoprobe.

2.3.5 Hydrogen peroxide detection in living cells

The linear detection range of IIM-Fe-SASC nanoprobe to H_2O_2 is determined and the results are shown in **Figure 2.10a**. Accordingly, a fine linear relationship of H_2O_2 concentration to absorbance curve is achieved in the range of 0.25 - 5 mM (**Figure 2.10b**). The MDA-MB-231 breast cancer cells were used for intracellular hydrogen peroxide detection. First, Adenosine-5-diphosphate (ADP), N-formylmethionyl-leucyl-phenylalanine (fMLP), and phorbol-12-myristate-13-acetate (PMA) were used to stimulate MDA-MB-231 cells and the released H_2O_2 were detected (**Figure 2.10c**), in which PMA exhibited the optimal stimuli.[49]

Then PMA was then selected to treat MDA-MB-231 cells under different concentrations. The results in **Figure 2.10d** show that the absorbance value is highly dependent on PMA concentrations. Furthermore, different cell numbers were treated with or without PMA. A higher colorimetric response is observed as the cell number increased, which can be ascribed to more H_2O_2 produced during PMA stimulation (**Figure 2.10e**).

Also, according to the H_2O_2 detection calibration curve in **Figure 2.10b**, H_2O_2 concentration produced from the MDA-MB-231 cells (2.5×10^5 cells/plate) is calculated to be 4.92 mM. This value is in good agreement with the previous reports,[47, 50] indicating that the colorimetric detection method based on IIM-Fe-SASC nanoprobe can be used in practical clinic applications. Intracellular H_2O_2 detection was also performed through transporting IIM-Fe-SASC nanoprobe into MDA-MB-231 cells by endocytosis. Since we have already proved that the $\cdot OH$ and $^1O_2$ are active intermediates during the peroxidase-like catalytic reaction, these intracellular reactive oxygen species can be evaluated using a fluorescence probe 2′,7′-dichlorofluorescein diacetate (DCFH-DA).[51]
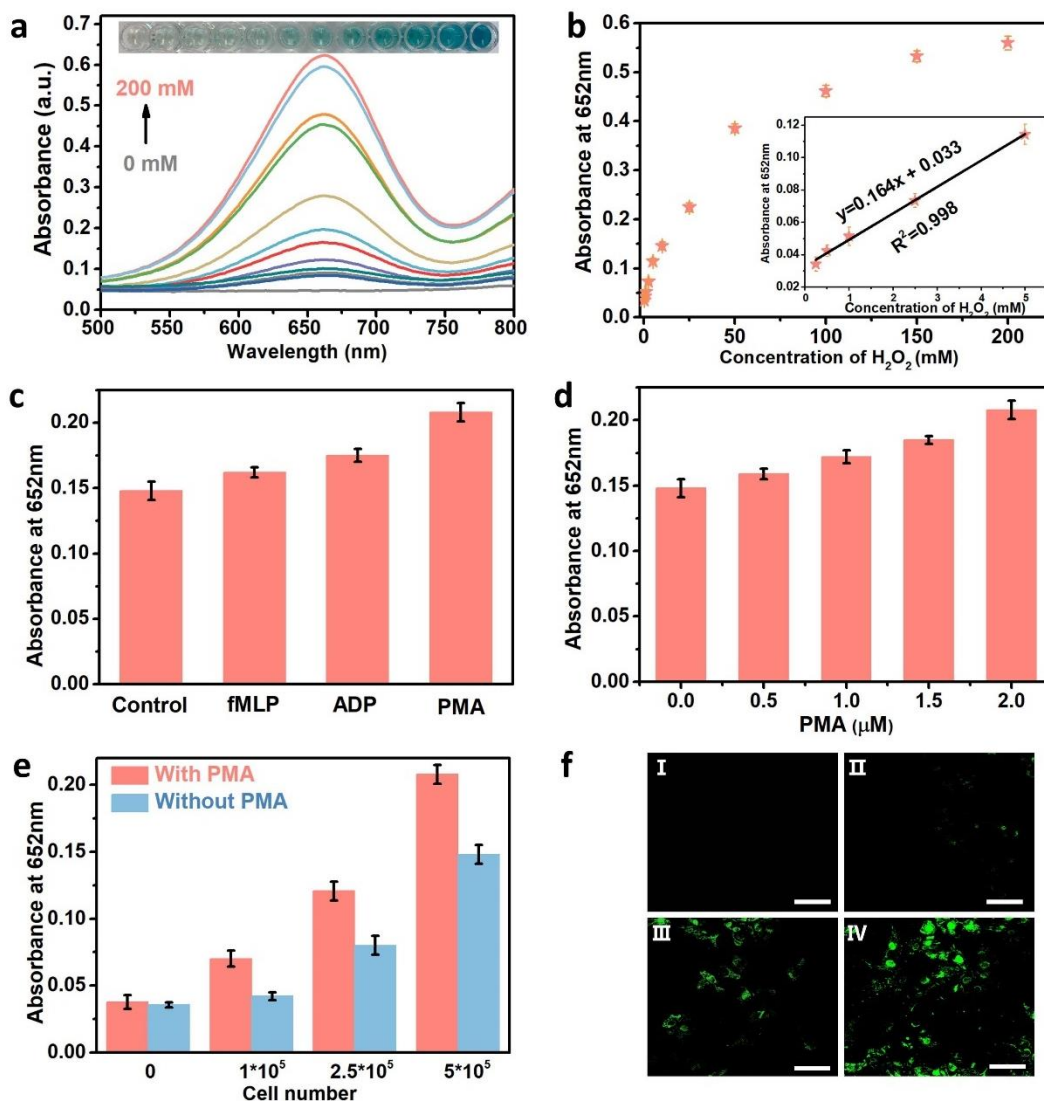
Figure 2.10 (a) UV-vis spectra of TMB oxidized by the IIM-Fe-SASC under different H_2O_2 concentrations. (b) Absorbance changes and linear calibration plot (inset) for H_2O_2 detection. (c) Absorbance values of ox-TMB toward the fMLP, ADP, and PMA. (d) Absorbance values of H_2O_2 generated from MDA-MB-231 cells after treating with various concentrations of PMA. (e) Absorbance comparison toward MDA and PMA-treated MDA-MB-231 cells. (f) CLSM images of active intermediates generated in MDA-MB-231 cells treated with different amount of IIM-Fe-SASC nanoprobe (I: 0 μg mL^{-1}; II: 2.5 μg mL^{-1}; III: 5 μg mL^{-1}; IV: 10 μg mL^{-1}). The intracellular ROS generation was detected by the DCFH-DA (Scale bar: 60 μm).

As illustrated in **Figure 2.10f**, MDA-MB-231 cells show insignificant green fluorescence when

incubating with IIM-Fe-SASC nanoprobe. In contrast, obvious green fluorescence is observed in

control cells, suggesting IIM-Fe-SASC nanoprobe can produce massive intracellular active

intermediates. In addition, the intensity of the green fluorescence signal is also enhanced with the increasing concentration of nanoprobes. These results further demonstrate the excellent intracellular H_2O_2 detection ability of IIM-Fe-SASC nanoprobe.

2.4 Conclusion

In summary, we have used a facile ion-imprinting approach to synthesize a Fe-based single-atomic nanoprobe for hydrogen peroxide detection in living cells. The resultant IIM-Fe-SASC shows better peroxidase-like activity than that of non-imprinted references, demonstrating that the ion-imprinting process can precisely control ion at the atomic level and form numerous well-defined single-atom iron. High sensitivity and specificity of IIM-Fe-SASC nanoprobe have been achieved for colorimetric detection of H_2O_2. Furthermore, *in situ* detection of H_2O_2 generated from the MDA-MB-231 cells was performed, exhibiting satisfactory sensitivity and specificity. This work opens a novel and easy route in designing advanced single atom nanoprobe and expands their biosensing applications.

REFERENCES

1. H. Ohshima, M. Tatemichi, T. Sawa. Chemical basis of inflammation-induced carcinogenesis, Archives of Biochemistry and Biophysics, 417 (2003) 3-11.

2. J. Bai, X. Jiang. A facile one-pot synthesis of copper sulfide-decorated reduced graphene oxide composites for enhanced detecting of H_2O_2 in biological environments, Analytical Chemistry, 85 (2013) 8095-8101.

3. Q. Chen, C. Liang, X. Sun, J. Chen, Z. Yang, H. Zhao, L. Feng, Z. Liu. H_2O_2-responsive liposomal nanoprobe for photoacoustic inflammation imaging and tumor theranostics via in vivo chromogenic assay, Proceedings of the National Academy of Sciences, 114 (2017) 5343-5348.

4. T. Finkel, M. Serrano, M. A. Blasco. The common biology of cancer and ageing, Nature, 448 (2007) 767-774.

5. T. Zhang, Y. Xing, Y. Song, Y. Gu, X. Yan, N. Lu, H. Liu, Z. Xu, H. Xu, Z. Zhang, M. Yang. AuPt/MOF-graphene: A synergistic catalyst with surprisingly high peroxidase-like activity and its application for H_2O_2 detection, Analytical Chemistry, 91 (2019) 10589-10595.

6. J. Liu, J. Liang, C. Wu, Y. Zhao. A doubly-quenched fluorescent probe for low-background detection of mitochondrial H_2O_2, Analytical Chemistry, 91 (2019) 6902-6909.

7. Z. Deng, Y. Qian, Y. Yu, G. Liu, J. Hu, G. Zhang, S. Liu. Engineering intracellular delivery nanocarriers and nanoreactors from oxidation-responsive polymersomes via synchronized bilayer cross-linking and permeabilizing inside live cells, Journal of the American Chemical Society, 138 (2016) 10452-10466.

8. Q. Fu, H. Saltsburg, M. Flytzani-Stephanopoulos. Active nonmetallic Au and Pt species on ceria-based water-gas shift catalysts, Science, 301 (2003) 935-938.

9. C. Zhu, S. Fu, Q. Shi, D. Du, Y. Lin. Single-atom electrocatalysts, Angewandte Chemie International Edition, 56 (2017) 13944-13960.

10. L. Jiao, W. Xu, Y. Wu, H. Yan, W. Gu, D. Du, Y. Lin, C. Zhu. Single-atom catalysts boost signal amplification for biosensing, Chemical Society Reviews, 50 (2021) 750-765.

11. B. Qiao, A. Wang, X. Yang, L. F. Allard, Z. Jiang, Y. Cui, J. Liu, J. Li, T. Zhang. Single-atom catalysis of co oxidation using Pt1/FeO$_x$, Nature Chemistry, 3 (2011) 634-641.

12. S. Ji, Y. Chen, X. Wang, Z. Zhang, D. Wang, Y. Li. Chemical synthesis of single atomic site catalysts, Chemical Reviews, 120 (2020) 11900-11955.

13. F. X. Hu, T. Hu, S. Chen, D. Wang, Q. Rao, Y. Liu, F. Dai, C. Guo, H. B. Yang, C. M. Li. Single-atom cobalt-based electrochemical biomimetic uric acid sensor with wide linear range and ultralow detection limit, Nano-Micro Letters, 13 (2020) 7.

14. H. Zhang, W. Zhou, T. Chen, B. Y. Guan, Z. Li, X. W. Lou. A modular strategy for decorating isolated cobalt atoms into multichannel carbon matrix for electrocatalytic oxygen reduction, Energy & Environmental Science, 11 (2018) 1980-1984.

15. L. Huang, J. Chen, L. Gan, J. Wang, S. Dong. Single-atom nanozymes, Science Advances, 5 (2019) eaav5490.

16. L. Jiao, H. Yan, Y. Wu, W. Gu, C. Zhu, D. Du, Y. Lin. When nanozymes meet single-atom catalysis, Angewandte Chemie, 132 (2020) 2585-2596.

17. S. Lin, H. Wei. Design of high performance nanozymes: A single-atom strategy, Science China Life Sciences, 62 (2019) 710-712.

18. W. Wu, L. Huang, E. Wang, S. Dong. Atomic engineering of single-atom nanozymes for enzyme-like catalysis, Chemical Science, 11 (2020) 9741-9756.

19. X. Niu, Q. Shi, W. Zhu, D. Liu, H. Tian, S. Fu, N. Cheng, S. Li, J. N. Smith, D. Du, Y. Lin. Unprecedented peroxidase-mimicking activity of single-atom nanozyme with atomically dispersed Fe-N$_x$ moieties hosted by mof derived porous carbon, Biosensors and Bioelectronics, 142 (2019) 111495.

20. Y. Chen, L. Jiao, H. Yan, W. Xu, Y. Wu, H. Wang, W. Gu, C. Zhu. Hierarchically porous S/N codoped carbon nanozymes with enhanced peroxidase-like activity for total antioxidant capacity biosensing, Analytical Chemistry, 92(2020) 13518-13524.

21. L. Jiao, W. Xu, Y. Zhang, Y. Wu, W. Gu, X. Ge, B. Chen, C. Zhu, S. Guo. Boron-doped Fe-N-C single-atom nanozymes specifically boost peroxidase-like activity, Nano Today, 35 (2020) 100971.

22. N. Cheng, J.-C. Li, D. Liu, Y. Lin, D. Du. Single-atom nanozyme based on nanoengineered Fe-N-C catalyst with superior peroxidase-like activity for ultrasensitive bioassays, Small, 15 (2019) 1901485.

23. R. Jiang, L. Li, T. Sheng, G. Hu, Y. Chen, L. Wang. Edge-site engineering of atomically dispersed Fe-N$_4$ by selective C-N bond cleavage for enhanced oxygen reduction reaction activities, Journal of the American Chemical Society, 140 (2018) 11594-11598.

24. H. Zhang, J. Li, S. Xi, Y. Du, X. Hai, J. Wang, H. Xu, G. Wu, J. Zhang, J. Lu. A graphene-supported single-atom FeN$_5$ catalytic site for efficient electrochemical CO$_2$ reduction, Angewandte Chemie, 131 (2019) 15013-15018.

25. J. Han, J. Bian, C. Sun. Recent advances in single-atom electrocatalysts for oxygen reduction reaction, Research, 2020 (2020) 9512763.

26. Y. Qu, L. Wang, Z. Li, P. Li, Q. Zhang, Y. Lin, F. Zhou, H. Wang, Z. Yang, Y. Hu, M. Zhu, X. Zhao, X. Han, C. Wang, Q. Xu, L. Gu, J. Luo, L. Zheng, Y. Wu. Ambient synthesis of single-

atom catalysts from bulk metal via trapping of atoms by surface dangling bonds, Advanced Materials, 31 (2019) 1904496.

27. J.-C. Li, Z.-Q. Yang, D.-M. Tang, L. Zhang, P.-X. Hou, S.-Y. Zhao, C. Liu, M. Cheng, G.-X. Li, F. Zhang, H.-M. Cheng. N-doped carbon nanotubes containing a high concentration of single iron atoms for efficient oxygen reduction, NPG Asia Materials, 10 (2018) e461-e461.

28. J. Han, H. Bao, J.-Q. Wang, L. Zheng, S. Sun, Z. L. Wang, C. Sun. 3D N-doped ordered mesoporous carbon supported single-atom Fe-N-C catalysts with superior performance for oxygen reduction reaction and zinc-air battery, Applied Catalysis B: Environmental, 280 (2021) 119411.

29. X.-F. Yang, A. Wang, B. Qiao, J. Li, J. Liu, T. Zhang. Single-atom catalysts: A new frontier in heterogeneous catalysis, Accounts of Chemical Research, 46 (2013) 1740-1748.

30. J. Fu, L. Chen, J. Li, Z. Zhang. Current status and challenges of ion imprinting, Journal of Materials Chemistry A, 3 (2015) 13598-13627.

31. N. Zhang, N. Zhang, Y. Xu, Z. Li, C. Yan, K. Mei, M. Ding, S. Ding, P. Guan, L. Qian, C. Du, X. Hu. Molecularly imprinted materials for selective biological recognition, Macromolecular Rapid Communications, 40 (2019) 1900096.

32. S. Ding, Z. Lyu, X. Niu, Y. Zhou, D. Liu, M. Falahati, D. Du, Y. Lin. Integrating ionic liquids with molecular imprinting technology for biorecognition and biosensing: A review, Biosensors and Bioelectronics, 149 (2020) 111830.

33. Y. Berro, S. Gueddida, Y. Bouizi, C. Bellouard, E.-E. Bendeif, A. Gansmuller, A. Celzard, V. Fierro, D. Ihiawakrim, O. Ersen, M. Kassir, F. El Haj Hassan, S. Lebegue, M. Badawi, N. Canilho, A. Pasc. Imprinting isolated single iron atoms onto mesoporous silica by templating with metallosurfactants, Journal of Colloid and Interface Science, 573 (2020) 193-203.

34. S. Ding, Z. Lyu, H. Zhong, D. Liu, E. Sarnello, L. Fang, M. Xu, M. H. Engelhard, H. Tian, T. Li. An ion-imprinting derived strategy to synthesize single-atom iron electrocatalysts for oxygen reduction, Small, 17 (2020) 2004454.

35. H. Zhang, W. Zhou, X. F. Lu, T. Chen, X. W. Lou. Implanting isolated ru atoms into edge-rich carbon matrix for efficient electrocatalytic hydrogen evolution, Advanced Energy Materials, 10 (2020) 2000882.

36. J. Li, H. Zhang, W. Samarakoon, W. Shan, D. A. Cullen, S. Karakalos, M. Chen, D. Gu, K. L. More, G. Wang. Thermally driven structure and performance evolution of atomically dispersed FeN_4 sites for oxygen reduction, Angewandte Chemie, 131 (2019) 19147-19156.

37. R. Li, Z. Wei, X. Gou. Nitrogen and phosphorus dual-doped graphene/carbon nanosheets as bifunctional electrocatalysts for oxygen reduction and evolution, ACS Catalysis, 5 (2015) 4133-4142.

38. S. Yi, X. Qin, C. Liang, J. Li, R. Rajagopalan, Z. Zhang, J. Song, Y. Tang, F. Cheng, H. Wang, M. Shao. Insights into $KMnO_4$ etched n-rich carbon nanotubes as advanced electrocatalysts for Zn-air batteries, Applied Catalysis B: Environmental, 264 (2020) 118537.

39. J. Han, X. Meng, L. Lu, J. Bian, Z. Li, C. Sun. Single-atom $Fe-N_x-C$ as an efficient electrocatalyst for zinc-air batteries, Advanced Functional Materials, 29 (2019) 1808872.

40. L. Tao, Q. Wang, S. Dou, Z. Ma, J. Huo, S. Wang, L. Dai. Edge-rich and dopant-free graphene as a highly efficient metal-free electrocatalyst for the oxygen reduction reaction, Chemical Communications, 52 (2016) 2764-2767.

41. P. Hao, Z. Zhao, Y. Leng, J. Tian, Y. Sang, R. I. Boughton, C. P. Wong, H. Liu, B. Yang. Graphene-based nitrogen self-doped hierarchical porous carbon aerogels derived from chitosan for high performance supercapacitors, Nano Energy, 15 (2015) 9-23.

42. J. Wang, F. Ciucci. Boosting bifunctional oxygen electrolysis for N-doped carbon via bimetal addition, Small, 13 (2017) 1604103.

43. N. Leonard, W. Ju, I. Sinev, J. Steinberg, F. Luo, A. S. Varela, B. Roldan Cuenya, P. Strasser. The chemical identity, state and structure of catalytically active centers during the electrochemical CO_2 reduction on porous Fe-nitrogen-carbon (Fe-N-C) materials, Chemical Science, 9 (2018) 5064-5073.

44. Y. Wang, K. Qi, S. Yu, G. Jia, Z. Cheng, L. Zheng, Q. Wu, Q. Bao, Q. Wang, J. Zhao, X. Cui, W. Zheng. Revealing the intrinsic peroxidase-like catalytic mechanism of heterogeneous single-atom CO-MoS_2, Nano-Micro Letters, 11 (2019) 102.

45. Y. Zhan, Y. Zeng, L. Li, L. Guo, F. Luo, B. Qiu, Y. Huang, Z. Lin. Cu^{2+}-modified boron nitride nanosheets-supported subnanometer gold nanoparticles: An oxidase-mimicking nanoenzyme with unexpected oxidation properties, Analytical Chemistry, 92 (2020) 1236-1244.

46. H. Wang, S. Jiang, W. Shao, X. Zhang, S. Chen, X. Sun, Q. Zhang, Y. Luo, Y. Xie. Optically switchable photocatalysis in ultrathin black phosphorus nanosheets, Journal of the American Chemical Society, 140 (2018) 3474-3480.

47. L. Jiao, J. Wu, H. Zhong, Y. Zhang, W. Xu, Y. Wu, Y. Chen, H. Yan, Q. Zhang, W. Gu, L. Gu, S. P. Beckman, L. Huang, C. Zhu. Densely isolated FeN_4 sites for peroxidase mimicking, ACS Catalysis, 10 (2020) 6422-6429.

48. H. Tamura, H. Ishikita. Quenching of singlet oxygen by carotenoids via ultrafast superexchange dynamics, The Journal of Physical Chemistry A, 124 (2020) 5081-5088.

49. Q. Shi, Y. Song, C. Zhu, H. Yang, D. Du, Y. Lin. Mesoporous pt nanotubes as a novel sensing platform for sensitive detection of intracellular hydrogen peroxide, ACS Applied Materials & Interfaces, 7 (2015) 24288-24295.

50. L. Jiao, W. Xu, H. Yan, Y. Wu, C. Liu, D. Du, Y. Lin, C. Zhu. Fe-N-C single-atom nanozymes for the intracellular hydrogen peroxide detection, Analytical Chemistry, 91 (2019) 11994-11999.

51. X. Cai, S. Ding, Q. Shi, Z. Lyu, D. Liu, W.-j. Dong, M. Du, P. Dutta, Y. Song, D. Du, Y. Lin. "Eyeball-like yolk–shell bimetallic nanoparticles for synergistic photodynamic–photothermal therapy". ACS Applied Bio Materials 2020, 3(9), 5922-592.

CHAPTER THREE: SINGLE-ATOMIC SITE CATALYST ENHANCED IMMUNOSORBENT

ASSAY FOR ALZHEIMER'S DISEASE DETECTION

This chapter is published as: **Zhaoyuan Lyu**, Shichao Ding, Nan Zhang, Yang Zhou, Nan Cheng,

Maoyu Wang, Mingjie Xu, Zhenxing Feng, Xiangheng Niu, Yuan Cheng, Chao Zhang, Dan Du,

Yuehe Lin. Single-Atom Nanozymes Linked Immunosorbent Assay for Sensitive Detection of A

β 1-40: A Biomarker of Alzheimer's Disease. *Research*, **2020**, 2020.

Contributions: **Zhaoyuan Lyu**: Conceptualization, Methodology, Investigation, Formal analysis,

Validation, Writing-original draft, Writing-review & editing. Shichao Ding: Resources, Formal

analysis, Investigation, Validation, Writing-review & editing. Nan Zhang: Resources. Yang Zhou:

Writing-review & editing. Nan Cheng: Writing-review & editing. Maoyu Wang: Resources.

Mingjie Xu: Resources. Zhenxing Feng: Resources. Xiangheng Niu: Writing-review & editing.

Yuan Cheng: Resourse. Chao Zhang: Resources. Dan Du: Supervision, Writing-review & editing,

Project administration, Funding acquisition. Yuehe Lin: Conceptualization, Supervision, Project

administration, Writing-review & editing, Funding acquisition.

3.1 Introduction

Alzheimer's disease (AD) is a neurodegenerative brain disease that induces significant issues with

thinking, learning, memory, or other cognitive skills. AD is extremely threatening to human health

and reduces the life quality of aged people.[1, 2] Based on the report released by the Alzheimer's

Association, approximately 5.8 million Americans have AD and this number is predicted to rise

to 14 million in 2050, which makes the studying of AD a hot spot for governments and scholars.[3]

Moreover, AD begins in the human body years before symptoms present, hence, diagnosing and

detecting this disease in advance will have great importance for clinical treatment.[4, 5] Nowadays,

although the cause of AD is not fully understood, it is believed that AD is associated with self-

association and deposition of amyloid β peptide (Aβ). Among them, amyloid beta 1-40 (Aβ1-40) is the most plentiful existed form in humans and easy to form the insoluble toxic Aβ1-40 aggregation, which is usually regarded as vital neuropathological hallmarks of AD.[6-8] Therefore, Aβ1-40 is usually qualified to serve as one of the diagnostic biomarkers and can be used to estimate the risk or show the presence of AD at the early stage.[9, 10]

Typically, Aβ1-40 could be detected in cerebrospinal fluid (CSF), serum and plasma and serves as an objective and reliable indicator of AD's progression.[11] Normally, serum detection is undoubtedly the top choice owing to its superior convenience and less pain to the patient. The commonly used technology is neuroimaging techniques,[12] while the high price limits its widespread use in patients.

Currently, detecting electric signals like electrical impedimetric, electrochemiluminescence and localized surface plasmon resonance is regarded as an effective method.[13-15] Nevertheless, the operation process is complicated and lacks an established standard. With advancements in on-site and on-line techniques, commercial enzyme-linked immunosorbent assay (ELISA) has established a widely recognized standard in food safety, clinical diagnose, and environmental evaluation due to its high specificity and accuracy.[11, 16] Its work mechanism is converting the interactions between antigen and antibody into visible color change so one can easily get the results from observation. However, some limitations of ELISA have to be considered in the practical application, such as high cost of enzymes, prolonged incubation time, and moderate sensitivity. Moreover, it is challenging for ELISA to achieve accurate detection because of the ultralow concentration of biomarkers in the early stages of diseases and for enzymes as horseradish peroxidase (HRP) used in commercial ELISA, its performance is highly dependent on pH and

temperature.[17-19] Hence, the probing of stable and low-cost enzyme-like materials to develop ELISA with high sensitivity needs to be addressed.

Nowadays, nanomaterials with enzyme-like characteristics have been selected as the potential next-generation artificial enzymes candidate.[20] Owing to their high stability and low cost compared with natural enzymes,[21, 22] they have attracted huge attention in fields of biosensing,[23] biotherapy,[24] and environmental treatment.[21, 22, 25] Up to now, extensive endeavors have been undertaken to develop novel ELISA by using various kinds of enzyme-like nanomaterials.[26] Recently, attention has been turned to Fe-N_x single atomic site catalysts (Fe-N_x SASCs) with peroxidase-like activity, which have been developed to achieve theoretically maximum atom utilization and utilized as a promising alternative to natural HRP.[27, 28] In Chapter 2, we have demonstrated the high peroxidase-mimicking effect of some SASCs.[29]

Inspired by the idea above, a novel high-density Fe-N_x single atom peroxidase-like catalyst (Fe-N_x SASCs) was successfully fabricated from pyrolyzed polypyrrole (PPy) nanotube via nanoconfined strategy. A series of analysis revealed the ultrahigh surface area and superior peroxidase-like activity. What's more, the peroxidase-like catalytic activity of the Fe-N_x SASCs was optimized and compared with natural HRP, which showed better thermal and pH stable catalytic properties. Streptavidin (SA) functionalized Fe-N_x SASCs were used to replace HRP in ELISA and detect Aβ1-40. The detection performance of the proposed Fe-N_x SASCs-linked immunosorbent assay (SASC-LISA) was examined and compared with commercial ELISA, results show that the SASC-LISA exhibited higher sensitivity, making Fe-N_x SASCs qualified as an HRP replacement and providing satisfactory feasibility in clinical diagnosis.

3.2 Experimental

3.2.1 Preparation of Fe-N_x SASCs

500mg of MO was dissolved in DI water, then 5 g of $FeCl_3$ and 1.5 mL pyrrole were added under vigorous stirring to form Fe^{3+} doped PPy nanotube. MnO_2 coated PPy nanotubes were prepared by dispersing a certain amount of $KMnO_4$ into the aforementioned solution. The product was pyrolyzed at 900°C under the nitrogen atmosphere, and the MnO_2 coating could be removed by leaching for 8 h with 5% H_2SO_4 (v/v). [30] Finally, the Fe-N_x SASCs was obtained after the second heat-treatment at 900°C under ammonia.

3.2.2 Fabrication of streptavidin labeled Fe-N_x SASCs

First of all, the tubed Fe-N_x SASCs were shattered under vigorous sonication and dispersed in PBS (0.5 mg/ml), then adjusted by K_2CO_3 to reach pH = 6.0 and ultrasonicated for 1h. Secondly, the solution was activated by EDC (2 mg/ mL) and NHS (4 mg/mL) under shaking for 30 minutes, and then centrifuged and washed three times to form the activated Fe-N_x SASCs. Streptavidin (SA, 100 μg/ml in PBS) was incubated with activated Fe-N_x SASCs at 37°C for 1 hour and the mixture was centrifuged for three times to remove unbonded SA. Lastly, the products were passivated with 1% BSA for 30 minutes and dispersed in 1 mL of PBS. Herein, the SA labeled Fe-N_x SASCs were broken down to nano size via an intense ultrasound treatment before further using in ELISA.

3.2.3 Detection of amyloid beta 1-40 by SASCs linked immunosorbent assay

Firstly, different amounts of amyloid beta 1-40 standard were added into a 96-well and incubated at 37°C for 2.5 h. Each well was washed for three times, and then 200 μL of PBST (PBS containing 0.5 wt % of TWEEN-20) containing 1 wt % BSA was added into it to block the unbonded primary antibody at 37 °C for 1.5 h. Secondly, 100 μL of the prepared biotinylated amyloid beta 1-40 was added to each well and incubated for 1h with gentle shaking, then the plate was washed with wash buffer for three times. Thirdly, 50 μL of SA labeled Fe-N_x SASCs was added into each well, and

shaken for 45 min. Finally, a chromogenic reaction was conducted. Specifically, 100 µL TMB was added to each well and the mixture was incubated for 10 min at room temperature under gentle shaking. Then 50 µL stop solution was added to stop the reaction and absorbance data were collected at 450 nm immediately upon color change.

3.3 Results and discussion

3.3.1 Materials characterizations

Figure 3.1 Schematic diagram of preparing SA-labeled Fe-N_x SASCs.

The synthesis route of SA labeled Fe-N_x SASCs is shown in **Figure 3.1**, in which $KMnO_4$ was added to form a layer of MnO_2 coated on the surface of PPy nanotubes to produce more single

atom active sites due to nanoconfinement effect. Specifically, MnO_2 coating can confine atoms into precursors, thus achieving high atomic distribution of Fe iron, reducing aggregation during pyrolysis, and greatly enhancing the number of $Fe-N_x$ active sites. Moreover, free migration of iron species could be restricted, further improving its catalytic performance. [31, 32]
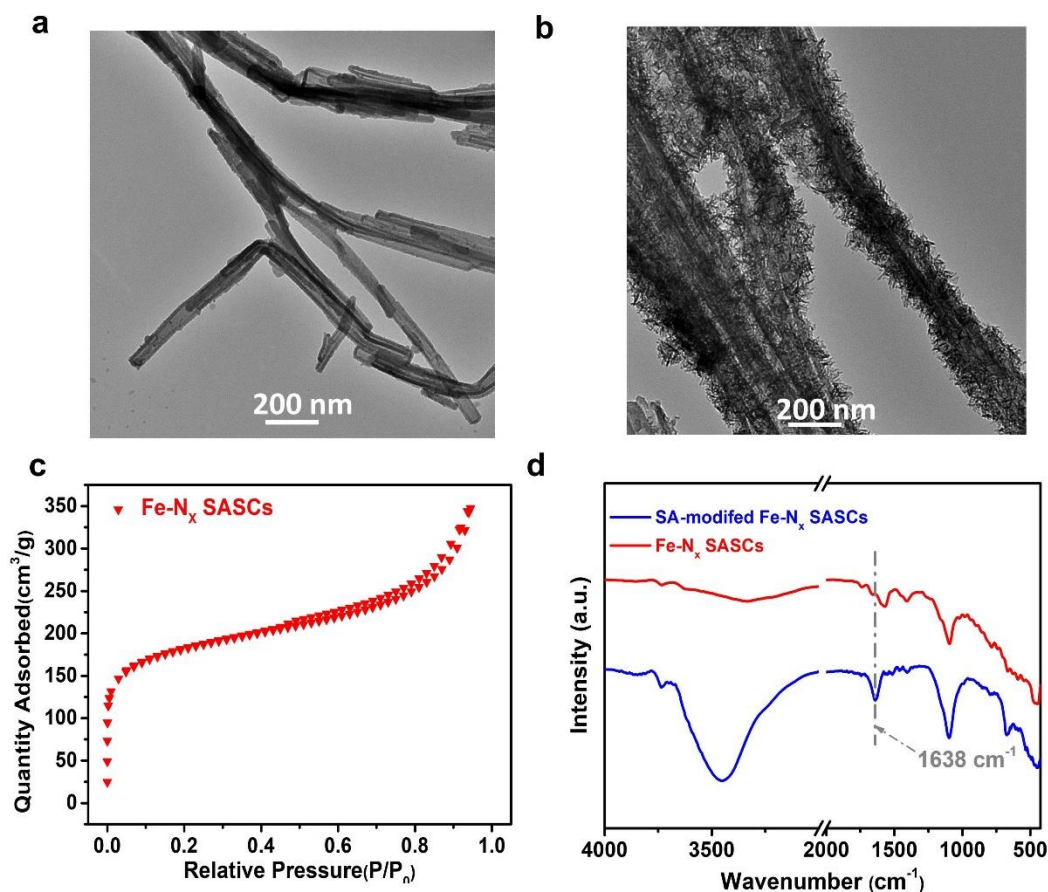
Figure 3.2 (a) and (b) Morphology of PPy nanotube and MnO_2 coated PPy nanotube, respectively. (c) N_2 adsorption-desorption isotherm of $Fe-N_x$ SASCs (d) Fourier transform infrared spectra of the $Fe-N_x$ SASCs and SA-labeled $Fe-N_x$ SASCs

The morphologies of PPy nanotube and MnO_2 coating PPy nanotube were confirmed by Transmission electron microscopy (TEM), shown in **Figure 3.2a** and **b**. N_2 adsorption/desorption test was carried out to evaluate detailed textural structure (**Figure 3.2c**). The Brunauer-Emmett-Teller (BET) surface areas of $Fe-N_x$ SASCs was 648.16 m²/g. The large surface area enabled the synthesized $Fe-N_x$ SASCs to host more $Fe-N_x$-C moieties, and thus achieving high peroxidase-like

activity. Next, the synthesized Fe-N$_x$ SASCs were treated with EDC and NHS, then modified with streptavidin (SA) to bind biotinylated Aβ 1-40 antibody, the strong peak at 1638 cm^{-1} which corresponds to the amide I show that streptavidin is already successful labeled on Fe-N$_x$ SASCs, which proved that the SA was successfully modified on Fe-N$_x$ SASCs (**Figure 3.2d**).[33] Thereinto, the biotin can react with SA conjugated labels, forming the strongest known noncovalent interaction between a protein and a ligand.[34]
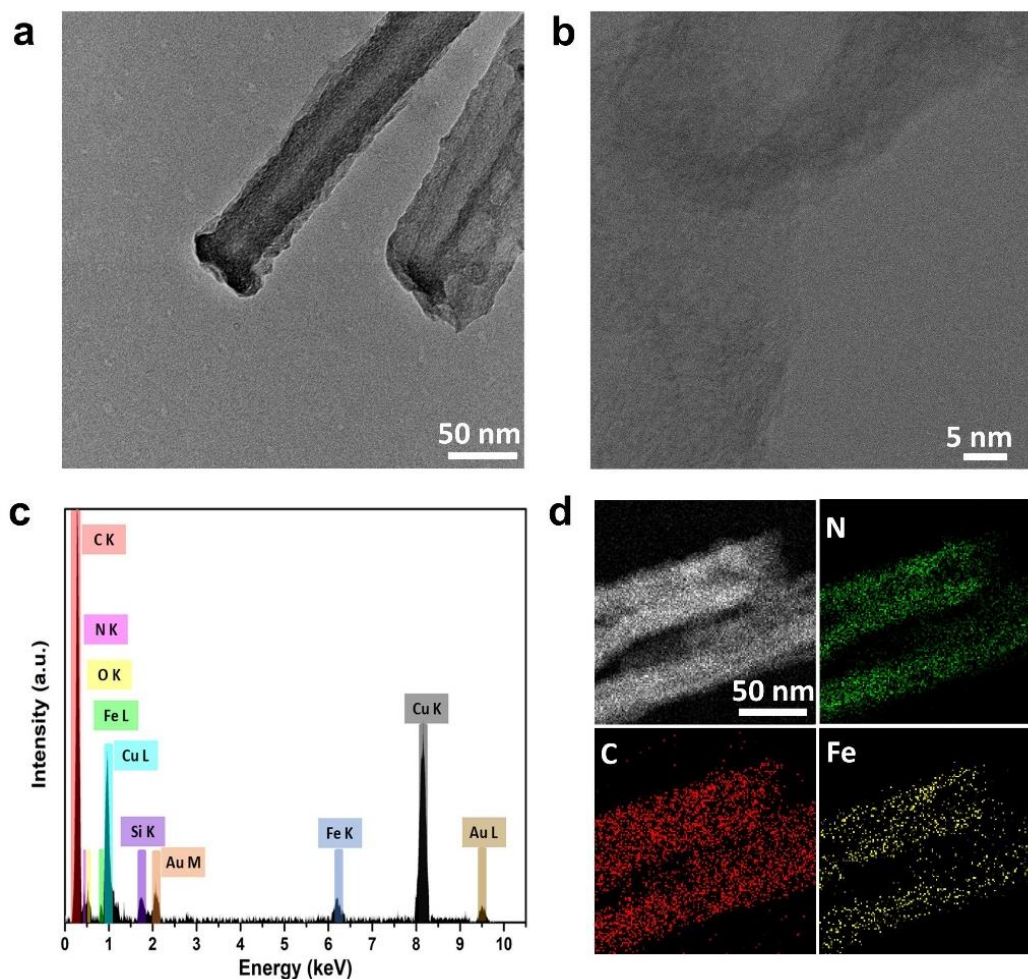
Figure 3.3 (a) TEM image of Fe-N$_x$ SASCs. (b) HRTEM image of the Fe-N$_x$ SASCs sample. (c) EDS elemental analysis of Fe-N$_x$ SASCs. (d) STEM image of Fe-N$_x$ SASCs and EDS elemental mapping results of C, N, and Fe.

In **Figure 3.3a**, the well-defined Fe-N$_x$ SASCs had a typical nanotube structure with a diameter of

around 50nm. Moreover, distorted graphite layers were found in Fe-N$_x$ SASCs (**Figure 3.3b**) by

high-resolution TEM (HRTEM). This graphite structure could provide enriched defects and nanopores, which would anchor abundant atomic Fe-N$_x$ moieties. Auxiliary energy-dispersive X-ray spectroscopy (EDS) elemental analysis demonstrated that the Fe-N$_x$ SASCs were comprised of C, N and Fe (**Figure 3.3c**). Here, the absence of Mn signal meant that the MnO$_2$ coating was removed successfully. Moreover, the EDS mapping of C, N and Fe was conducted, as shown in **Figure 3.3d**. All elements were distributed uniformly in the Fe-N$_x$ SASCs, indicating that the Fe-N$_x$ could be incorporated into the PPy matrix. Besides, no Fe clusters were observed, which was because the aggregated Fe species were washed out during acid treatment and the remaining Fe existed as isolated atoms.
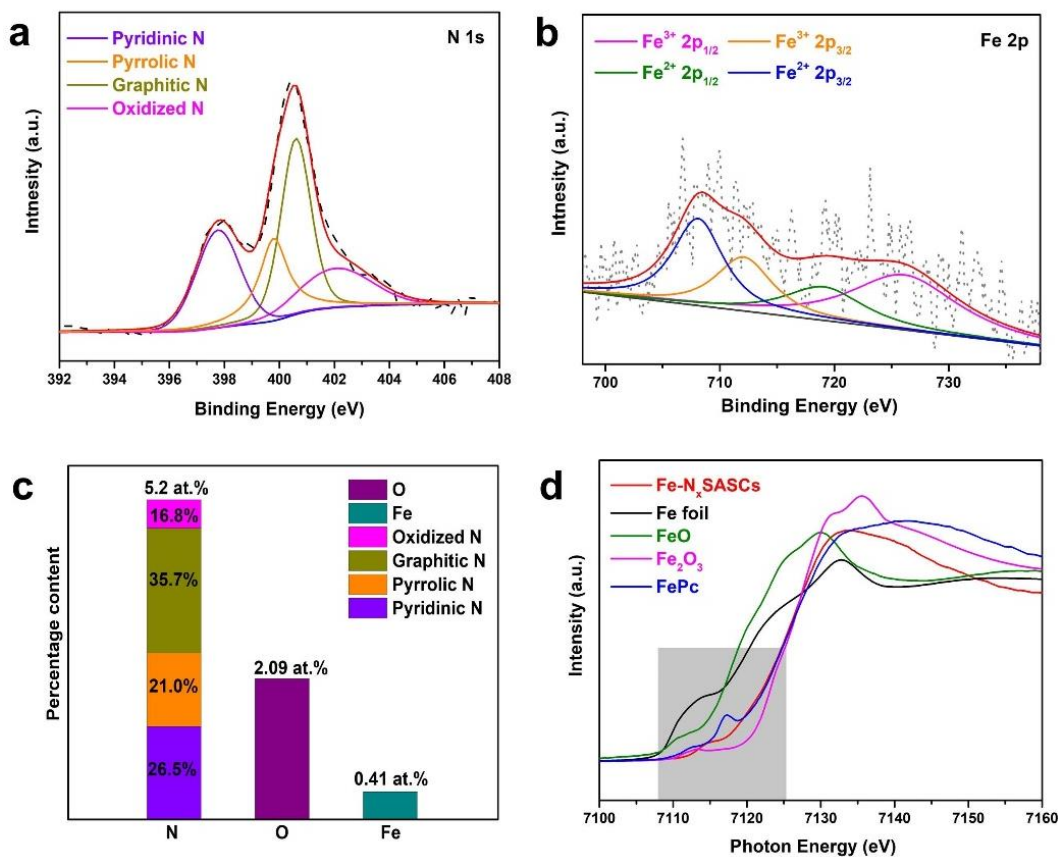
Figure 3.4 (a) and (b) High-resolution N 1s and Fe 2p spectra of Fe-N$_x$ SASCs, respectively. (c) N, O, and Fe contents in Fe-N$_x$ SASCs. (d) Fe K-edge XANES spectrum of Fe-N$_x$ SASCs and reference samples of FePc, Fe foil, FeO and Fe$_2$O$_3$.

In order to measure the chemical composition of Fe-N_x SASCs, high-resolution XPS spectra with curve fitting of N 1s and Fe 2p were adopted, and the results were shown in **Figure 3.4 a** and **b**. For N 1s, the spectrum of Fe-N_x SASCs could be fitted into four peaks at 397.7 eV, 399.7 eV, 400.7 eV and 402.1 eV, which corresponding to Fe-N_x or pyridinic N, pyrrolic N, graphitic N and oxidized N, respectively.[35] Here, we fitted the pyridinic N and Fe-N_x in one peak because of the small difference in binding energy between Fe-N_x and pyridinic N.[36] For Fe 2p, four peaks of 707.9 eV, 712.1 eV, 718.9 eV, 723.5 and 725.9 eV were assigned to Fe^{2+} $2p_{2/3}$, $Fe^{3+}2p_{2/3}$, $Fe^{2+}2p_{1/2}$ and $Fe^{3+}2p_{1/2}$ on the basis of binding energies, respectively.[37] The deconvolution method using Gaussian-Lorentz curve fittings was adopted to conduct the semiquantitative analysis of all the elements.[38, 39]

Figure 3.4c showed that the N and Fe contents were 5.02 at. % and 0.41 at.%, respectively, which correspond to previously published works of single-atomic Fe-N-C materials.[35, 40] The percentage of defective N configurations (pyridinic and pyrrolic N), regarded as coordination sites for single Fe atoms was high. Moreover, compared to traditional PPy nanotube-based Fe-N-C materials (0.35 at. % [35]), the nanoconfinement strategy enhanced Fe loading significantly.

The Fe K-edge X-ray absorption near-edge structure (XANES) spectra (**Figure 3.4d**) of Fe-N_x SASCs and reference samples of iron (II) phthalocyanine FePc, Fe foil, FeO and Fe_2O_3 were obtained. Obviously, the near-edge absorption energy of Fe-N_x SASCs located between standard bi-(FeO) and trivalent (Fe_2O_3) iron, illustrating that +2 and +3 coexisted in Fe-N_x SASCs, consistent with XPS results (**Figure 3.4b**).

Fourier-transform EXAFS curve of Fe-N_x SASCs in **Figure 3.5a** showed the Fe-N peak at 1.4 Å and no Fe-Fe peak at 2.1 Å was observed. Moreover, from the K-edge EXAFS oscillations, the spectrum of Fe-N_x SASCs was distinct from those of Fe foil and Fe oxides, but almost the same

as that of Fe single atom reference FePc (**Figure 3.5c**), which could further demonstrate that Fe was atomically dispersed in Fe-N$_x$ SASCs. Such a structure is also similar to natural HRP (**Figure 3.5d**), thereby possessing intrinsic peroxidase activity.
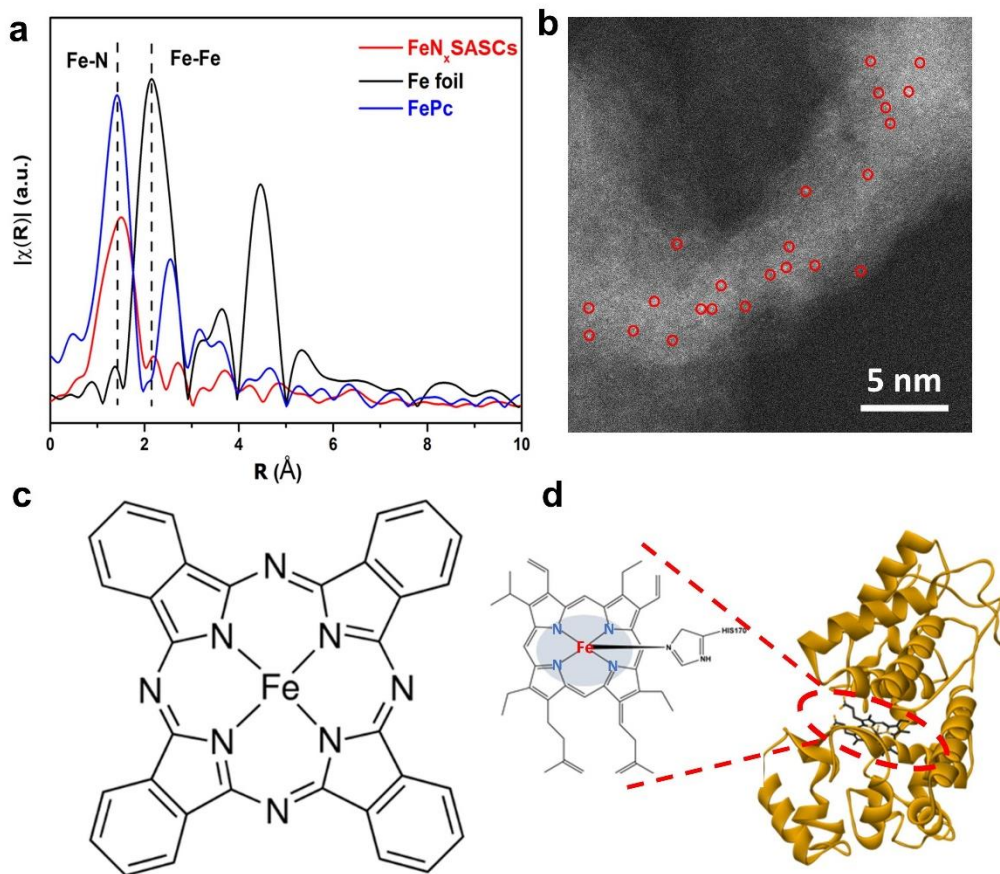
Figure 3.5 (a) FT k^3-weighted EXAFS spectrum of Fe-N$_x$ SASCs, FePc and Fe foil. (b) HAADF-STEM image of Fe-N$_x$ SASCs sample. (c-d) Structure of natural Iron (II) phthalocyanine (FePc) and HRP, respectively.

Subsequently, in order to confirm the distribution of Fe species in Fe-N$_x$ SASCs at atomic levels, aberration-corrected scanning TEM (STEM) characterizations were carried out (**Figure 3.5b**). It clearly showed that the Fe species were uniformly dispersed into the PPy matrix and formed single-atomic Fe sites, which were the bright dots circled with red marks. In addition, no nanoparticles were observed at the atomic level, which again proved that no aggregated Fe species existed in Fe-

N_x SASCs. All the results illustrated that enriched atomic Fe-N_x moieties had been doped in the PPy matrix effectively.

3.3.2 Peroxidase-like activities evaluation of Fe-N_x SASCs

TMB chromogenic reaction curve of absorbance to time was obtained and the sample without adding H_2O_2 was served as a reference. The result was shown in **Figure 3.6a**. The absorbance at 652nm increased with reaction time and the absorbance to reaction time was linear in the first minute with R^2 coefficient close to 1 in linear regression analysis.

The catalytic activity of Fe-N_x SASCs expressed in units (U) (**Figure 3.6b**) was further assessed. The peroxidase-mimic activity of the Fe-N_x SASCs was calculated to be 64.79 U mg^{-1}, further proved that the synthesized SASCs possessed unprecedented peroxidase-like properties. This is due to that those active sites of Fe-N_x have similar effective structures to natural enzymes. What's more, owing to single atom Fe, the atom utilization could become 100% theoretically. In other words, every single atom can work as an active site to catalyze H_2O_2. Kinetics of peroxidase-mimicking catalysis of Fe-N_x SASCs was analyzed, as shown in **Figure 3.6c** and **d**.

Also, the stability of Fe-N_x SASCs in harsh environments was evaluated (**Figure 3.6e** and **f**). The curve demonstrated that the SASCs maintained excellent stability with pH and temperature variation, while HRP gradually lost its activities when pH was higher than four or the temperature was not close to 40°C.
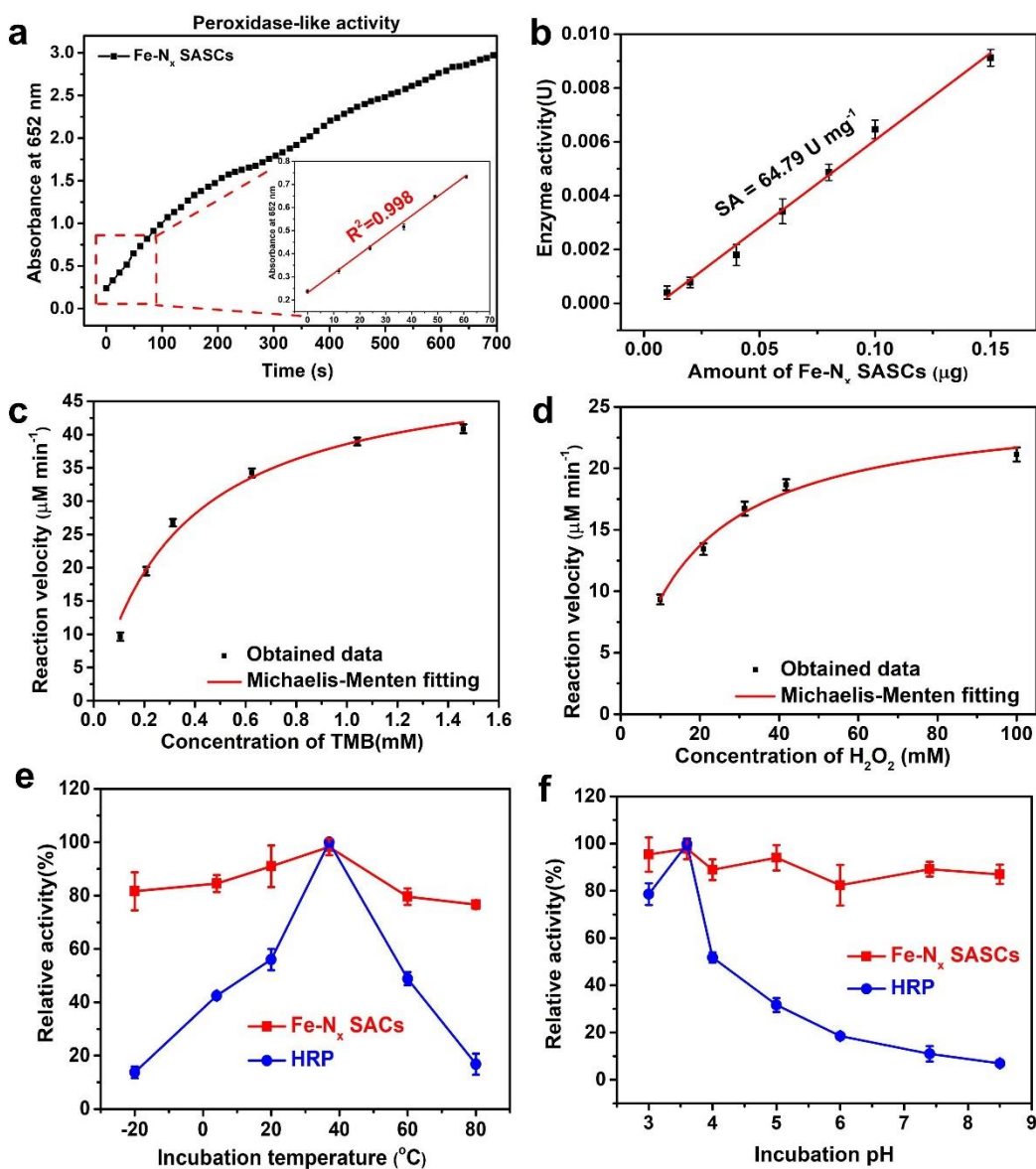
Figure 3.6 (a) Absorbance-time curve of TMB chromogenic reaction catalyzed by Fe-N_x SASCs and the corresponding magnified initial linear portion. (b) Specific activities of Fe-N_x SASCs. (c) and (d) Steady-state kinetics curves of Fe-N_x SASCs toward TMB and H_2O_2, respectively. (e) and (f) Robustness of Fe-N_x SASCs against the harsh environment of temperature and pH, respectively.

The Steady-state kinetics curves of Fe-N_x SASCs towards TMB substrates and H_2O_2 were obtained and listed in Table 3.1. Michaelis constants (K_m) of the steady-state kinetics were obtained by fitting in the Michaelis-Menten model and compared with that of HRP. The K_m of Fe-N_x SASCs

with TMB and H_2O_2 as the substrate is slightly lower than that of HRP, demonstrating that the SASCs has a comparable affinity of HRP.

Table 3.1 steady-state kinetics parameters of Fe-N_x SASCs and natural HRP

Materials	[E] (M)	Substrate	K_m (mM)	v_{max} (μM min^{-1})	K_{cat} (min^{-1})	K_{cat}/K_m (M^{-1} min^{-1})
Fe-N_x SASCs	7.3×10^{-11}	H_2O_2	17.12	24.48	3.35×10^5	19.57×10^6
		TMB	0.3322	51.4	7.04×10^5	21.19×10^8
Natural HRP	2.5×10^{-11}	H_2O_2	18.64	48.6	1.99×10^6	10.6×10^7
		TMB	0.4269	55.49	2.22×10^6	5.2×10^9

3.3.3 Detection performance of SASCs-linked immunosorbent assay

Amyloid beta 1-40 is a typical biomarker of detecting Alzheimer's Disease (AD). However, the concentration of Aβ 1-40 is in pg/mL to ng/mL level in human serum which requires sensitive and accurate detection in the early diagnosis of Alzheimer's disease. Herein, a typical sandwich-type SASCs-linked immunosorbent assay (SASC-LISA) was built to detect Aβ 1-40, shown in **Figure 3.7**.
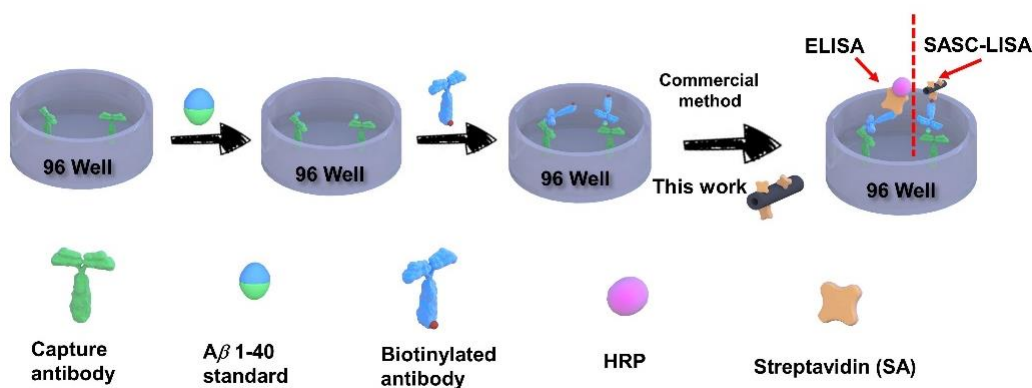
Figure 3.7 Schematic illustration of SASC-LISA for the detection of Aβ 1-40.

The curve of SASCs detecting Aβ 1-40 was obtained and was shown in **Figure 3.8a**. The linear range was 1 pg/mL to 2000 pg/mL. The low concertation range between 0-15 pg/ml was shown in inserted figure of **Figure 3.8a**, by applying to the equation 3S/K, where S and K referred to the standard deviation of blank sample and slope of the standard curve respectively, the limit of detection (LOD) was calculated to be 0.88 pg/mL, which is low enough to meet the detection requirement of human serum.
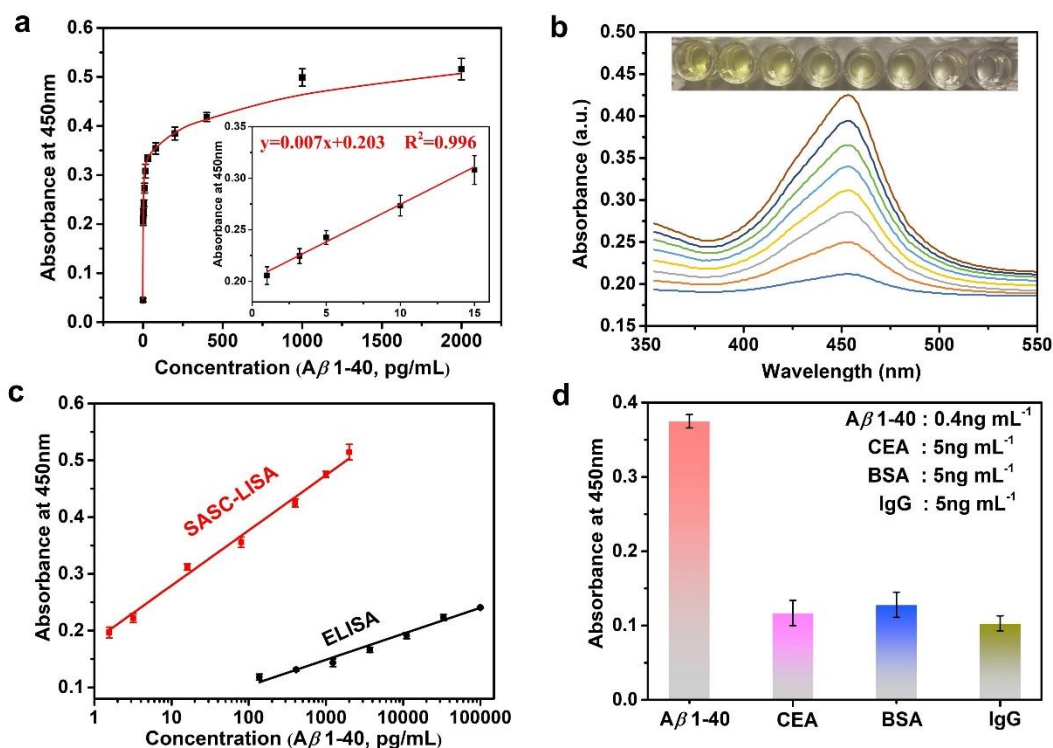
Figure 3.8 (a) The curve of SASC-LISA for the detection of Aβ 1-40 ranging from 1 pg/mL to 2000 pg/mL. The inserted figure showed a low concentration of 0-15 pg/ml (b) Absorbance spectra of various concentrations of Aβ 1-40 detected by SASC-LISA. (c) Standard curves of SASC-LISA (Aβ 1-40 ranging from 1 to 2000 pg/mL) and ELISA (Aβ 1-40 ranging from 100 pg/mL to 100 ng/mL). (d) Specificity of SASC-LISA (Aβ 1-40 of 400 pg/mL; CEA, BSA and IgG of 5 ng/mL, respectively).

Absorbance spectra of various concentrations of Aβ 1-40 detected by SASC-LISA and their corresponding colorimetric signal were shown in **Figure 3.8b**. It shown clearly that the signal intensities increased with elevated concentrations of Aβ 1-40. By applying the previous equation,

the LOD of the traditional ELISA was calculated to be 9.98 pg/mL, which was almost 11 times higher than that of SASC-LISA. The enhanced sensitivity was due to the ultrahigh surface area which could hold more active sites.

Furthermore, we evaluated the sensitivity of SASC-LISA by comparing the signal between traditional ELISA and proposed SASC-LISA. (**Figure 3.8c**). The results proved that SASC-LISA has better sensitivity, with much higher absorbance on much lower concertation of $A\beta$ 1-40. Lastly, the specificity of SASC-LISA was analyzed, as displayed in **Figure 3.8d**. $A\beta$ 1-40 exhibited a distinct signal, while the other competition protein had negligible signals, indicating the satisfactory specificity of SASC-LISA.

As shown in **Table 3.2**, compared with previously reported detection results of $A\beta$ 1-40 using different methods, the proposed SANs-LISA method exhibits superior detection performance.

Table 3.2 Reviews of the detection of $A\beta$ 1-40 with different methods

Techniques	LOD (pg mL^{-1})	Linear Range (pg mL^{-1})	Reference
SASC-LISA	0.88	1-2000	This work
Electrochemical Immunoassay	19	20-12500	[1]
SWV* at GCE*	7×10^5 [##]	nonlinear	[41]
Microfluidic Droplet	2165 [#]	NP	[42]
EIS*	2468 [#]	43.3-4.33×10^5 [#]	[43]
SPR*	14.3 [###]	86.6-865.9 [#]	[44]
SWV*	8.6×10^5 [#]	1.772×10^6-8.66×10^6 [#]	[45]

SWV: Square Wave Voltammetry**;** GCE: Glassy Carbon Electrode; SPR: Surface Plasmon Resonance; ECL: Electrochemiluminescence (ECL) immunosensor; EIS: Electrochemical Impedance Spectroscopy
#: Value was expressed in nM and converted to pg mL^{-1}; ##: Value was expressed in ug mL^{-1} and converted to pg mL^{-1}; ###: Value was expressed in pM and converted to pg mL^{-1}

3.4 Conclusion

In summary, we have successfully synthesized a Fe-N$_x$ single-atomic site catalyst with outstanding peroxidase-mimicking activity, which is mainly attributed to the ultra-large surface area of carbon support that forms more active sites and enables 100% Fe atom utilization. It also shows excellent robustness in harsh environments. Most importantly, novel Fe-N$_x$ SASC-LISA is built to enhance the detection performance of Aβ1-40, exhibiting a sensitivity with LOD of 0.88 pg/mL. This result is much lower than that of the commercial ELISA kit (9.98 pg/mL), which meets the requirement of effective detection of Aβ1-40. Based on the high activity of Fe-N$_x$ SASCs and improved ELISA performance, the peroxidase-like SASCs show great potential and pave a new way to design novel ELISA kit with improved sensitivity for detecting various target biomarkers.

REFERENCES

1. A. de la Escosura-Muñiz, Z. Plichta, D. Horák, A. Merkoçi, Alzheimer′s disease biomarkers detection in human samples by efficient capturing through porous magnetic microspheres and labelling with electrocatalytic gold nanoparticles, Biosensors and Bioelectronics, 67 (2015) 162-169.

2. A. Nakamura, N. Kaneko, V.L. Villemagne, T. Kato, J. Doecke, V. Doré, C. Fowler, Q.-X. Li, R. Martins, C. Rowe, High performance plasma amyloid-β biomarkers for Alzheimer's disease, Nature, 554 (2018) 249.

3. A.s. Association, 2019 Alzheimer's disease facts and figures, Alzheimer's & Dementia, 15 (2019) 321-387.

4. H. Kim, J.U. Lee, S. Song, S. Kim, S.J. Sim, A shape-code nanoplasmonic biosensor for multiplex detection of Alzheimer's disease biomarkers, Biosensors and Bioelectronics, 101 (2018) 96-102.

5. F. Qu, M. Yang, A. Rasooly, Dual signal amplification electrochemical biosensor for monitoring the activity and inhibition of the Alzheimer's related protease β-secretase, Analytical Chemistry, 88 (2016) 10559-10565.

6. G. Zhao, Y. Wang, X. Li, Q. Yue, X. Dong, B. Du, W. Cao, Q. Wei, Dual-quenching electrochemiluminescence strategy based on three-dimensional metal-organic frameworks for ultrasensitive detection of amyloid-β, Analytical Chemistry, 91 (2019) 1989-1996.

7. A. Vázquez de la Torre, M. Gay, S. Vilaprinyó-Pascual, R. Mazzucato, M. Serra-Batiste, M. Vilaseca, N.l. Carulla, Direct evidence of the presence of cross-linked Aβ dimers in the brains of Alzheimer's disease patients, Analytical Chemistry, 90 (2018) 4552-4560.

8. X. Li, X. Yang, J. Zhang, Y. Huang, B. Liu, In Situ/Operando Techniques for Characterization of Single-Atom Catalysts, ACS Catalysis, 9 (2019) 2521-2531.

9. N.J. Abbott, Astrocyte-endothelial interactions and blood–brain barrier permeability, Journal of Anatomy, 200 (2002) 629-638.

10. J.P. Cleary, D.M. Walsh, J.J. Hofmeister, G.M. Shankar, M.A. Kuskowski, D.J. Selkoe, K.H. Ashe, Natural oligomers of the amyloid-β protein specifically disrupt cognitive function, Nature Neuroscience, 8 (2005) 79-84.

11. H.-N. Chan, D. Xu, S.-L. Ho, D. He, M.S. Wong, H.-W. Li, Highly sensitive quantification of Alzheimer's disease biomarkers by aptamer-assisted amplification, Theranostics, 9 (2019) 2939.

12. G. Chételat, Alzheimer disease: Aβ-independent processes-rethinking preclinical AD, Nature Reviews. Neurology, 9 (2013) 123.

13. E.C. Rama, M.B. González-García, A. Costa-García, Competitive electrochemical immunosensor for amyloid-beta 1-42 detection based on gold nanostructurated Screen-Printed Carbon Electrodes, Sensors Actuators B: Chemical, 201 (2014) 567-571.

14. Y. Yu, X. Sun, D. Tang, C. Li, L. Zhang, D. Nie, X. Yin, G. Shi, Gelsolin bound β-amyloid peptides (1-40/1-42): Electrochemical evaluation of levels of soluble peptide associated with Alzheimer's disease, Biosensors Bioelectronics, 68 (2015) 115-121.

15. S. Ding, Z. Lyu, X. Niu, Y. Zhou, D. Liu, M. Falahati, D. Du, Y. Lin, Integrating ionic liquids with molecular imprinting technology for biorecognition and biosensing: A review, Biosensors and Bioelectronics, 149 (2020) 111830.

16. K. Petropoulos, S.F. Bodini, L. Fabiani, L. Micheli, A. Porchetta, S. Piermarini, G. Volpe, F.M. Pasquazzi, L. Sanfilippo, P. Moscetta, Re-modeling ELISA kits embedded in an automated system

suitable for on-line detection of algal toxins in seawater, Sensors Actuators B: Chemical, 283 (2019) 865-872.

17. L. Jiao, L. Zhang, W. Du, H. Li, D. Yang, C. Zhu, Hierarchical manganese dioxide nanoflowers enable accurate ratiometric fluorescence enzyme-linked immunosorbent assay, Nanoscale, 10 (2018) 21893-21897.

18. C. Li, Y. Yang, D. Wu, T. Li, Y. Yin, G. Li, Improvement of enzyme-linked immunosorbent assay for the multicolor detection of biomarkers, Chemical Science, 7 (2016) 3011-3016.

19. K. Chattopadhyay, S. Mazumdar, Structural and conformational stability of horseradish peroxidase: effect of temperature and pH, Biochemistry, 39 (2000) 263-270.

20. H. Wei, E. Wang, Nanomaterials with enzyme-like characteristics (nanozymes): next-generation artificial enzymes, Chemical Society Reviews, 42 (2013) 6060-6093.

21. N. Cheng, Q. Shi, C. Zhu, S. Li, Y. Lin, D. Du, Pt-Ni (OH)$_2$ nanosheets amplified two-way lateral flow immunoassays with smartphone readout for quantification of pesticides, Biosensors and Bioelectronics, 142 (2019) 111498.

22. J. Wu, X. Wang, Q. Wang, Z. Lou, S. Li, Y. Zhu, L. Qin, H. Wei, Nanomaterials with enzyme-like characteristics (nanozymes): next-generation artificial enzymes (II), Chemical Society Reviews, 48 (2019) 1004-1076.

23. Y. Wu, L. Jiao, X. Luo, W. Xu, X. Wei, H. Wang, H. Yan, W. Gu, B.Z. Xu, D. Du, Oxidase-Like Fe-N-C Single-Atom Nanozymes for the Detection of Acetylcholinesterase Activity, Small, 15 (2019) 1903108.

24. Y. Luo, Y. Song, M. Wang, T. Jian, S. Ding, P. Mu, Z. Liao, Q. Shi, X. Cai, H. Jin, Bioinspired Peptoid Nanotubes for Targeted Tumor Cell Imaging and Chemo-Photodynamic Therapy, Small, 15 (2019) 1902485.

25. J.-C. Li, F. Xiao, H. Zhong, T. Li, M. Xu, L. Ma, M. Cheng, D. Liu, S. Feng, Q. Shi, Secondary-atom-assisted synthesis of single iron atoms anchored on N-doped carbon nanowires for oxygen reduction reaction, ACS Catalysis, 9 (2019) 5929-5934.

26. X. Niu, N. Cheng, X. Ruan, D. Du, Y. Lin, Nanozyme-Based Immunosensors and Immunoassays: Recent Developments and Future Trends, Journal of the Electrochemical Society, 167 (2019) 037508.

27. X. Niu, Q. Shi, W. Zhu, D. Liu, H. Tian, S. Fu, N. Cheng, S. Li, J.N. Smith, D. Du, Unprecedented peroxidase-mimicking activity of single-atom nanozyme with atomically dispersed Fe–Nx moieties hosted by MOF derived porous carbon, Biosensors and Bioelectronics, 142 (2019) 111495.

28. N. Cheng, J.C. Li, D. Liu, Y. Lin, D. Du, Single-Atom Nanozyme Based on Nanoengineered Fe-N-C Catalyst with Superior Peroxidase-Like Activity for Ultrasensitive Bioassays, Small, 15 (2019) 1901485.

29. L. Jiao, H. Yan, Y. Wu, W. Gu, C. Zhu, D. Du, Y. Lin, When nanozymes meet single-atom catalysis, Angewandte Chemie, 132 (2020) 2585-2596.

30. D. Hariprasad, B. Dash, M. Ghosh, S. Anand, Leaching of manganese ores using sawdust as a reductant, Minerals Engineering, 20 (2007) 1293-1295.

31. T.A. Shifa, A. Vomiero, Confined catalysis: progress and prospects in energy conversion, Advanced Energy Materials, 9 (2019) 1902307.

32. J. Guo, Y. Li, Y. Cheng, L. Dai, Z. Xiang, Highly efficient oxygen reduction reaction electrocatalysts synthesized under nanospace confinement of metal-organic framework, ACS Nano, 11 (2017) 8379-8386.

33. Z. Liu, L. Jiang, F. Galli, I. Nederlof, R.C. Olsthoorn, G.E. Lamers, T.H. Oosterkamp, J.P. Abrahams, A graphene oxide streptavidin complex for biorecognition-towards affinity purification, Advanced Functional Materials, 20 (2010) 2857-2865.

34. D. Xu, S.V. Wegner, Multifunctional streptavidin-biotin conjugates with precise stoichiometries, Chemical Science, 11 (2020) 4422-4429.

35. D. Liu, J.-C. Li, Q. Shi, S. Feng, Z. Lyu, S. Ding, L. Hao, Q. Zhang, C. Wang, M. Xu, Atomically isolated iron atom anchored on carbon nanotubes for oxygen reduction reaction, ACS Applied Materials & Interfaces, 11 (2019) 39820-39826.

36. H.-W. Liang, W. Wei, Z.-S. Wu, X. Feng, K. Mullen, Mesoporous metal-nitrogen-doped carbon electrocatalysts for highly efficient oxygen reduction reaction, Journal of the American Chemical Society, 135 (2013) 16002-16005.

37. J.-C. Li, M. Cheng, T. Li, L. Ma, X. Ruan, D. Liu, H.-M. Cheng, C. Liu, D. Du, Z. Wei, Carbon nanotube-linked hollow carbon nanospheres doped with iron and nitrogen as single-atom catalysts for the oxygen reduction reaction in acidic solutions, Journal of Materials Chemistry A, 7 (2019) 14478-14482.

38. M. Seah, M. Brown, Validation and accuracy of peak synthesis software for XPS, Applied Surface Science, 144 (1999) 183-187.

39. S. Ding, X. Hu, P. Guan, N. Zhang, J. Li, X. Gao, X. Zhang, X. Ding, C. Du, Preparation of surface-imprinted microspheres using ionic liquids as novel cross-linker for recognizing an immunostimulating peptide, Journal of Materials Science, 52 (2017) 8027-8040.

40. J.-C. Li, Z.-Q. Yang, D.-M. Tang, L. Zhang, P.-X. Hou, S.-Y. Zhao, C. Liu, M. Cheng, G.-X. Li, F. Zhang, N-doped carbon nanotubes containing a high concentration of single iron atoms for efficient oxygen reduction, NPG Asia Materials, 10 (2018) e461-e461.

41. M.d. Vestergaard, K. Kerman, M. Saito, N. Nagatani, Y. Takamura, E. Tamiya, A rapid label-free electrochemical detection and kinetic study of Alzheimer's amyloid beta aggregation, Journal of the American Chemical Society, 127 (2005) 11892-11893.

42. T.D. Mai, D. Ferraro, N. Aboud, R. Renault, M. Serra, N.T. Tran, J.-L. Viovy, C. Smadja, S. Descroix, M. Taverna, Single-step immunoassays and microfluidic droplet operation: towards a versatile approach for detection of amyloid-β peptide-based biomarkers of Alzheimer's disease, Sensors and Actuators B: Chemical, 255 (2018) 2126-2135.

43. T.T. Lien, Y. Takamura, E. Tamiya, C.V. Mun'delanji, Modified screen printed electrode for development of a highly sensitive label-free impedimetric immunosensor to detect amyloid beta peptides, Analytica Chimica Acta, 892 (2015) 69-76.

44. N. Xia, L. Liu, M.G. Harrington, J. Wang, F. Zhou, Regenerable and simultaneous surface plasmon resonance detection of aβ (1-40) and aβ (1-42) peptides in cerebrospinal fluids with signal amplification by streptavidin conjugated to an n-terminus-specific antibody, Analytical Chemistry, 82 (2010) 10151-10157.

45. S. Prabhulkar, R. Piatyszek, J.R. Cirrito, Z.Z. Wu, C.Z. Li, Microbiosensor for Alzheimer's disease diagnostics: detection of amyloid beta biomarkers, Journal of Neurochemistry, 122 (2012) 374-381.

CHAPTER FOUR: TWO-DIMENSIONAL Fe-N-C SINGLE ATOMIC-SITE CATALYSTS

WITH BOOSTED PEROXIDASE-LIKE ACTIVITY FOR SENSITIVE IMMUNOASSAY

4.1 Introduction

The broad usage and high consumption of herbicide have resulted in herbicide accumulation in the soil, air, ocean, food, water sources, and even in the human body, severely impacting the ecosystem and food safety.[1] Nowadays, researchers have found that exposure to herbicide can be associated with serious health problems such as endocrine-disrupting activities,[2] acute congestion and degenerative changes in the central nervous system.[3]. 2,4-Dichlorophenoxyacetic acid (2,4-D), a common and important phenoxy herbicide, was the first successful one ever developed since its commercial release in the 1940s.[4] It is considered as one of the "probably carcinogenic compounds to humans".[5, 6] Since 2,4-D remains chemically stable in the human body and can be secreted through urine,[7] direct detection of 2,4-D concentration in human urine is a meaningful and effective way to judge a person's exposure level. For example, for non-exposed adults and children in the USA and Canada, 2,4-D concentrations in urine samples are less than 3.5 ng/mL,[8, 9] while for the workers who are occupationally exposed to herbicides, the average 2,4-D concentrations of 7.8 and 33 ng/mL were detected in urine before and after 2,4-D spray, respectively.[10, 11] Up to now, the quantification of 2,4-D and other herbicides is usually based on its inhibitory effect on alkaline phosphatase (ALP) activity via electrochemical workstations or various chromatographic techniques.[12, 13] However, these methods suffer from poor reproducibility, expensive equipment, meticulous sample preparation, and highly qualified technicians, which limit their fast point-of-care (POC) applications.[13] Hence, developing effective methods for simple, rapid, cost-effective, and sensitive detection of 2,4-D becomes an important goal.

As a recognized standard, enzyme-linked immunosorbent assay (ELISA) has been widely used in food safety, clinical testing, environmental assessment, and other fields. It has the attractive advantage of fast detection, simple operation, and strong applicability. The mechanism of ELISA is that the interaction of antigen and antibody can be converted into visible color change, which is convenient for observation and detection. In which competitive ELISA is widely used in small-molecule detection, such as residues (pesticides, antibiotics), environmental contaminants (heavy metals, mycotoxins), unapproved adulterants (food colorants), and process contaminants acrylamide, heterocyclic amines)[14, 15] In competitive immunoreaction, the principle is based on the competitive binding of the primary antibody between the target antigen in the sample and the same antigen coated on the plate. However, the detection performance of traditional ELISA is highly dependent on the activity of peroxidase (HRP). According to previous studies, the enzymatic activity of HRP is affected by detecting pH and temperature.[16-18] Thus, in practical applications, the limitations of high enzyme cost, detection dependence, long incubation time, and moderate sensitivity need to be addressed.

Compared to traditional ELISA using natural HRP, applying nanomaterials with POD-like activity in ELISA is a promising method to address the challenges. Numerous studies have demonstrated that improved ELISA has been constructed based on the introduction of novel nanomaterials, resulting in significantly improved detection sensitivity and ease of operation. Many other types of nanomaterials like magnetic Fe_3O_4 nanomaterials[19, 20] and Au nanoparticles[21] have been utilized as carriers to enhance the sensitivity of ELISAs. But the used nanomaterials suffered from the low POD-like activity, so ways to increase the intrinsic activity of the used materials have been regarded as a problem that needs to be addressed.

Two-dimensional (2D) nanomaterials, as sheet-like structured nanomaterials, have received significant attention for their large surface, anisotropic chemical/physical properties, biocompatibility, and degradability.[22, 23] Researchers have used 2-dimensional nanomaterials and their derivatives in biological applications of bioimaging, biosensors, bioengineering, and drug delivery.[24-26] Regulating the size of nanomaterials, especially downsizing nanomaterials to single atoms, has been regarded as a potential way to address this challenge. Single-atomic site nanomaterials have attracted widespread attention as hot research fields due to their unique electronic/geometric structure containing massive isolated active metal sites. In the previous chapters, we have synthesized different kinds of Fe-N-C SASCs, but it is still hard to own the comparable activity with HRP. In this chapter, we have used iron (II) phthalocyanine (FePc) in preparing precursors, in this way, the Fe-N structure has been induced into our SASCs. Then, we have used the 2D graphene as carbon support to synthesize the SASCs, we believe the 2D structure can help to expose more active sites and better boost the catalytic activity, thus achieving sensitive detection of 2,4-Dichlorophenoxyacetic acid (2,4-D) by using 2D Fe-SASCs in the competitive ELISA (2D Fe-SASC-LISA).

4.2 Experimental

4.2.1 Preparation of 2D Fe-SASC

A typical Hummer's method was used to prepare Graphene oxide (GO). Specifically, solution A was prepared by dissolving 1.8 g Zn (NO$_3$)$_2$ • 6H$_2$O and 25 mg of iron (II) phthalocyanine (FePc) into 100 mL methanol. Solution B was prepared by dissolving 2-Methylimidazole into 40 mL of methanol. Solution C was 160 mL 0.5 mg mL^{-1} graphene oxide methanol solution. Then string the mixture of a solution of A and B to get FePc/ZIF-8 and 30 min later, add solution C to the mixture above. The precursor of FePc/ZIF-8/GO was collected 8h later by centrifugation, washed with

deionized water and ethanol, then freeze-dried. 2D Fe- SASCs were synthesized through pyrolyzing under N_2 flow for 30 min and NH_3 flow for another 30 min at 900 °C, then acidic washing using 0.5M H_2SO_4 at 80 °C for 6 h.

4.2.2 Fabrication of 2D Fe-SASC labeled 2,4-D secondary antibody

2D Fe-SASCs were dispersed in PBS (0.5 mg/ml) and adjusted by K_2CO_3 to reach pH equals to 6.0, activating by EDC (2 mg/ mL) and NHS (4 mg/mL) under shaking for 30 minutes. Then centrifuged and washed three times to remove the extra EDC and NHS. 2,4-D secondary antibody. (100 µg/ml in PBS) was incubated with activated 2D Fe-SASCs at 37°C for 1 hour, and the mixture was centrifuged and washed to remove unbonded 2,4-D secondary antibody. The final product was gotten through passivating with 1% BSA for 30 minutes and dispersed in 1 mL of PBS.

4.2.3 Establishment of competitive 2D Fe-SASC-LISA

Firstly, 2,4-D hapten was diluted 4000 times with PBS and added 100 µL into a 96-well microtiter plate, then sealing the plate with cover and incubating at 4°C overnight. Each well was washed three times to remove the uncoated hapten. Adding 250 µL of blocking solution of 3% BSA+0.05% Tween and incubating at 4°C overnight to block the nonspecific sites, then washed three times with PBS. Secondly, prepare a concentration range of 2,4-D standards (0.01-500 ng/mL), adding 100 µL of the diluted 2,4-D primary antibody (×10000) and 100 µL of prepared 2,4-D with different concentrations into each well, then incubated for 2 h with gentle shaking at room temperature followed by three times washing with PBS.

Thirdly, dilute the secondary antibody of goat anti-mouse IgG to 1:10000 and add 50 µL into each well, seal the plates, incubate at room temperature for another 90 min with continuous shaking, and wash with PBS for 4 times. Lastly, adding 50 µL of TMB into the wells and incubating at

room temperature under dark environment for 30 min, then adding 50 µL stop solution of 0.5M H_2SO_4 to each well and absorbance data were collected at 450 nm immediately upon color change to yellow.

4.3 Results and discussion

4.3.1 Materials characteristics

Figure 4.1 illustrates the preparation process of material synthesis and the detection principle of the competitive immunoassay. The 2D Fe-SASC was synthesized via a ZIF-8 "thermal melting" method. [27, 28]
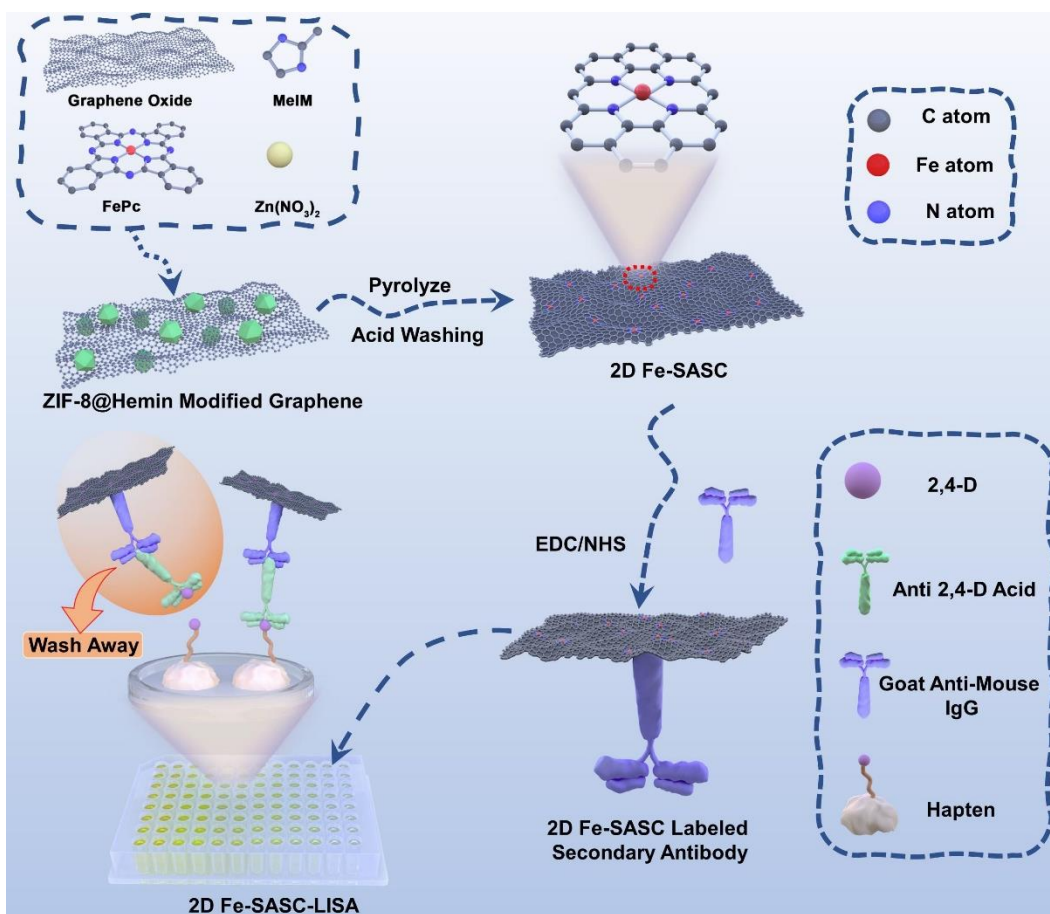
Figure 4.1 Schematic diagram of 2D Fe-SASC synthesis and colorimetric detection of 2,4-Dichlorophenoxyacetic acid (2,4-D)

Firstly, iron (II) phthalocyanine (FePc)-doped ZIF-8 (ZIF-8@FePc) growing on GO surface was prepared and used as a precursor. Herein, the 2D GO nanosheets can firmly host the ZIF-8@FePc due to the interactions between the metal ions in ZIF-8 and the functional groups on GO.[27] Then, 2D Fe-SASC was obtained by pyrolyzing under high temperature and acid washing. Next, the synthesized 2D Fe-SASC was activated with N-(3-dimethylamino propyl)-N′-ethylcarbodiimide hydrochloride (EDC) and N-hydroxysuccinimide (NHS), then bonded with 2,4-D primary antibodies. The 2D Fe-SASC labeled primary antibody was applied in the competitive immunoassay. Hence, the more antigen in the sample, the less antibody is available to bind to the antigen in the wells, resulting in a signal reduction. Therefore, we utilized this peroxidase-like 2D Fe-SASC to develop a new 2D Fe-SASC-LISA for enhancing the detection performance of 2,4-D. Transmission electron microscopy (TEM) image of the precursor is shown in **Figure 4.2a**. It is shown that ZIF-8@FePc with a rhombic dodecahedral structure is anchored on the GO nanosheets. The structure of 2D Fe-SASC is shown in **Figure 4.2b**, and it can be seen that it had a wrinkled nanosheet structure. Here, the ZIF-8@FePc was disappeared through a thermal melting step.

The STEM image in **Figure 4.2c** further proven the obtained SASC has the typical 2D structure. High-angle annular dark-field STEM (HAADF-STEM) was further employed to investigate the Fe configurations in 2D Fe-SASC at the atomic level. As shown in **Figure 4.2d**, the large amounts of bright dots represent isolated iron atoms in 2D Fe-SASC. Such abundant single Fe atom sites in the synthesized Fe-SASC endow it with outstanding peroxidase-like activity. Combining with energy-dispersive X-ray spectroscopy (EDS) analysis, we achieved the elemental composition and distribution in 2D Fe-SASC. As shown in **Figure 4.2e**, the uniformly distributed C, N, O, and Fe signals were detected, suggesting that Fe and N were successfully doped in 2D Fe-SASC.
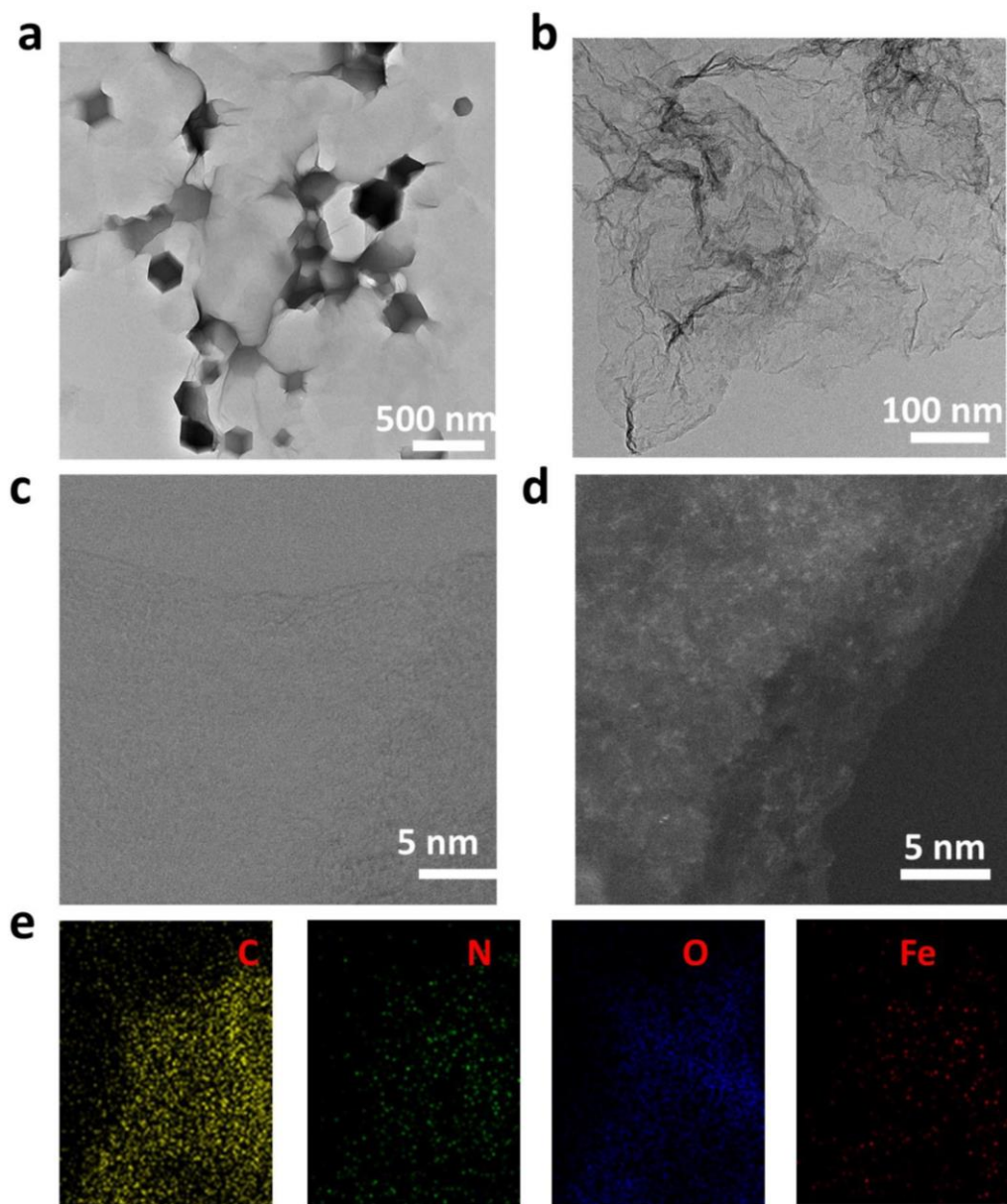
Figure 4.2 (a) TEM image of the ZIF-8@FePc modified GO. (b-d) TEM, STEM, and HAADF-STEM images of 2D Fe-SASC, respectively. (e) C, N, O and Fe elemental mapping images of 2D Fe-SASC.

X-ray absorption spectroscopy (XAS) measurements were used to determine the local structural and electronic states of Fe atoms in the 2D Fe-SASC. Compared with Fe foil, the absorption edge of Fe K-edge X-ray absorption near-edge structure (XANES) spectrum of 2D Fe-SASC is located at higher energies, but between the two reference samples (FeO and Fe_2O_3), indicating that Fe

atoms in 2D Fe-SASC have positive charges between +2 and +3 (**Figure 4.3a**). Moreover, in

Figure 4.3b, only a main peak at about 1.5 Å exists in the Fourier-transformed (FT) k^2-weighted

EXAFS curve of 2D Fe-SASC, which is mainly attributed to the Fe-N$_x$ first coordination shell.

The wavelet transform (WT) shows remarkable resolution in both k and R space, and Fe K-edge

EXAFS oscillations are analyzed here.
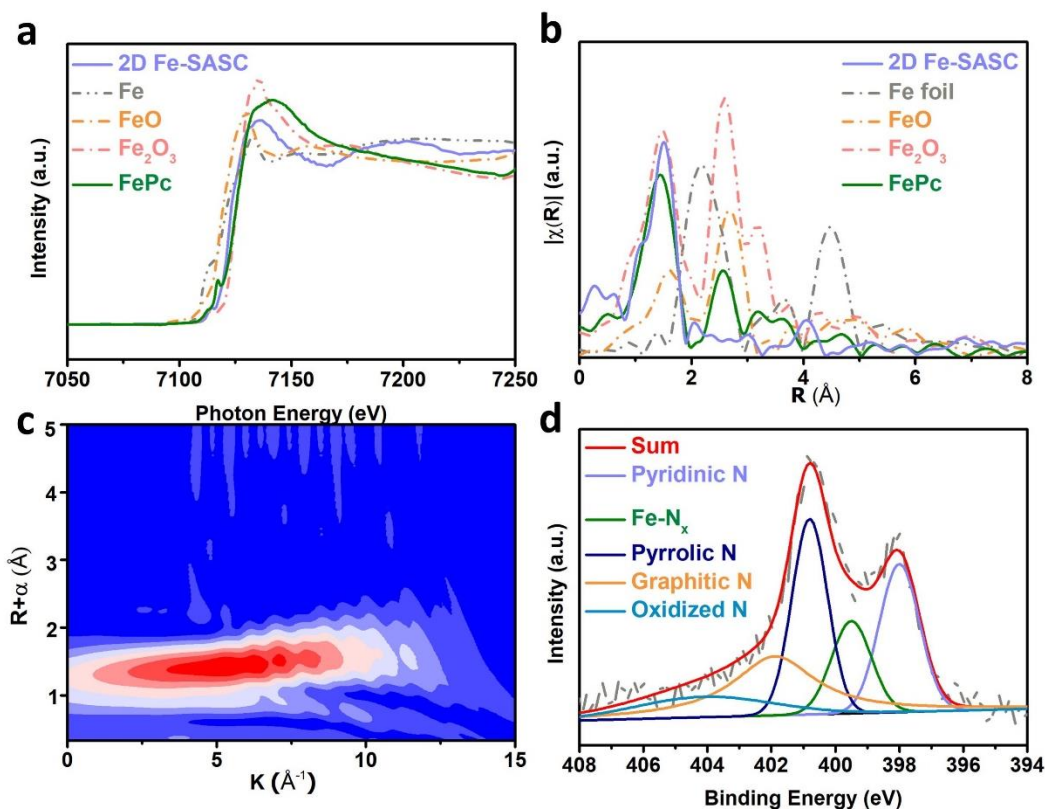
Figure 4.3 (a) Fe K-edge XANES spectra of 2D Fe-SASC, and reference samples of FePc, Fe, FeO, and Fe$_2$O$_3$. (b) FT k^2-weighted EXAFS R-space spectra of 2D Fe-SASC, FePc, Fe foil, and Fe$_2$O$_3$. (c) Full-range WT representation of the EXAFS signal for a representative 2D Fe-SASC. (d) N 1s spectrum of 2D Fe-SASC.

In **Figure 4.3c**, the intensity maxima at ~5 Å^{-1} for 2D Fe-SASC can be attributed to Fe-N bonding.

Most importantly, no intensity corresponding to Fe-Fe is observed, which illustrates that all the

doped Fe in the 2D Fe-SASC are existed as single atom form. All the above results are consistent

with the HAADF-STEM results.

The chemical composition of 2D Fe-SASC was carried out by X-ray photoelectron spectroscopy (XPS). The complex N 1s spectrum of 2D Fe-SASC is deconvoluted into several main peaks (**Figure 4.3d**), which correspond to pyridinic N (398.0 eV), pyrrolic N (400.7 eV), graphitic N (401.8 eV) and oxidized N (404.3 eV), respectively.[29] Notably, the spectral valley between the two main pyridine and pyrrolic peaks at 399.5 eV indicates the presence of Fe-N_x single-atomic sites, [30] which is in good agreement with EXAFS results.

4.3.2 Peroxidase-like activities evaluation of 2D Fe-SASC

Based on the standard analytical procedure of the Nature protocol, the peroxidase-like activity of 2D Fe-SASC was validated using TMB as a typical substrate, and the results are shown in **Figure 4.4a**. The absorbance values show a typical chromogenic reaction, which can only be triggered in the presence of H_2O_2, while 2D Fe-SASC oxidizes the substrate to its corresponding oxidation product. The typical absorbance-time curve is in **Figure 4.4b**. Absorbance at 652nm increased along with time, and a linear relationship (R^2=0.998) was obtained by linear regression analysis in the first minute.

Then the catalytic activities expressed in units (U) of 2D Fe-SASC was calculated (**Figure 4.4c**), by plotting the catalytic activities against the amount of 2D Fe-SASC, the peroxidase-mimicking specific activity of the synthesized 2D Fe-SASC is calculated to be 90.11 U mg^{-1}, which is superior to the most reported POD-like nanomaterials since 2D structure is beneficial for exposing single-atomic sites, thus boosting the specific activity of the 2D Fe-SASC. Compared with bulk materials in which active sites are located inside and blocked, the 2D structure of our material helps to expose more single atomic active sites on the surface and achieve higher active site atom utilization. Another reason is that the high surface area and large pore volume can greatly facilitate a fast mass transfer, leading to the ultra-high catalytic activity of 2D Fe-SASC. Then the stability against pH

and temperature are verified and shown in **Figure 4.4d** and **e**, it is clear that the 2D Fe-SASC can maintain its activities under a large range of pH and temperature, indicating excellent stability in harsh environments. Finally, the selectivity of 2D Fe-SASC towards H_2O_2 was studied (**Figure 4.4f**), and the neglectable absorbance of 2D Fe-SASC for different interfere revealed a satisfactory selectivity towards H_2O_2.
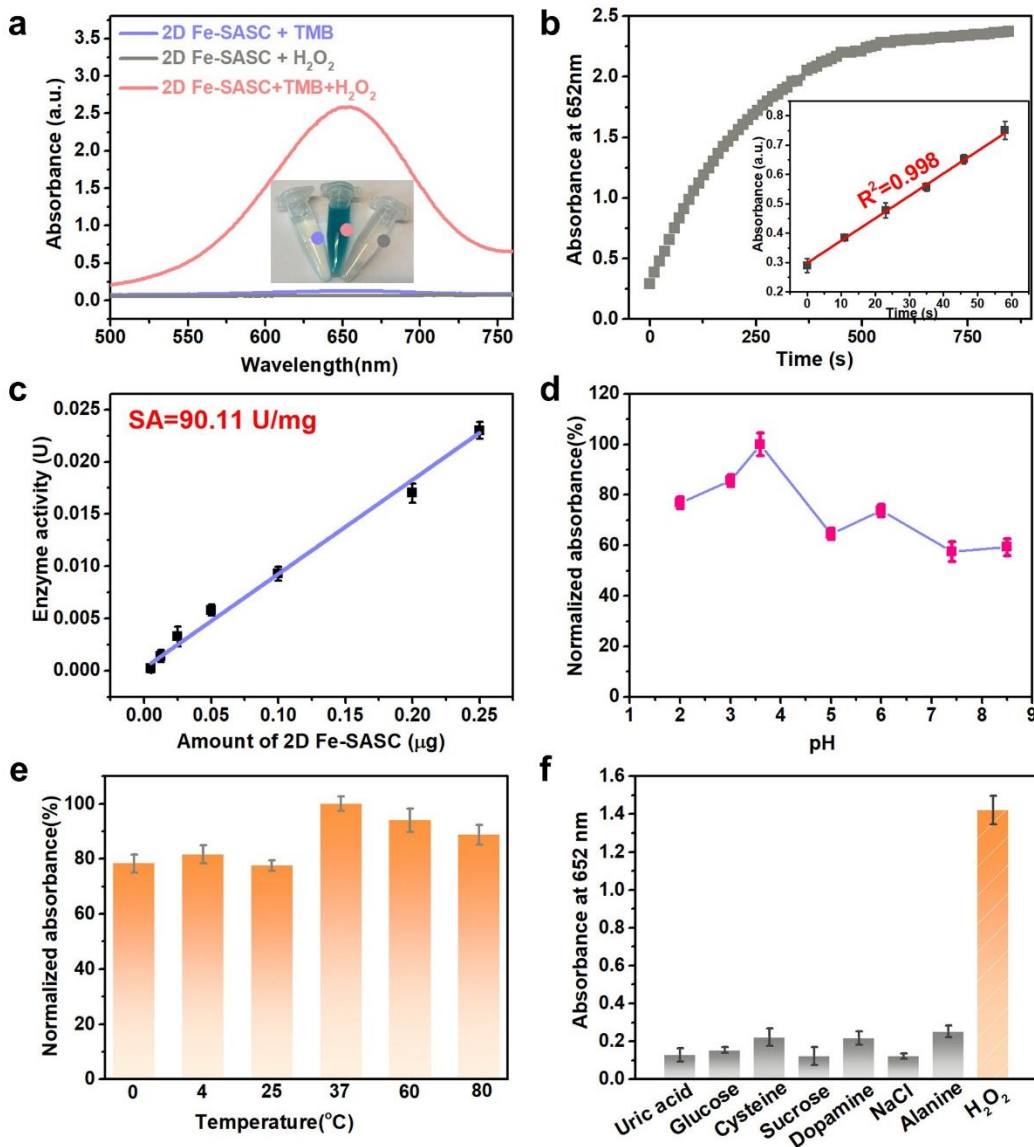
Figure 4.4 (a) Absorption curves of the 2D Fe-SASC in TMB, H_2O_2, and TMB +H_2O_2 solutions, respectively. Insert: photographs of the color changes (blue). (b) Absorbance to time curve of TMB chromogenic reaction catalyzed by 2D Fe-SASC, inserted is the magnified linear portion. (c) Specific activities of 2D Fe-SASC. (d-e) Robustness of 2D Fe-SASC against temperature and pH, respectively. (f) Specificity evaluation of 2D Fe-SASC for various interferences.

To further understand the role of single atomic active sites in the catalytic process, KSCN was used because a stable chelate complex could be formed between SCN^- and catalytic sites, thereby blocking Fe activity sites and failing to decompose H_2O_2, results are shown in **Figure 4.5a**. As the amount of KSCN increased, the absorbance value of ox-TMB dropped sharply, indicating that the greatly reduced catalytic activity is due to the blocked Fe active site, which in turn proves that the atomically dispersed Fe active sites are the main source for its peroxidase-like activity. It is believed that the active intermediates are involved in the colorimetric reaction which can be verified by several scavengers.[31]
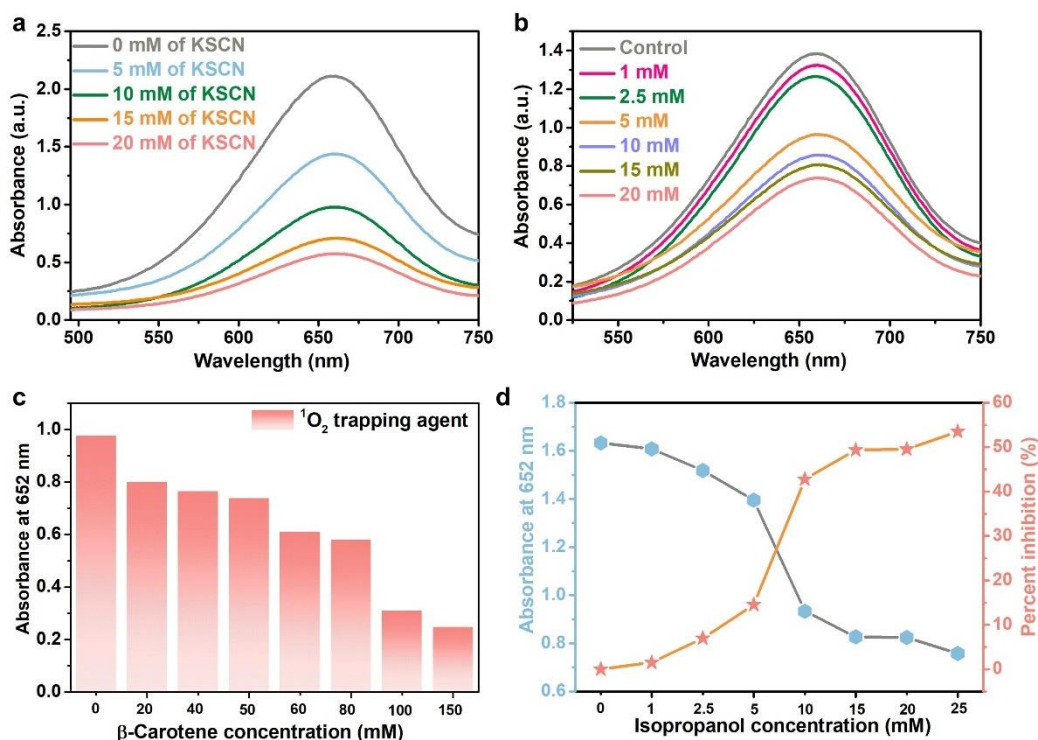
Figure 4.5 (a) Absorbance curves against KSCN with various concentrations. (b) Absorbance curves against various amounts of NaN_3. (c) Absorption changes and percent inhibition after adding isopropanol with different concentrations. (d) Absorption changes after adding different amounts of β-carotene.

In **Figure 4.5b**, NaN_3 served as the $\bullet OH/{}^1O_2$ scavenger, and the absorbance value of ox-TMB decreases significantly along with the NaN_3 addition, proving the participation of $\bullet OH/{}^1O_2$ in oxidation coloration reaction. Similarly, experimental results shown in **Figure 4.5c** verified the

little presence of $^1O_2$, the signal decreased with the increasing addition of β-carotene.[32] Besides, the generated •OH was detected and its participation is verified by the enhanced isopropanol inhibition ability (**Figure 4.5d**).

4.3.3 Optimization for 2D Fe-SASC-LISA

2D Fe-SASC labeled secondary antibody was used in a competitive immunoassay (2D Fe-SASC-LISA) for 2,4-D detection, and several parameters were optimized, the results are shown in **Figure 4.6a**. Choosing the right blocking agent is critical in ELISA systems, and excellent blocking can help reduce the non-specific binding of proteins and produce low background reads. A variety of blocking buffers have been selected to reduce the non-specific adsorption of 2D Fe-SASC labeled secondary antibody, the blocking solution of 3% BAS+0.05% Tween was chosen for its relatively low absorbance value, expected to reduce nonspecific binding and subsequently increase the signal to background ratio, thus increasing the sensitivity of the 2D Fe-SASC-LISA.
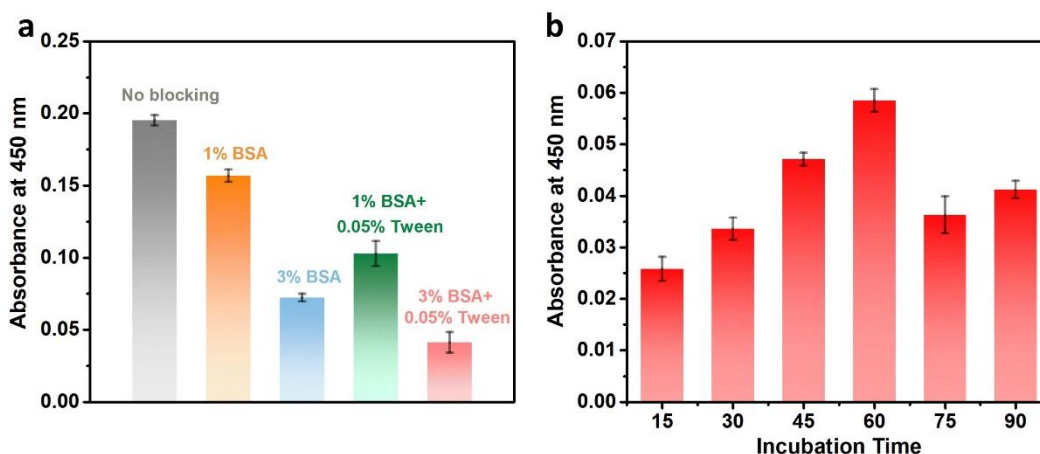
Figure 4.6 (a) Optimization of blocking solution with various solutions. (b) Optimization of incubation time of the mixture of primary antibody and 2,4-D

The incubation time of the mixture of primary antibody and 2,4-D is critical for antibodies binding onto the hapten on the plate, which can contribute significant effects on the performance of the assay. It shows that with the increasing incubation time, the absorbance value first increased while

decreasing after 60 min, which could be ascribed to the activity of the antibody decreased with the prolonging of incubation time (**Figure 4.6b**). As a result, 60 min was chosen as the best incubation time for the 2D Fe-SASC-LISA.

4.3.4 Detection performance of 2D Fe-SASC linked immunosorbent assay

The detection performance of our 2D Fe-SASC linked immunosorbent assay (2D Fe-SASC-LISA) is shown in **Figure 4.7**, in which 2D Fe-SASC is used as the substitution of natural HRP. **Figure 4.7a** shows the competitive immunoassay principle, 2,4-D hapten was immobilized directly on a 96-well polystyrene plate, then conjugated with the 2D Fe-SASC labeled 2,4-D primary antibody specific for the hapten, thus catalyzing a colorimetric reaction with TMB into a visible signal.

The 2D Fe-SASC-LISA detection results towards 2,4-D are shown in **Figure 4.7b**, the absorbance intensity at 450 nm dropped with the increasing addition of 2,4-D, which is in accordance with the principle of competitive ELISA. The relation between absorbance intensity and 2,4-D concentration is presented in **Figure 4.7c**, in the inserted figure, an excellent linear relation of 5ng/mL to 250 ng/mL can be observed, and the linear regression equation was fitted as $I=1.189-0.43 \lg (C)$ with the correlation coefficient of 0.995, in which I refers to the absorbance intensity and the C is the 2,4-D concentration. The limit of detection (LOD) is defined as the concentration of 2,4-D corresponding to the signal intensity which is equal to the mean signal intensity of 0 ng/mL (measured 5 times) minus 3 times the standard deviation. The LOD of 2D Fe-SASC-LISA was calculated to be 0.72 ng/mL. The improved detection performance can be ascribed to the favorable active sites with enhanced catalytic activity provided by the 2D Fe-SASC.

Finally, the specificity of 2D Fe-SASC-LISA was evaluated, and the results are shown in **Figure 4.7d**, other herbicides and pesticides such as glyphosate (Gly), acetochlor (Ace), phosmet (Pho), and chlorpyrifos (Chl) with the concentration of 1ug/mL were used as interference molecules to

80

evaluate specificity, while the concentration of 2,4-D was 200ng/mL. Only 2,4-D can trigger the colorimetric response change while the interferences can only produce a neglectable color change, proving the high specificity of our 2D Fe-SASC-LISA.
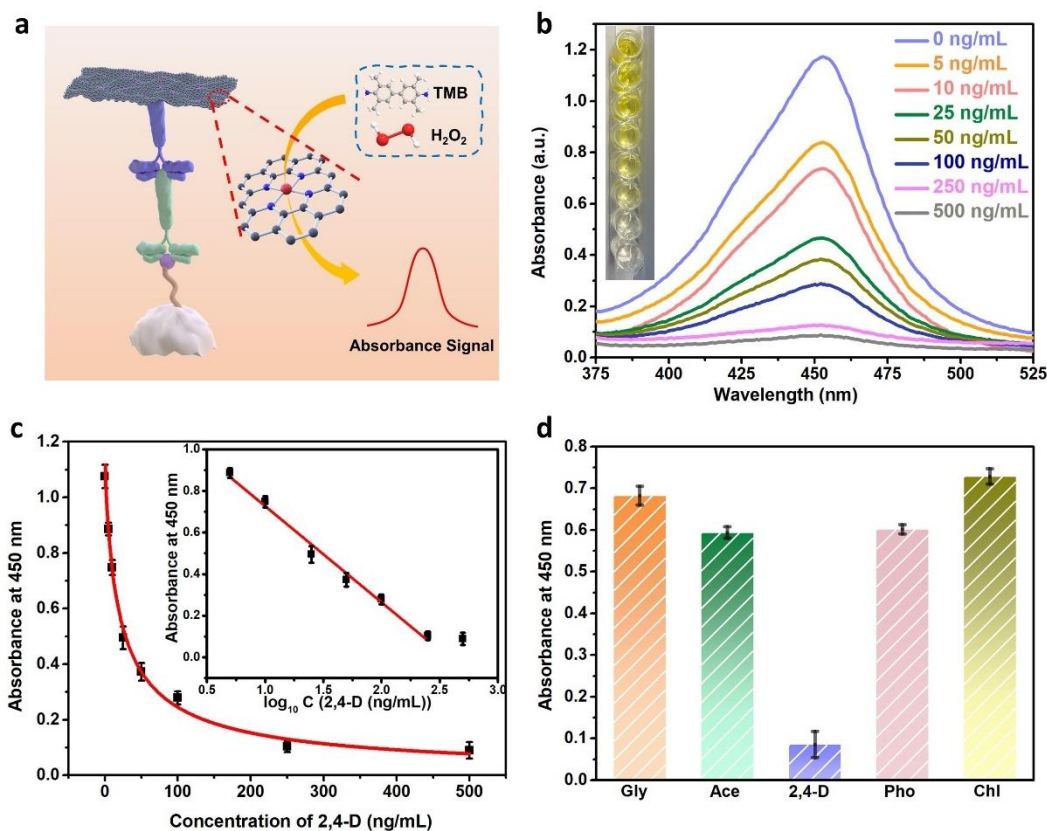
Figure 4.7 (a) Schematic illustration of the 2D Fe-SASC-LISA for 2,4-D detection. (b) Detection performance of 2D Fe-SASC-LISA towards 2,4-D (Inserted is the linear detection range). (c) Absorbance spectra of 2,4-D under different concentrations. (d) Absorbance values for different targets.

Lastly, the spike and recovery experiments were taken out to evaluate the analytical reliability and accuracy of 2D Fe-SASC-LISA in real samples, as in **Table 4.1**. The recovery rates were in the range of 96.8-105.4%, with relative standard deviations (RSDs) of 1.87-7.02%. The high recovery level and low variability results indicate the reliability and accuracy of the proposed 2D Fe-SASC-LISA on 2,4-D detection in actual samples.

Table 4.1 Spiked-recovery test of the proposed 2D Fe-SASC-LISA in human urine (n=3)

Sample No.	Added (ng mL^{-1})	Found (ng mL^{-1})	Recovery (%)	RSD%
1	5	5.27	105.4	5.73
2	10	9.68	96.8	3.26
3	50	49.38	98.8	1.87
4	100	103.27	103.3	7.02

4.4 Conclusion

In summary, the 2D Fe-SASC catalyst was successfully synthesized with excellent peroxidase-mimicking activity, which is mainly attributed to the 2-dimensional structure that can help expose more single atomic sites and enable 100% Fe atom utilization. Compared to natural HRP, 2D Fe-SASC also shows excellent stability against harsh environments. Most importantly, using 2D Fe-SASC in competitive ELISA achieves a satisfactory detection performance 2,4-D with high sensitivity (LOD is calculated as 0.72 ng/mL) and a wide detection range (1-500ng/mL). Based on the high activity of 2D Fe-SASC and improved ELISA performance, the peroxidase-like 2D Fe-SASC shows great potential in designing a compactivity ELISA kit with improved sensitivity for detecting various target biomarkers.

REFERENCES

1. F. Islam, J. Wang, M.A. Farooq, M.S.S. Khan, L. Xu, J. Zhu, M. Zhao, S. Muños, Q.X. Li, W. Zhou, Potential impact of the herbicide 2,4-dichlorophenoxyacetic acid on human and ecosystems, Environment International, 111 (2018) 332-351.

2. E.K. Sheiner, E. Sheiner, R.D. Hammel, G. Potashnik, R. Carel, Effect of occupational exposures on male fertility: literature review, Industrial Health, 41 (2003) 55-62.

3. A. Ganguli, D. Choudhury, G. Chakrabarti, 2, 4-Dichlorophenoxyacetic acid induced toxicity in lung cells by disruption of the tubulin-microtubule network, Toxicology Research, 3 (2014) 118-130.

4. G.E. Peterson, The discovery and development of 2, 4-D, Agricultural History, 41 (1967) 243-254.

5. H. Wang, Q. Xu, J. Wang, W. Du, F. Liu, X. Hu, Dendrimer-like amino-functionalized hierarchical porous silica nanoparticle: A host material for 2,4-dichlorophenoxyacetic acid imprinting and sensing, Biosensors and Bioelectronics, 100 (2018) 105-114.

6. A. Blair, H. Malker, K.P. Cantor, L. Burmeister, K. Wiklund, Cancer among farmers: a review, Scandinavian journal of work, Environment & Health, (1985) 397-407.

7. C.f.D. Control, Prevention, Third national report on human exposure to environmental chemicals: executive summary, (2005).

8. H. Canada, Third report on human biomonitoring of environmental chemicals in Canada: results of the Canadian health measures survey cycle 3 (2012-2013) by the minister of health, Journal of Occupational and Environmental Hygiene, 16 (2015) 763-774.

9. S.A. Venners, N. Khoshnood, M. Jeronimo, A. Sobkowicz, P. Provencher, G. Tang, W. Chu, R. Copes, Adult and child urinary 2 , 4-D in cities with and without cosmetic pesticide bylaws: a

population-based cross-sectional pilot study, Journal of Exposure Science & Environmental Epidemiology, 27 (2017) 484-490.

10. K.W. Thomas, M. Dosemeci, J.A. Hoppin, L.S. Sheldon, C.W. Croghan, S.M. Gordon, M.L. Jones, S.J. Reynolds, J.H. Raymer, G.G. Akland, Urinary biomarker, dermal, and air measurement results for 2, 4-D and chlorpyrifos farm applicators in the Agricultural Health Study, Journal of Exposure Science & Environmental Epidemiology, 20 (2010) 119-134.

11. B.D. Curwin, M.J. Hein, W.T. Sanderson, C. Striley, D. Heederik, H. Kromhout, S.J. Reynolds, M.C. Alavanja, Pesticide dose estimates for children of Iowa farmers and non-farmers, Environmental Research, 105 (2007) 307-315.

12. P. Bollella, G. Fusco, C. Tortolini, G. Sanzò, R. Antiochia, G. Favero, F. Mazzei, Inhibition-based first-generation electrochemical biosensors: theoretical aspects and application to 2, 4-dichlorophenoxy acetic acid detection, Analytical and Bioanalytical Chemistry, 408 (2016) 3203-3211.

13. S. Ding, Z. Lyu, S. Li, X. Ruan, M. Fei, Y. Zhou, X. Niu, W. Zhu, D. Du, Y. Lin, Molecularly imprinted polypyrrole nanotubes based electrochemical sensor for glyphosate detection, Biosensors and Bioelectronics, 191 (2021) 113434.

14. D. Schrenk, A. Cartus, Chemical contaminants and residues in food, Woodhead Publishing (2017).

15. I.A. Rather, W.Y. Koh, W.K. Paek, J. Lim, The sources of chemical contaminants in food and their health implications, Frontiers in Pharmacology, 8 (2017) 830.

16. Z. Lyu, S. Ding, N. Zhang, Y. Zhou, N. Cheng, M. Wang, M. Xu, Z. Feng, X. Niu, Y. Cheng, Single-atom nanozymes linked immunosorbent assay for sensitive detection of Aβ 1-40: a biomarker of alzheimer's disease, Research, 2020 (2020).

17. L. Jiao, L. Zhang, W. Du, H. Li, D. Yang, C. Zhu, Hierarchical manganese dioxide nanoflowers enable accurate ratiometric fluorescence enzyme-linked immunosorbent assay, Nanoscale, 10 (2018) 21893-21897.

18. N. Cheng, Q. Shi, C. Zhu, S. Li, Y. Lin, D. Du, Pt-Ni $(OH)_2$ nanosheets amplified two-way lateral flow immunoassays with smartphone readout for quantification of pesticides, Biosensors and Bioelectronics, 142 (2019) 111498.

19. D. Liu, Z. Wang, A. Jin, X. Huang, X. Sun, F. Wang, Q. Yan, S. Ge, N. Xia, G. Niu, Acetylcholinesterase-catalyzed hydrolysis allows ultrasensitive detection of pathogens with the naked eye, Angewandte Chemie, 125 (2013) 14315-14319.

20. Y. Wang, G. Zhao, Y. Zhang, X. Pang, W. Cao, B. Du, Q. Wei, Sandwich-type electrochemical immunosensor for CEA detection based on $Ag/MoS_2@Fe_3O_4$ and an analogous ELISA method with total internal reflection microscopy, Sensors and Actuators B: Chemical, 266 (2018) 561-569.

21. D. Liu, J. Yang, H.-F. Wang, Z. Wang, X. Huang, Z. Wang, G. Niu, A. Hight Walker, X. Chen, Glucose oxidase-catalyzed growth of gold nanoparticles enables quantitative detection of attomolar cancer biomarkers, Analytical Chemistry, 86 (2014) 5800-5806.

22. B. Xu, H. Wang, W. Wang, L. Gao, S. Li, X. Pan, H. Wang, H. Yang, X. Meng, Q. Wu, A Single-atom nanozyme for wound disinfection applications, Angewandte Chemie, 131 (2019) 4965-4970.

23. C. Tan, X. Cao, X.-J. Wu, Q. He, J. Yang, X. Zhang, J. Chen, W. Zhao, S. Han, G.-H. Nam, Recent advances in ultrathin two-dimensional nanomaterials, Chemical Reviews, 117 (2017) 6225-6331.

24. D. Bitounis, H. Ali-Boucetta, B.H. Hong, D.H. Min, K. Kostarelos, Prospects and challenges of graphene in biomedical applications, Advanced Materials, 25 (2013) 2258-2268.

25. F. Yin, B. Gu, Y. Lin, N. Panwar, S.C. Tjin, J. Qu, S.P. Lau, K.-T. Yong, Functionalized 2D nanomaterials for gene delivery applications, Coordination Chemistry Reviews, 347 (2017) 77-97.

26. E. Morales-Narváez, A. Merkoçi, Graphene oxide as an optical biosensing platform, Advanced Materials, 24 (2012) 3298-3308.

27. D. Liu, J.-C. Li, S. Ding, Z. Lyu, S. Feng, H. Tian, C. Huyan, M. Xu, T. Li, D. Du, P. Liu, M. Shao, Y. Lin, 2D single-atom catalyst with optimized iron sites produced by thermal melting of metal-organic frameworks for oxygen reduction reaction, Small Methods, 4 (2020) 1900827.

28. J. Wei, Y. Hu, Y. Liang, B. Kong, J. Zhang, J. Song, Q. Bao, G.P. Simon, S.P. Jiang, H. Wang, Nitrogen-doped nanoporous carbon/graphene nano-sandwiches: synthesis and application for efficient oxygen reduction, Advanced Functional Materials, 25 (2015) 5768-5777.

29. S. Ding, Z. Lyu, H. Zhong, D. Liu, E. Sarnello, L. Fang, M. Xu, M.H. Engelhard, H. Tian, T. Li, An ion-imprinting derived strategy to synthesize single-atom iron electrocatalysts for oxygen reduction, Small, 17 (2021) 2004454.

30. N. Leonard, W. Ju, I. Sinev, J. Steinberg, F. Luo, A.S. Varela, B.R. Cuenya, P. Strasser, The chemical identity, state and structure of catalytically active centers during the electrochemical CO_2 reduction on porous Fe-nitrogen-carbon (Fe-N-C) materials, Chemical Science, 9 (2018) 5064-5073.

31. Y. Zhan, Y. Zeng, L. Li, L. Guo, F. Luo, B. Qiu, Y. Huang, Z. Lin, Cu^{2+}-modified boron nitride nanosheets-supported subnanometer gold nanoparticles: an oxidase-mimicking nanoenzyme with unexpected oxidation properties, Analytical Chemistry, 92 (2019) 1236-1244.

32. H. Tamura, H. Ishikita, Quenching of singlet oxygen by carotenoids via ultrafast super-exchange dynamics, The Journal of Physical Chemistry A, (2020).

CHAPTER FIVE: SINGLE-ATOMIC SITE CATALYST ENHANCED LATERAL-FLOW

IMMUNOASSAY FOR HERBICIDE DETECTION

5.1 Introduction

Lateral-flow immunoassay (LFIA), as an effective POC detection method, is widely reported for monitoring and diagnosis of various specific targets.[1-3] However, the drawback of low sensitivity limits its further practical applications. In the past few decades, the continuous development of nanotechnology has brought vitality to the development of various nano-sized materials with enzyme-like activities.[4, 5] Having been introduced as the label for signal amplification since 2015,[6] these kinds of nanomaterials have allowed LFIA to achieve high-sensitive detection and thus greatly benefited to trace detections. Our group has reported that the enzyme-like nanomaterials linked-LFIA could boost signal amplification for biosensing. An obvious color change on concerned lines can be produced through catalyzing enzyme substrates by the intrinsic peroxidase-like (POD-like) activity of nanomaterials; thus, the detection performance is greatly improved.[7, 8] Though the stability of enzyme-like nanomaterials is much better than their natural counterparts, substantially improving the catalytic activity of this type of nanomaterial still remains a grand challenge.

Regulating the size of nanomaterials, especially downsizing the catalytically active sites on materials to several or even single atoms, has been considered as a potential way to address this challenge. Single-atomic site catalysts (SASCs) have recently attracted widespread attention due to their isolated active metal sites and unique electronic/geometric structures.[9-12] Different from traditional nanomaterials where the catalytic activity mainly comes from surface atoms, the increased catalytic abilities of SASCs come from almost one hundred percent utilization of active metal atoms.[13] Most importantly, the coordination structure of $Fe-N_x$ sites on SASCs vividly

mimics the active sites of natural enzyme.[14-17] Based on these, SASCs not only show a myriad of advantages in electrocatalysis applications,[18, 19] but also exhibit high-performance enzyme-like properties and huge potential in biosensing applications.[20-22] Our previous work developed Fe-N$_x$ SASC to replace natural enzymes in a commercial enzyme-linked immunosorbent assay (ELISA) for early-stage detection of Alzheimer's disease. The designed SASC labeled linked immunosorbent assay is over ten times more sensitive than that of commercial ELISA.[23] Therefore, we believe that the SASCs with enhanced catalytic activity and stability can be an ideal substitute for traditional nanomaterials in LFIA to improve their sensing sensitivity and detection ability.

In this work, we synthesized a single-atomic site iron catalyst (Fe-SASC) and used it in competitive LFIA for POC detection of 2,4-D. Herein, hemin was selected as Fe precursor owing to the existed similar Fe coordination site of the natural enzyme. Owing to the nanoconfinement effect of ZIF-8, the dope hemin sites were directly converted to POD-like active center, and its atomically dispersed iron active sites were proved by aberration-corrected scanning transmission electron microscopy (AC-STEM) image and extended X-ray absorption fine structure (EXAFS). A series of analyses were conducted to reveal the POD-like activity and catalytic mechanism of Fe-SASC. The 2,4-Dichlorophenoxyacetic acid (2,4-D) is selected as a kind of herbicide target in this work. The designed Fe-SASC labeled LFIA (Fe-SASC-LFIA) detection platform is illustrated in Scheme 1. When 2,4-D is not present in the sample, Fe-SASC labeled 2,4-D antibody (Fe-SASC-Ab$_{2,4-D}$) will be captured by the test lines where corresponding haptens (BSA-2,4-D) were immobilized, which the visible label will be displayed (Negative). Conversely, when 2,4-D exists in the sample, it will bind to the antibodies to prevent them from binding to the haptens immobilized on the test line so that no visible label will appear. The Fe-SASC has superior catalytic activity and can be

used as an antibody label to achieve the biorecognition process and amplify the signal. Highly sensitive and specific 2,4-D in human urine was demonstrated using the developed Fe-SASC-LFIA. The results prove that the Fe-SASC-LFIA exhibited excellent sensitivity and practical applicability, making the fabricated bioassays with satisfactory detection ability and feasibility in clinical diagnosis.

5.2 Experimental

5.2.1 Preparation of Fe-SASC

Hemin (160 mg) and Zn $(NO_3)_2 \cdot 6H_2O$ (3.39 g) were added to 150 mL methyl alcohol and dissolved by stirring for 10 min (Solution A). MeIM (3.94 g) was dissolved in 150 mL methyl alcohol to prepare Solution B and then poured Solution B into Solution A with stirring for 1 min. After that, the obtained mixture was allowed to stand overnight at 60°C. The hemin-doped ZIF-8 precursor was collected after centrifugation at 8000 rpm. Finally, Fe-SASC was obtained from the pyrolytic process at 1100°C under nitrogen and ammonia atmosphere for 30 min, respectively. Then acid washing using 3M HCl at 60°C for 4h was performed.

5.2.2 Preparation Fe-SASC labeled antibody

The Fe-SASC labeled antibody (Fe-SASC-Ab$_{2,4-D}$) was successfully prepared through an amide binding between Ab$_{2,4-D}$ and carboxy-terminated Fe-SASC by EDC/NHS amidation reaction. [24-26] Specifically, 1.0 mL of 1.0 mg/mL Fe-SASC was dispersed in 0.05% Nafion (in Ethanol), and the pH value was adjusted to 6 with 0.02 M K_2CO_3. Subsequently, the Fe-SASC solution was activated with NHS (4 mg/mL) and EDC (2 mg/mL) by gently shaking for 30 minutes, then washed by centrifuging with PBS three times to obtain the active Fe-SASC. 10 μL of 2,4-D antibody (1 mg/mL in PBS) with active Fe-SASC was incubated at 37 °C for 1 hour and centrifuged at 13000

RPM for three times to remove the unbonded antibodies. Finally, 1% BSA in PBS was used to passivate the products for 30 minutes and the final product was dispersed in 1 mL of PBS and stored at 4 °C for further use.

5.2.3 Preparation of Fe−SASC labeled competitive LFIA

The Fe-SASC-LFIA was comprised of the following components: a sample pad, a conjugate pad, a nitrocellulose membrane, an absorbent pad, and a backing pad. The sample pad (glass fiber, 17 mm × 30 cm) was treated with a buffer (PBS containing 2% BAS and 2% Sucrose), then dried at 37 °C for 2 h. Test line (1 μL/cm, 30 μL 2,4-D BSA) and control line (1 μL/cm, 30 μL Goat anti-mouse IgG) prepared at different locations on the nitrocellulose membrane (25 mm× 30 cm) by BioJet BJQ 3000 dispenser (BioDot, Irving, California, USA), then dried at 37 °C overnight and stored at 4 °C. The treated sample pad, nitrocellulose membrane and fiber absorbent pad were laminated on a backing card (60 mm × 30 cm). The overlapping length between each pad was approximate 1-2 mm to ensure the migration of solution. After all components were assembled on the backing card, this card is cut into strips with a width of 4 mm using a BioDot module CM4000 paper cutter (Irvine, CA, USA). These lateral flow strips were then ready to use for 2,4D tests.

5.3. Results and discussion

5.3.1 Synthesis and structure characterization of Fe-SASC

The designed Fe-SASC labeled LFIA (Fe-SASC-LFIA) detection platform is illustrated in **Figure 5.1.** Preparation of hemin-doped ZIF-8 precursor is similar to the previous report[27] except for adding a certain amount of hemin, as shown in **Figure 5.1a**.
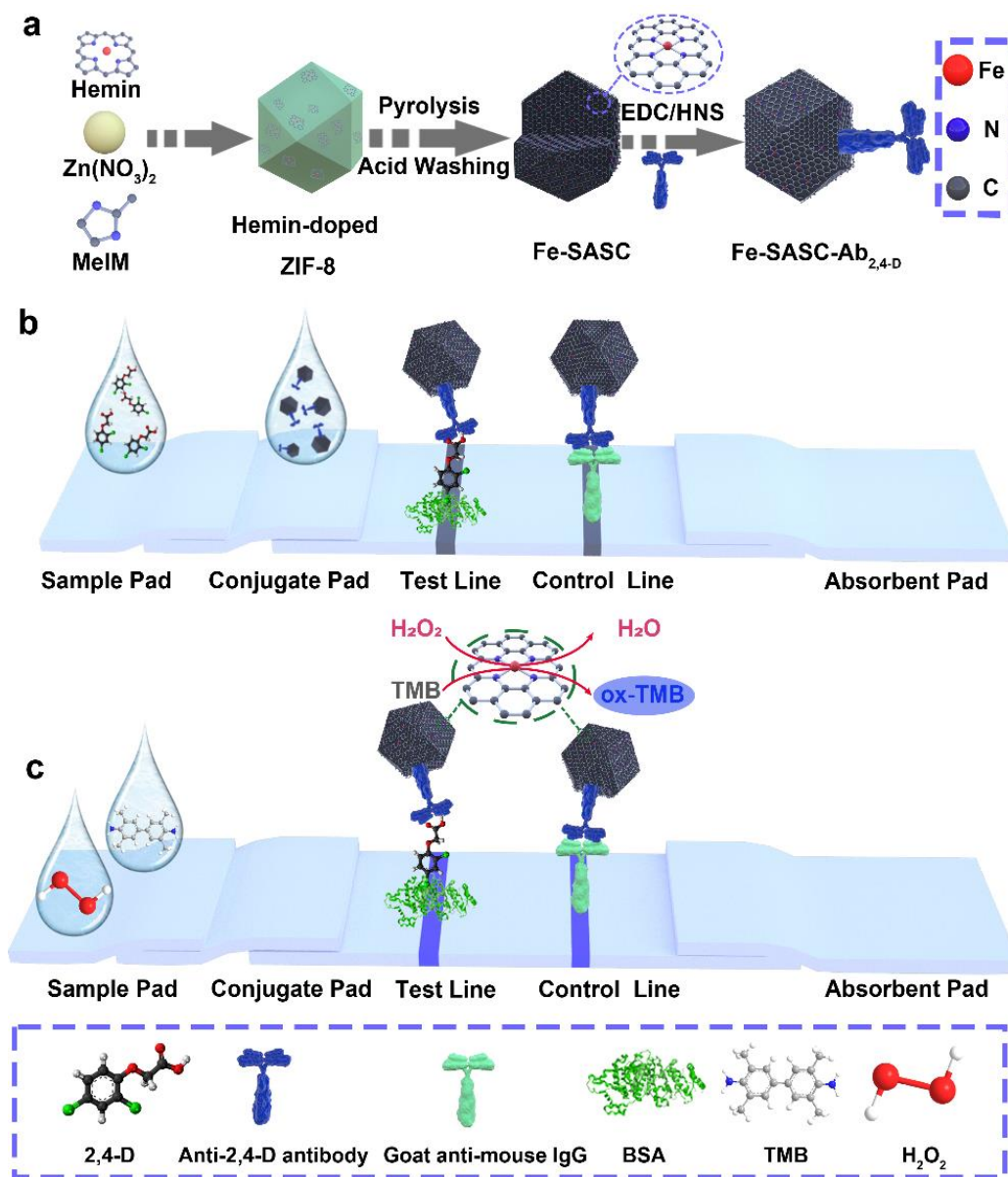
Figure 5.1 Schematic illustration of (a) preparation process of the Fe-SASC and Fe-SASC-Ab$_{2,4\text{-}D}$. (b) Fe-SASC enhanced competitive lateral flow immunoassay (Fe-SASC-LFIA) for detection of 2,4-D.

Figure 5.2a-**c** exhibit the morphologies of the hemin-doped ZIF-8 precursor and the synthesized Fe-SASC, respectively. Similar to the hemin-doped ZIF-8 precursor, the dodecahedral structure is well maintained after the pyrolysis process to form the Fe-SASC (**Figure 5.2b** and **c**). The average size of the synthesized Fe-SASC is around 100 nm, and such a small size meets the liquidity

requirements of the LFIA sensing process. The selected area electron diffraction (SAED) pattern in **Figure 5.2c** shows no diffraction spots, which means no crystalline phase is present in Fe-SASC.
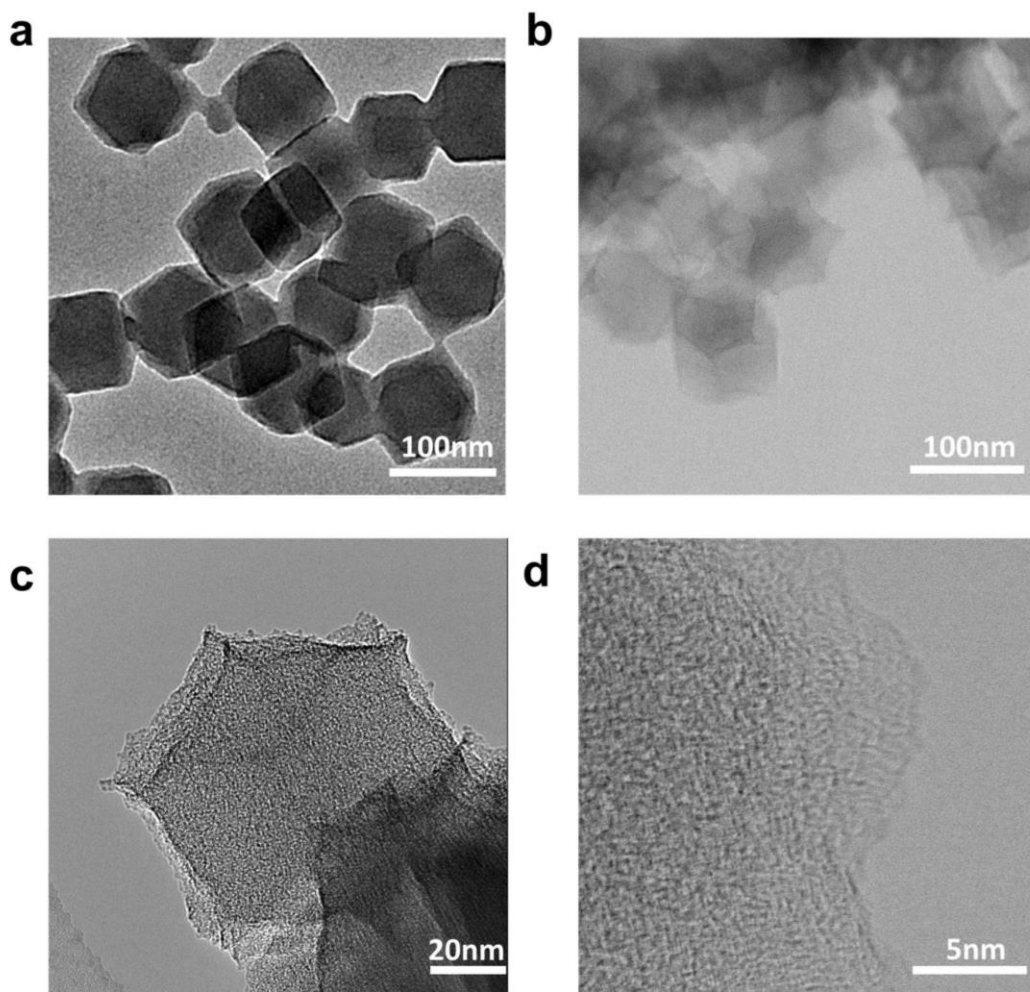
Figure 5.2 (a) TEM image of hemin-doped ZIF-8 precursor. (b and c) Low and high magnification TEM images of Fe-SASC, Inset in Figure 1c: The SAED pattern of Fe-SASC. (d) BF-STEM image of Fe-SASC.

The bright-field scanning TEM (BF-STEM) image (**Figure 5.2d**) confirms that Fe-SASC is composed of distorted graphitic carbon without any metal clusters. These analysis results support that catalytically active sites of SASC are formed at the single Fe atomic level. Such active sites are believed rich in high specific surface area and vast nanopores of the SASC. Besides, due to the doping of macromolecule hemin as the Fe precursor, lots of micropores are also formed here to improve the specific surface area and enhance catalytic efficiency.[28]
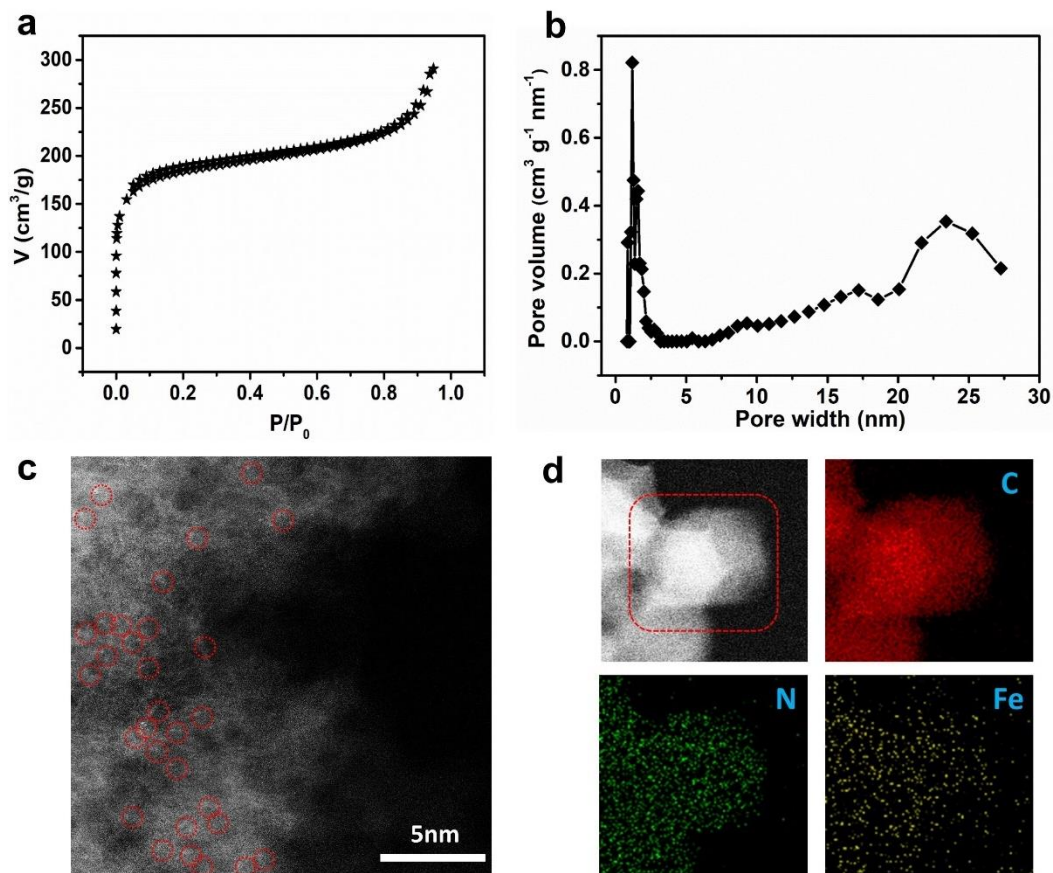
Figure 5.3 (a) The N_2 adsorption/desorption isotherm curves of Fe-SASC. (b) Pore distribution of Fe-SASC by NLDFT. (c) HAADF-STEM image of Fe-SASC. (d) HAADF-STEM image and the corresponding EDS elemental mapping of Fe-SASC.

The specific surface area of Fe-SASC was evaluated by N_2 adsorption-desorption measurement, which is calculated around 664.91 m^2 g^{-1} from Brunauer-Emmett-Teller (BET) method. The corresponding isotherm curve (**Figure 5.3a**) indicates that Fe-SASC has both micropores and mesopores, supported by the obvious adsorption and hysteresis in the low-pressure zone (P/P_0 = 0-0.1). Nonlocal density functional theory (NLDFT) was also carried out to analyze the specific pore distributions (**Figure 5.3b**). Application of high-angle annular dark-field STEM (HAADF-STEM) imaging was applied to study the atomic level structure of Fe-SASC (**Figure 5.3c**). The observed isolated bright spots are circled by red circles, indicating that plentiful single atom Fe sites are anchored on Fe-SASC. In addition, the energy-dispersive X-ray spectroscopy (EDS)

elemental mapping is applied to verify that the C, N, and Fe elements are uniformly distributed on the nanostructure (**Figure 5.3d**).

The chemical state and coordination environment of Fe center was investigated by X-ray absorption spectroscopy analysis, and the X-ray absorption near-edge structure (XANES) spectra reveal that the absorption edge position of Fe-SASC is between FeO and Fe_2O_3, indicating that the average valence state of Fe atoms is between Fe^{+2} and Fe^{+3} (**Figure 5.4a**). In **Figure 5.4b**, Fourier transforms (FT) from extended X-ray absorption fine structure (EXAFS) indicate that Fe-SASC only exhibits a prominent peak at 1.57 Å, which corresponds to the Fe-N first coordination shell in the hemin reference sample. Most importantly, no obvious Fe-Fe peak (2.22 Å) nor other high-shell peaks are observed, confirming that Fe in Fe-SASC exists as the isolated atom form. Moreover, Fe K edge EXAFS oscillations were analyzed by Wavelet transform (WT). In **Figure 5.4c**, from the WT contour plots, only one intensity maximum at about 5.5 $Å^{-1}$ can be observed, and no Fe-Fe intensity maximum corresponding is detected compared with the WT plots of Fe foil, Fe_2O_3, and FeO (**Figure 5.4d** and **f**).

X-ray photoelectron spectroscopy (XPS) analysis was conducted to evaluate the chemical composition of iron atoms, and results show that the quantified Fe content in Fe-SASC is about 0.86 at% (**Figure 5.4g**). The high-resolution N 1s is shown in **Figure 5.4h**, the peaks near 398.4, 399.6, 401.5, and 402.5 eV can be divided into pyridinic, pyrrolic, graphitic, and oxidized N, respectively, which confirms that the nitrogen is indeed incorporated into the carbon matrix. [29] Based on binding energy, a 400.8 eV spectral valley between two main peaks of pyridinic and pyrrolic can be attributed to $Fe-N_x$ species.[15, 30] The inset of **Figure 5.4h** indicates that the percentage of $Fe-N_x$ configuration is 13.2% in all doped N species.
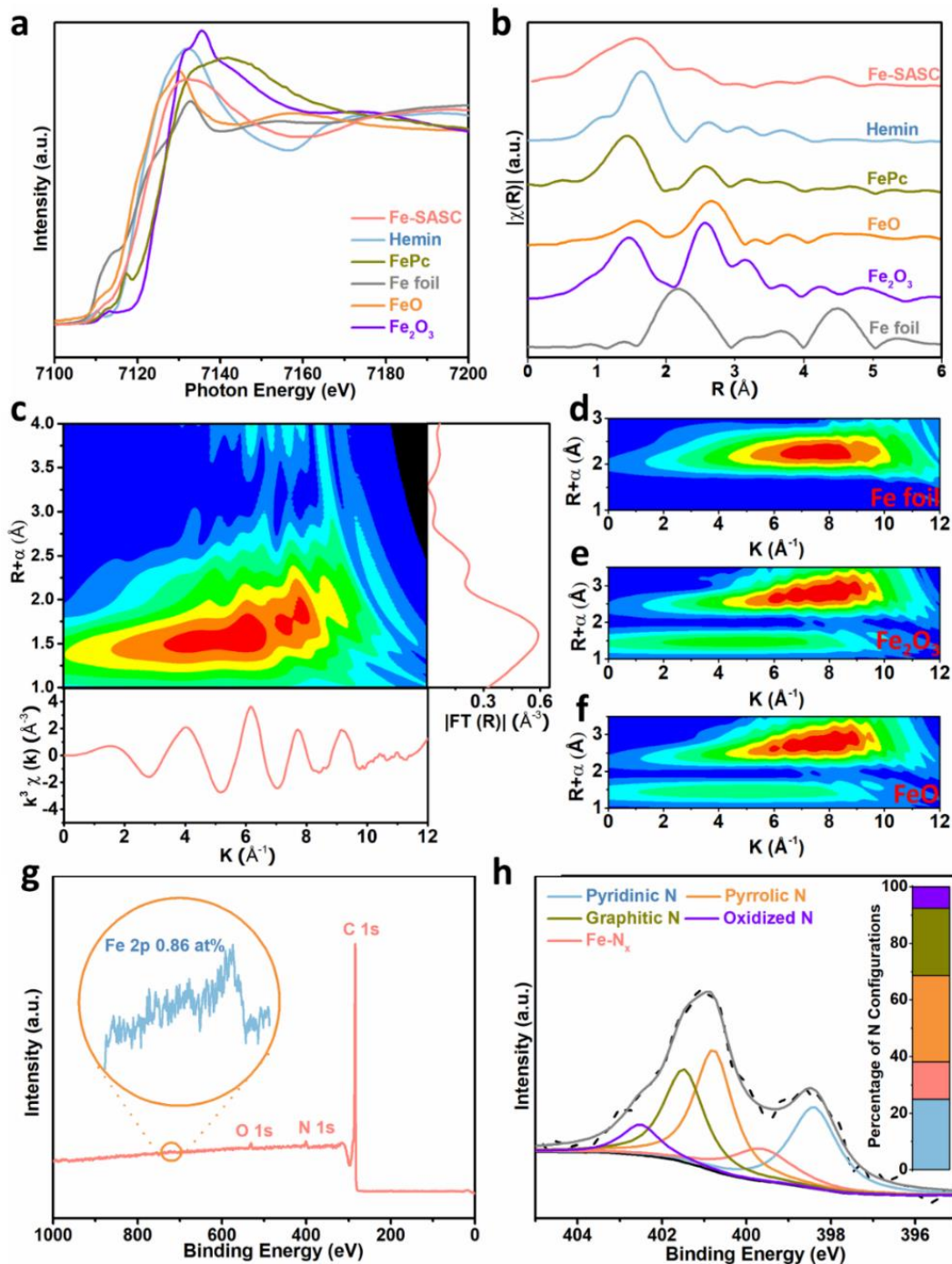
Figure 5.4 (a) Fe K-edge X-ray absorption near-edge structure (XANES) spectrum of Fe-SASC and reference samples of Hemin, FePc, Fe foil, FeO, and Fe_2O_3. (b) FT k^3-weighted extended X-ray absorption fine structure (EXAFS) spectrum of Fe-SASC, Hemin, FePc, Fe foil, FeO, and Fe_2O_3. (c) Full-range WT representation of EXAFS signal for a representative Fe-SASC sample. (d-f) WT of Fe foil, Fe_2O_3, and FeO, respectively. (g) XPS survey spectra with an inset of the high-resolution Fe 2p spectrum. (h) N 1s spectrum of Fe-SASC. Inset: the percentage of N 1s configuration.

5.3.2 Peroxidase-like properties of Fe-SASC

Peroxidase-like properties of Fe-SASC were verified by typical chromogenic reactions, in which 3,3′,5,5′-tetramethylbenzidine (TMB) was used as substrates. As shown in **Figure 5.5a**, the obvious color change and enhanced absorbance intensity prove that TMB is oxidized by the Fe-SASC in the presence of H_2O_2.
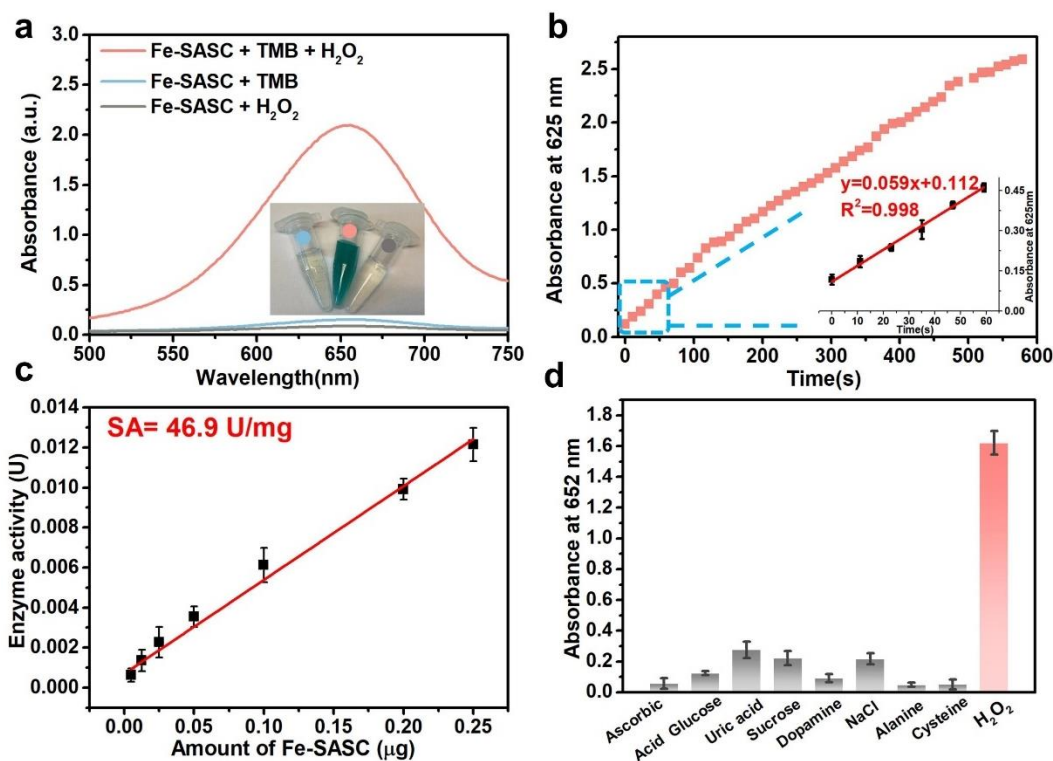
Figure 5.5 (a) Absorption curves of the Fe-SASC in the solution of TMB, H_2O_2, and TMB + H_2O_2, respectively. Insert: photographs of the color changes. (b) TMB chromogenic reaction curve of absorbance to time catalyzed by Fe-SASC and the inset is the initial linear portion. (c) The relationship between specific activity (SA) of Fe-SASC and its amount. (d) Specificity evaluation of Fe-SASC for various interferences.

The typical absorbance curve of TMB-Fe-SASC chromogenic reaction within 600s is presented in **Figure 5.5b**, where the absorbance increases with reaction time. In the first 60 s, linear regression analysis can confirm a linear reaction between absorbance and time (R^2=0.998). These results indicate that the Fe-SASC possesses excellent POD-like characteristics and can be used in bioapplications. Catalytic activity expressed in units (U) of Fe-SASC was calculated (**Figure 5.5c**).

The specific activity (SA) was determined to be 46.9 U mg^{-1}, further proving the unprecedented POD-like activities of the synthesized Fe-SASC. This high activity originated from the structural similarity between Fe-SASC and effective structure in natural enzymes.[15, 23] The selectivity of Fe-SASC towards H_2O_2 was analyzed. As shown in **Figure 5.5d**, the presence of H_2O_2 results in a distinct signal, while other competing interference can only produce negligible signals, indicating the satisfactory selectivity of Fe-SASC.
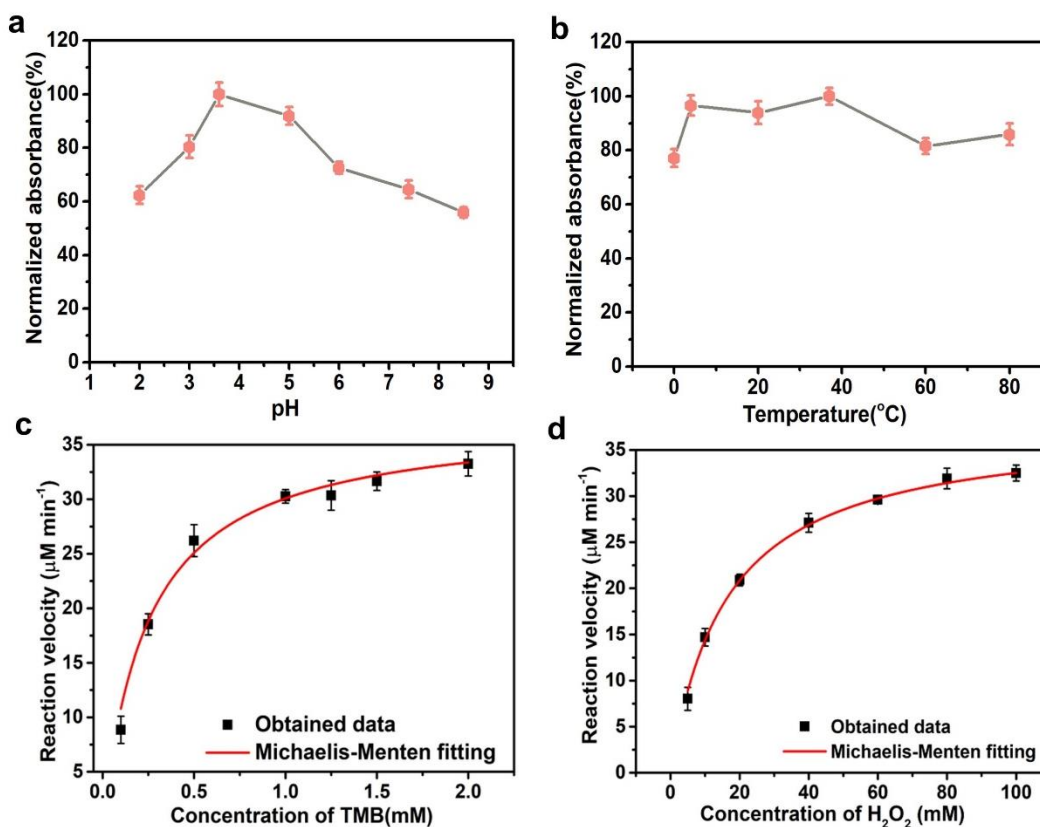
Figure 5.6 (a-b) Robustness of Fe-SASC against various pH and temperature values. (c-d) Steady-state kinetics curves of Fe-SASC toward TMB and H_2O_2.

To evaluate the potential effects of various harsh environments on Fe-SASC, the catalytic activity of Fe-SASC was measured under different pH values and temperatures (**Figure 5.6a** and **b**). The Fe-SASC can maintain its high activity in a wide range of pH values and temperatures. Fe-SASC has the maximum activity under the pH value of 3.5 as well as keeps above 50% activity under different pH values. The Fe-SASC can also preserve over 70% of its activity from 4 to 80°C and

exhibit the highest catalytic activity at 37°C. These results demonstrate that the Fe-SASC can maintain stability under harsh environments. The steady-state kinetics curves of Fe-SASC towards TMB substrates and H_2O_2 were obtained by fitting with the Michaelis-Menten equation, as shown in **Figure 5.6c** and **d,** and the corresponding Michaelis-Menten parameters were listed in **Table 5.1**. Compared to natural Horseradish peroxidase (HRP),[34] Fe-SASC showed a comparable K_m towards H_2O_2 and a relatively low K_m towards TMB, indicating that Fe-SASC has a superior binding affinity toward TMB and a similar affinity level towards H_2O_2.

Table 5.1 Comparison of steady-state kinetics parameters of Fe-SASC and HRP.

Materials	Substrate	K_m (mM)	v_{max}(μM min^{-1})
Fe-SASC	H_2O_2	16.28	36.7
	TMB	0.24	37.8
Natural HRP	H_2O_2	18.64	48.6
	TMB	0.43	55.5

5.3.3 Mechanisms for peroxidase-like activity of Fe-N-C SASC

It is speculated that the excellent heme enzyme-like activity of Fe-SASC originates from the reactive oxygen species (ROS) generated by the decomposition of H_2O_2 on the complex. Based on this, we conducted a series of chemical experiments to study the mechanism of the catalytic process of POD-like Fe-SASC. Firstly, the role of single atom Fe in catalytic efficiency was verified by thiocyanate ions (SCN$^-$). A stable chelate complex can be formed between SCN$^-$ and Fe-centered catalytic sites, thus blocking Fe activity sites and preventing decomposition of H_2O_2. As shown in **Figure 5.7a**, absorbance spectrums drop dramatically as more SCN$^-$ is added, indicating that the atomically dispersed Fe-N$_x$ active sites are the main source of the POD-like activity of Fe-SASC. Then, various scavengers were used to study the active intermediates involved in the POD-like

process (**Figure 5.7b-d**). The intermediate •OH/^{1}O$_2$ was verified in **Figure 5.7b**. The absorbance value of ox-TMB decreased with increasing amounts of the added NaN$_3$, showing that •OH/^{1}O$_2$ is involved in the oxidation coloration reaction.[31] Isopropanol and β-carotene were further used to confirm the existence of •OH and ^{1}O$_2$, respectively (**Figure 5.7c-d**). According to the above results, the oxidation coloration reaction is the result of the combined effect of •OH and ^{1}O$_2$. The strong oxidizing properties of ROS can effectively oxidize the chromogenic substrate.
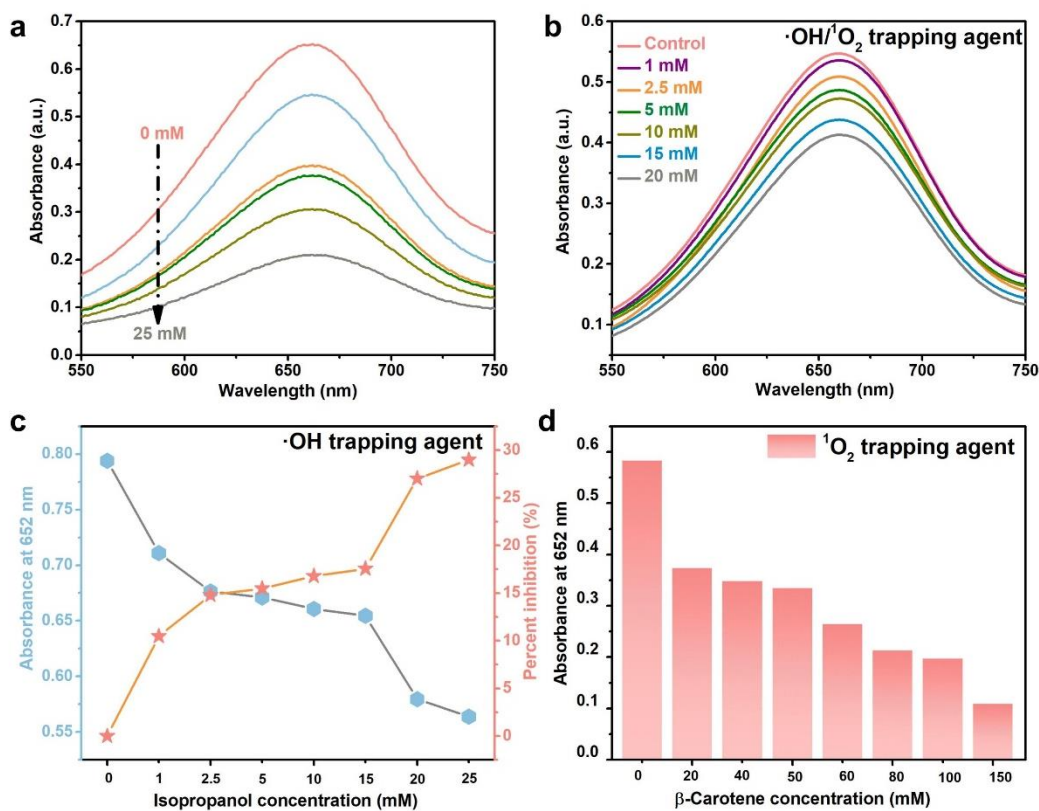
Figure 5.7 Absorption curves upon the addition of various concentrations of (a) KSCN and (b) NaN$_3$ as the •OH/^{1}O$_2$ scavenger. (c) Absorption values and their corresponding inhibition percentage after adding isopropanol. (d) Absorption after adding different amounts of β-carotene.

5.3.4 Optimization for the Fe-SASC labeled Ab$_{2,4-D}$ for LFIA application

The prepared Fe-SASCs were conjugated with Ab$_{2,4-D}$ and used as the signal labels for 2,4-D detection in competitive LFIA. The properties of the labeled antibody (Fe-SASC-Ab$_{2,4-D}$) were investigated by zeta potential characterization (**Figure 5.8a**). The reduced negative charge of Fe-

SASC demonstrating the Ab$_{2,4-D}$ is successfully labeled with Fe-SASC. In LFIA application, the pre-treatment of conjugate pads and the loading amount of Fe-SASC-Ab$_{2,4-D}$ probes are crucial factors in obtaining the best detection performance. Pre-treatment of the conjugate pad will affect the flow rate of the probes to test line (T-line) and control line (C-line) on NC membrane, ultimately affecting the processing time and sensitivity. Herein, the LFIA assembling process and Fe-SASC-Ab$_{2,4-D}$ loading parameter were optimized. The sample pad treated with 2% BSA + 2% sucrose was chosen since it has the highest T-line intensity, indicating the lower nonspecific adsorption on the conjugate pad (**Figure 5.8b**).
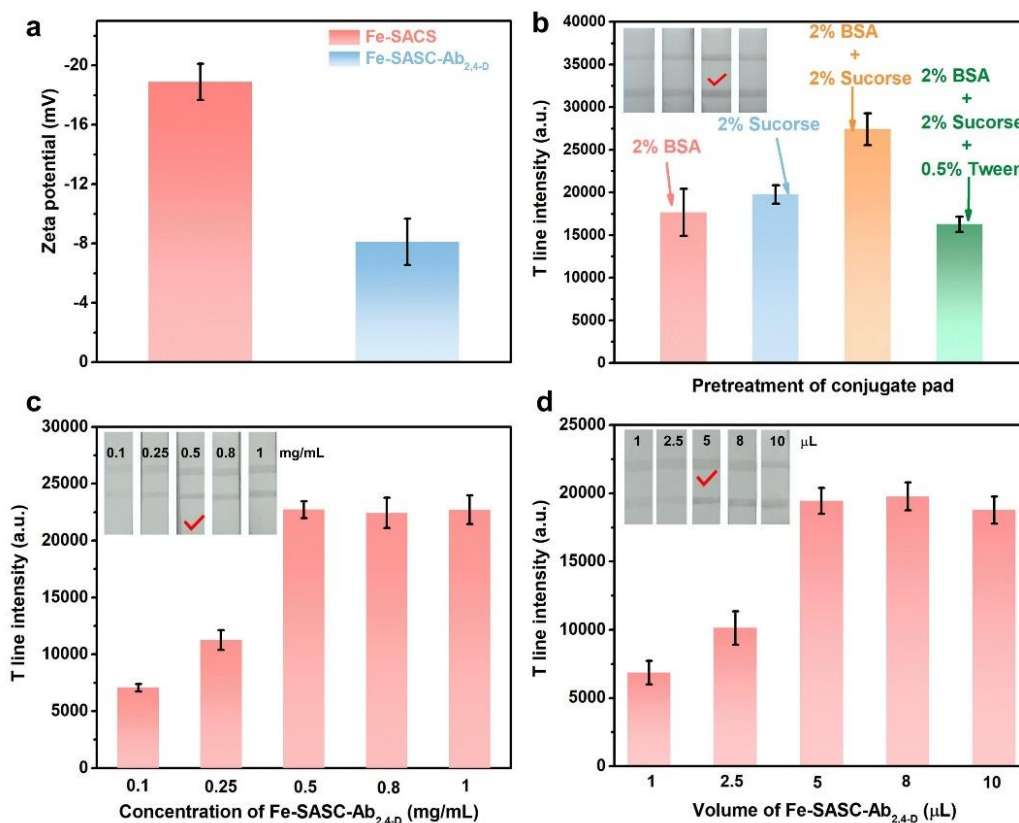
Figure 5.8 (a) Zeta potential analysis of Fe-SASC and Fe-SASC-Ab$_{2,4-D}$ conjugates. (b) Optimization of pre-treatment of the conjugate pads with various solutions. (c) and (d) Optimization of loading amount of concentration and volume of Fe-SASC-Ab$_{2,4-D}$ applied on the sample pad, respectively.

Loading amount of Fe-SASC-Ab$_{2,4-D}$ probes also play an important role since the visualization of the test area is due to the accumulation of probes on the T-line and C-line. Excessive loading of Fe-SASC-Ab$_{2,4-D}$ probes will increase background noise and limit the detection sensitivity, while an insufficient amount will cause weak signal which cannot be discerned compared to the C line or cannot be visualized.[32] As seen in **Figure 5.8c**, the T-line intensity increased along with the increasing concentration or volume of Fe-SASC-Ab$_{2,4-D}$ at first, no obvious difference in T-line intensity is observed when the concentration is above 0.5 mg/mL. After setting the Fe-SASC-Ab$_{2,4-D}$ concentration at 0.5mg/mL, the Volume was also investigated and determined as 5μL, as shown in **Figure 5.8d**. Based on these optimized results, 5 μL of 0.5mg/mL probe are selected as the suitable loading parameters for this system.

5.3.5 Detection performances of the Fe-SASC based LFIA

The optimized Fe-SASC-LFIA was used to detect 2,4-D in standard solutions (in PBS) and human urine samples, and the detection performance of the LFIA was systematically evaluated. **Figure 5.9a** shows the photographs of test/control lines before and after the Fe-SASC enhancement for 2,4-D detection with different 2,4-D concentrations ranging from 0 ng/mL to 250 ng/mL in PBS. For negative samples (no 2,4-D is presented), there is no color difference between T-line and control line that can be observed. For positive samples, the color on T-line is inversely proportional to the 2,4-D concentration and T-line becomes invisible when the 2,4-D concentration is high enough, which is consistent with competitive immuno-reactions. The dramatical enhancement of the detection signal is achieved through the reaction between the TMB and Fe-SASC. After adding TMB/H$_2$O$_2$, the T-line and control line colors change from light grey (color from Fe-SASC) to bright blue (results from Fe-SASC's catalyzing effect), which significantly enhances the signal output and dramatically widen the detection range.
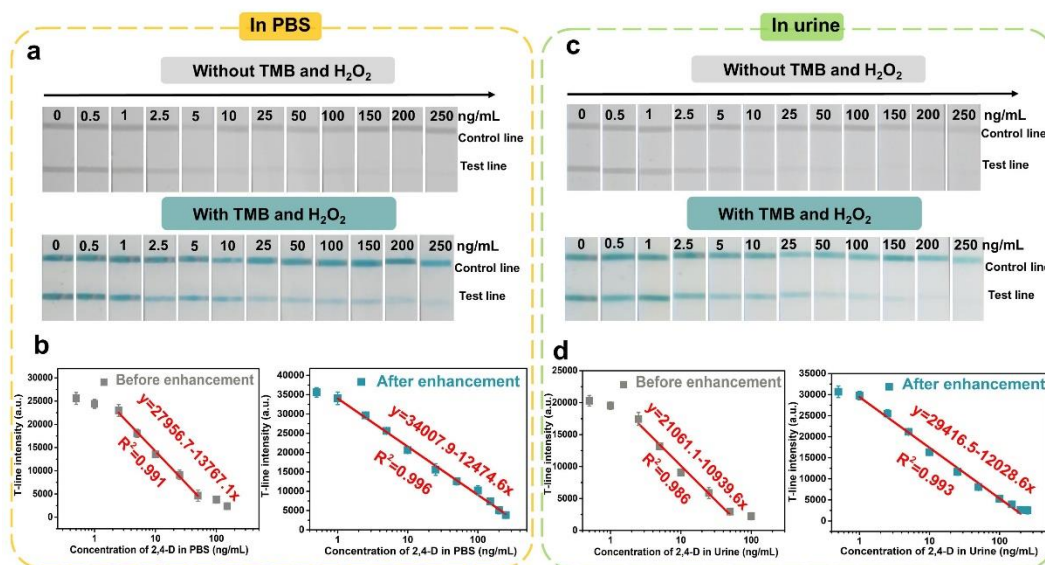
Figure 5.9 Detection performance of Fe-SASC-LFIA for 2,4-D detection. (a) and (c) Typical photographs of Fe-SASC-LFIA in the presence of different 2,4-D levels in PBS and in human urine before and after Fe-SASC enhancement, respectively. (b) and (d) Relationship between the T-line intensity and various concentrations of 2,4-D in PBS and in human urine, respectively.

The accurate quantitative analysis of 2.4-D detection by Fe-SASC-LFIA is conducted by a digital camera and processed with Image J software. As shown in **Figure 5.9b**, there is a linear correlation between the grey T-line intensity and the concentration of 2,4-D in the range of 2.5 to 50 ng/mL before adding TMB/H_2O_2. The limit of detection (LOD) is defined as the concentration of 2,4-D corresponding to the signal intensity, which is calculated by $\bar{S}$-3σ ($\bar{S}$ is the average signal intensity of 0 ng/mL measured 10 times, σ is the standard deviation).[33] LOD of Fe-SASC-LFIA is determined to be 1.54 ng/mL. After the signal enhancement via adding TMB/H_2O_2, we can see a much wider detection ranging from 1 to 250 ng/mL with a lower LOD of 0.82 ng/mL in the Fe-SASC-LIFA. The improved sensitivity and LOD can be attributed to the enhanced signal generated by the enzyme-mimic activity of Fe-SASC. Such excellent detection performance of Fe-SASC-LFIA for 2,4-D detection is also better than other published works (**Table 5.2**). We also analyzed the detection ability in real human urine samples, as shown in **Figure 5.9c** and **d**. Good linear

relations in the range of 2.5 to 50 ng/mL with LOD of 1.82 ng/mL and 1 to 200 ng/mL with LOD of 0.93 ng/mL before and after Fe-SASC enhancement are obtained, respectively. Comparable detection performance was achieved for detection of PBS-based standard solutions and detection of urine samples, proving that the urine matrix has a limited effect on the detection performance of Fe-SASC-LFIA.

Table 5.2 Comparison of our work and other different methods for 2,4-D detetion.

Techniques	LOD (ng mL^{-1})	Linear Range (ng mL^{-1})	Reference
Photoinduced electron transfer (PET)	30.6	30.6-7657.5	[34]
SPR immunosensor	0.5	0.5-1000	[35]
ELISA	1	1-80	[36]
Photoelectrochemical sensor	2.2	110-2874	[37]
Fluoroimmunoassay	0.25	0.25-1	[38]
HPLC	53	160-40000	[39]
HPLC	100	100-400000	[40]
Immunoassay	15	50-1000000	[41]
Fe-SASC-LFIA	0.82	1-250	This work

Moreover, the selectivity of this assay for 2,4-D in human urine was verified by evaluating the impact of interfering substances such as Na^+, K^+, Cl^-, glucose, uric acid (UA) (**Figure 5.10**).[42] Obvious color change on T-line is observed when in the presence of 2,4-D, while other interfering

substances are ineffective, indicating an outstanding selectivity of the proposed Fe-SASC-LFIA towards 2,4-D against potential interfering substances. Spike-recovery experiments evaluated the analytical reliability and accuracy of Fe-SASC-LFIA. Different concentrations of 2,4-D spiked human urine samples were prepared with satisfactory recoveries of 2,4-D in the range from 94.4 to 113.4% are obtained (**Table 5.3**). The high recovery level and low variability results indicate the reliability and accuracy of proposed Fe-SASC-LFIA on 2,4-D detection in actual samples.
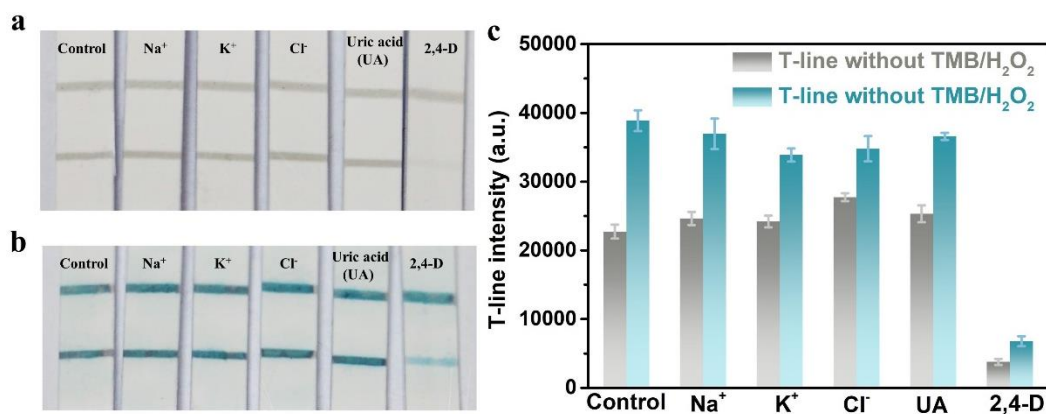
Figure 5.10 (a) and (b) Photographs of Fe-SASC-LFIA towards 2,4-D and interference substances in human urine before and after Fe-SASC enhancement, respectively; (c) Corresponding T-line signal intensities (Concentrations of interfering substances were all 100 ng/ mL, 2,4-D was 25 ng/ mL).

Table 5.3. Spiked-recovery test of urine samples by proposed Fe-SASC-LFIA (n=3)

	Without TMB/ H₂O₂			
Sample No.	**Added (ng mL⁻¹)**	**Found (ng mL⁻¹)**	**Recovery (%)**	**RSD**
1	5	4.72	94.4	5.43
2	10	10.6	106	8.62
3	20	21.9	109.5	7.54
4	40	38.6	96.5	6.36

	With TMB/ H_2O_2			
Sample No.	Added (ng mL^{-1})	Found (ng mL^{-1})	Recovery (%)	RSD
1	5	5.2	113.4	7.26
2	10	9.8	98	6.92
3	20	20.5	102.5	3.43
4	40	39.5	98.5	5.63

5.4 Conclusion

In summary, a single-atomic iron catalyst (Fe-SASC) was developed for rapid and ultrasensitive POC detection of 2,4-D. As expected, Fe-SASC has excellent peroxidase-like activity and exceptional stability due to the maximum utilization of active metal atoms and the structural mimicry of the active sites of natural enzyme. The Fe-SASC with high POD-like activity can trigger the colorimetric reaction of the chromogenic substrate to enhance the signal intensity, thus greatly improving the detection performance of LFIA. High-performance detection of 2,4-D with a low detection limit (0.82 ng/mL), wide detection range (1-250 ng/mL), and good selectivity have been demonstrated. Furthermore, the proposed Fe-SASC-LFIA exhibited high specificity and satisfactory recovery. The excellent detection abilities are sustained in the real human urine samples, further demonstrating its potential POC practicability.

REFERENCES

1. J. Deng, M. Yang, J. Wu, W. Zhang, X. Jiang, A Self-contained chemiluminescent lateral flow assay for point-of-care testing, Analytical Chemistry, 90 (2018) 9132-9137.

2. G.A. Posthuma-Trumpie, J. Korf, A. van Amerongen, Lateral flow (immuno) assay: its strengths, weaknesses, opportunities and threats. A literature survey, Analytical and Bioanalytical Chemistry, 393 (2009) 569-582.

3. C. Parolo, A. de la Escosura-Muñiz, A. Merkoçi, Enhanced lateral flow immunoassay using gold nanoparticles loaded with enzymes, Biosensors and Bioelectronics, 40 (2013) 412-416.

4. X. Niu, X. Li, Z. Lyu, J. Pan, S. Ding, X. Ruan, W. Zhu, D. Du, Y. Lin, Metal-organic framework based nanozymes: promising materials for biochemical analysis, Chemical Communications, 56 (2020) 11338-11353.

5. J. Wu, X. Wang, Q. Wang, Z. Lou, S. Li, Y. Zhu, L. Qin, H. Wei, Nanomaterials with enzyme-like characteristics (nanozymes): next-generation artificial enzymes (II), Chemical Society Reviews, 48 (2019) 1004-1076.

6. 6. D. Duan, K. Fan, D. Zhang, S. Tan, M. Liang, Y. Liu, J. Zhang, P. Zhang, W. Liu, X. Qiu, G.P. Kobinger, G. Fu Gao, X. Yan, Nanozyme-strip for rapid local diagnosis of Ebola, Biosensors and Bioelectronics, 74 (2015) 134-141.

7. N. Cheng, Y. Song, M.M. Zeinhom, Y.-C. Chang, L. Sheng, H. Li, D. Du, L. Li, M.-J. Zhu, Y. Luo, Nanozyme-mediated dual immunoassay integrated with smartphone for use in simultaneous detection of pathogens, ACS Applied Materials & Interfaces, 9 (2017) 40671-40680.

8. X. Ruan, Y. Wang, E.Y. Kwon, L. Wang, N. Cheng, X. Niu, S. Ding, B.J. Van Wie, Y. Lin, D. Du, Nanomaterial-enhanced 3D-printed sensor platform for simultaneous detection of atrazine and acetochlor, Biosensors and Bioelectronics, 184 (2021) 113238.

9. Q. Fu, H. Saltsburg, M. Flytzani-Stephanopoulos, Active nonmetallic Au and Pt species on ceria-based water-gas shift catalysts, Science, 301 (2003) 935-938.

10. B. Qiao, A. Wang, X. Yang, L.F. Allard, Z. Jiang, Y. Cui, J. Liu, J. Li, T. Zhang, Single-atom catalysis of CO oxidation using Pt_1/FeO_x, Nature Chemistry, 3 (2011) 634-641.

11. S. Ji, Y. Chen, X. Wang, Z. Zhang, D. Wang, Y. Li, Chemical synthesis of single atomic site catalysts, Chemical Reviews, 120 (2020) 11900-11955.

12. C. Zhu, S. Fu, Q. Shi, D. Du, Y. Lin, Single-atom electrocatalysts, Angewandte Chemie International Edition, 56 (2017) 13944-13960.

13. X.-F. Yang, A. Wang, B. Qiao, J. Li, J. Liu, T. Zhang, Single-atom catalysts: a new frontier in heterogeneous catalysis, Accounts of Chemical Research, 46 (2013) 1740-1748.

14. L. Huang, J. Chen, L. Gan, J. Wang, S. Dong, Single-atom nanozymes, Science Advances, 5 (2019) eaav5490.

15. S. Ding, Z. Lyu, L. Fang, T. Li, W. Zhu, S. Li, X. Li, J.-C. Li, D. Du, Y. Lin, Single-atomic site catalyst with heme hnzymes-like active sites for electrochemical sensing of hydrogen peroxide, Small, 17 (2021) 2100664.

16. N. Cheng, J.C. Li, D. Liu, Y. Lin, D. Du, Single-atom nanozyme based on nanoengineered Fe–N–C catalyst with superior peroxidase-like activity for ultrasensitive bioassays, Small, 15 (2019) 1901485.

17. X. Niu, Q. Shi, W. Zhu, D. Liu, H. Tian, S. Fu, N. Cheng, S. Li, J.N. Smith, D. Du, Unprecedented peroxidase-mimicking activity of single-atom nanozyme with atomically

dispersed Fe-N$_x$ moieties hosted by MOF derived porous carbon, Biosensors and Bioelectronics, 142 (2019) 111495.

18. M. Lefèvre, E. Proietti, F. Jaouen, J.-P. Dodelet, Iron-based catalysts with improved oxygen reduction activity in polymer electrolyte fuel cells, Science, 324 (2009) 71.

19. J. Liu, Y. Cai, R. Song, S. Ding, Z. Lyu, Y.-C. Chang, H. Tian, X. Zhang, D. Du, W. Zhu, Y. Zhou, Y. Lin, Recent progress on single-atom catalysts for CO$_2$ electroreduction, Materials Today, (2021).

20. L. Jiao, H. Yan, Y. Wu, W. Gu, C. Zhu, D. Du, Y. Lin, When nanozymes meet single-atom catalysis, Angewandte Chemie, 132 (2020) 2585-2596.

21. 21. W. Wu, L. Huang, E. Wang, S. Dong, Atomic engineering of single-atom nanozymes for enzyme-like catalysis, Chemical Science, 11 (2020) 9741-9756.

22. L. Jiao, W. Xu, Y. Wu, H. Yan, W. Gu, D. Du, Y. Lin, C. Zhu, Single-atom catalysts boost signal amplification for biosensing, Chemical Society Reviews, 50 (2021) 750-765.

23. Z. Lyu, S. Ding, N. Zhang, Y. Zhou, N. Cheng, M. Wang, M. Xu, Z. Feng, X. Niu, Y. Cheng, C. Zhang, D. Du, Y. Lin, Single-atom nanozymes linked immunosorbent assay for sensitive detection of Aβ1-40: a biomarker of Alzheimer's disease, Research, 2020 (2020) 4724505.

24. X. Cai, S. Ding, Q. Shi, Z. Lyu, D. Liu, W.-j. Dong, M. Du, P. Dutta, Y. Song, D. Du, Eyeball-Like yolk-shell bimetallic nanoparticles for synergistic photodynamic-photothermal therapy, ACS Applied Bio Materials, 3 (2020) 5922-5929.

25. E.Y. Liu, S. Jung, H. Yi, Improved Protein Conjugation with Uniform, Macroporous Poly(acrylamide-co-acrylic acid) hydrogel microspheres via EDC/NHS chemistry, Langmuir, 32 (2016) 11043-11054.

26. Q. Yan, H.-N. Zheng, C. Jiang, K. Li, S.-J. Xiao, EDC/NHS activation mechanism of polymethacrylic acid: anhydride versus NHS-ester, RSC Advances, 5 (2015) 69939-69947.

27. S. Fu, C. Zhu, D. Su, J. Song, S. Yao, S. Feng, M.H. Engelhard, D. Du, Y. Lin, Porous carbon-hosted atomically dispersed iron-nitrogen moiety as enhanced electrocatalysts for oxygen reduction reaction in a wide range of pH, Small, 14 (2018) 1703118.

28. R. Jiang, L. Li, T. Sheng, G. Hu, Y. Chen, L. Wang, Edge-site engineering of atomically dispersed Fe-N$_4$ by selective C-N bond cleavage for enhanced oxygen reduction reaction activities, Journal of the American Chemical Society, 140 (2018) 11594-11598.

29. S. Ding, Z. Lyu, H. Zhong, D. Liu, E. Sarnello, L. Fang, M. Xu, M.H. Engelhard, H. Tian, T. Li, X. Pan, S.P. Beckman, S. Feng, D. Du, J.-C. Li, M. Shao, Y. Lin, An ion-imprinting Derived strategy to synthesize single-atom iron electrocatalysts for oxygen reduction, Small, 17 (2021) 2004454.

30. Z. Lyu, S. Ding, M. Wang, X. Pan, Z. Feng, H. Tian, C. Zhu, D. Du, Y. Lin, Iron-imprinted single-atomic site catalyst-based nanoprobe for detection of hydrogen peroxide in living cells, Nano-Micro Letters, 13 (2021) 146.

31. G. Yang, S.Z.F. Phua, W.Q. Lim, R. Zhang, L. Feng, G. Liu, H. Wu, A.K. Bindra, D. Jana, Z. Liu, Y. Zhao, A hypoxia-responsive albumin-based nanosystem for deep tumor penetration and excellent therapeutic efficacy, Advanced Materials, 31 (2019) 1901513.

32. S. Liu, L. Dou, X. Yao, W. Zhang, M. Zhao, X. Yin, J. Sun, D. Zhang, J. Wang, Nanozyme amplification mediated on-demand multiplex lateral flow immunoassay with dual-readout and broadened detection range, Biosensors and Bioelectronics, 169 (2020) 112610.

33. J. Kong, L. Jiang, X. Su, J. Qin, Y. Du, B. Lin, Integrated microfluidic immunoassay for the rapid determination of clenbuterol, Lab on a Chip, 9 (2009) 1541-1547.

34. X. Wang, J. Yu, X. Wu, J. Fu, Q. Kang, D. Shen, J. Li, L. Chen, A molecular imprinting-based turn-on ratiometric fluorescence sensor for highly selective and sensitive detection of 2, 4-dichlorophenoxyacetic acid (2, 4-D), Biosensors and Bioelectronics, 81 (2016) 438-444.

35. K.V. Gobi, H. Tanaka, Y. Shoyama, N. Miura, Highly sensitive regenerable immunosensor for label-free detection of 2, 4-dichlorophenoxyacetic acid at ppb levels by using surface plasmon resonance imaging, Sensors and Actuators B: Chemical, 111 (2005) 562-571.

36. Y. Wang, M.M. Zeinhom, M. Yang, R. Sun, S. Wang, J.N. Smith, C. Timchalk, L. Li, Y. Lin, D. Du, A 3D-printed, portable, optical-sensing platform for smartphones capable of detecting the herbicide 2, 4-dichlorophenoxyacetic acid, Analytical Chemistry, 89 (2017) 9339-9346.

37. H. Shi, G. Zhao, M. Liu, Z. Zhu, A novel photoelectrochemical sensor based on molecularly imprinted polymer modified TiO_2 nanotubes and its highly selective detection of 2, 4-dichlorophenoxyacetic acid, Electrochemistry Communications, 13 (2011) 1404-1407.

38. A. Vinayaka, S. Basheer, M. Thakur, Bioconjugation of CdTe quantum dot for the detection of 2, 4-dichlorophenoxyacetic acid by competitive fluoroimmunoassay based biosensor, Biosensors and Bioelectronics, 24 (2009) 1615-1620.

39. S.A. Haeri, S. Abbasi, Biocoacervation extraction combined with dispersive solid phase extraction using a reversed-phase core-shell magnetic molecularly imprinted sorbent for 2, 4-dichlorophenoxyacetic acid prior to its determination by HPLC, Journal of the Iranian Chemical Society, 13 (2016) 1993-1999.

40. X. Chen, H. Zhang, Y. Wan, X. Chen, Y. Li, Determination of 2, 4-Dichlorophenoxyacetic acid (2, 4-D) in rat serum for pharmacokinetic studies with a simple HPLC method, Plos One, 13 (2018) e0191149.

41. X.L. Hu, X.M. Wu, X. Fang, Z.J. Li, G.L. Wang, Switchable fluorescence of gold nanoclusters for probing the activity of alkaline phosphatase and its application in immunoassay, Biosensors and Bioelectronics, 77 (2016) 666-672.

42. M. Janyasupab, C.-W. Liu, N. Chanlek, S. Chio-Srichan, C. Promptmas, W. Surareungchai, A comparative study of non-enzymatic glucose detection in artificial human urine and human urine specimens by using mesoporous bimetallic cobalt-iron supported N-doped graphene biosensor based on differential pulse voltammetry, Sensors and Actuators B: Chemical, 286 (2019) 550-563.

SUMMARY

Cost-effective biosensors with outstanding specificity and sensitivity to test environmental contaminants, control human biologic processes, and assess precise health diagnoses have been intensively studied and have good potential for the advantages such as simple, scalable, and efficient in the fabrication process. However, the natural enzyme used in biosensors suffers from disadvantages such as low stability, poor robustness, and high cost. Using single atom site catalysts in biosensors has been regarded as an effective way to solve the limitations of natural enzymes and can achieve the aforementioned detection goal. In this dissertation, we synthesized different kinds of SASC and used them for detecting different analytes with satisfactory detection performance.

Firstly, a Fe-based single-atomic site catalyst was prepared through a facile ion-imprinting approach and used as a nanoprobe for hydrogen peroxide detection in living cells. Results show that the synthesized SASC possesses abundant Fe-N_x single-atomic sites, which can mimic the active center structure of natural HRP. Herein, the ion imprinting process can precisely control ions at the atomic level, resulting in the formation of large quantities of well-defined monoatomic iron during the pyrolysis process. Results show that SASC had an excellent peroxidase-like activity. High sensitivity and specificity of nanoprobe have been achieved for colorimetric detection of H_2O_2 in living cells. This work proved that the Fe-N-C SASC could structurally mimic the active site of natural HRP, thus opening a novel and easy route in designing advanced SASC used as nanoprobes and expanding their biosensing applications.

The activity site density of SASC is an important factor affecting the enzyme-like activity. To further increase enzyme-like activity, we used a nanoconfinement strategy to increase the Fe-N_x active site density in the matrix. Herein, manganese oxide was coated on the surface of the

112

processor, thus the nanoconfinement effect was introduced in the pyrolysis process. The obtained Fe-N$_x$ SASC possessed outstanding peroxidase-mimicking activity, showing high activity and excellent robustness against harsh environments. Most importantly, novel Fe-N$_x$ SASC was applied as the HRP replacement in ELISA to enhance the detection performance of Aβ1-40, exhibiting an ultralow sensitivity that met the requirement of effective detection of Aβ1-40. we believe this kind of peroxidase-like SASC will show great potential and pave a new way to design a novel ELISA kit with improved sensitivity for detecting various target biomarkers in real human samples.

It is well known that the more active sites exposed on the surface, the easier for them to participate in the reaction, and the better activity can be obtained. Hence, a 2D Fe-SASC catalyst was successfully synthesized with excellent peroxidase-mimicking activity, mainly attributed to the 2-dimensional structure to expose more single-atom sites on the surface. Such structure design achieves the aim of continuously increasing the peroxidase-like activity. Besides, using 2D Fe-SASC in competitive ELISA achieves a satisfactory detection performance 2,4-D with high sensitivity and wide detection range, showing great potential in designing compactivity ELISA kits with improved sensitivity for detecting various target biomarkers.

Finally, a single-atomic iron site catalyst (Fe-SASC) was developed through precisely structural control of the active sites of natural enzyme and used for rapid and ultrasensitive point-of-care detection of herbicide via lateral-flow immunoassay. High-performance detection of 2,4-D with a low detection limit, wide detection range, and good selectivity has been demonstrated. The excellent detection abilities are sustained in the real human urine samples, demonstrating potential POC practicability.

In the future, it is believed that effective synthesis methods and advanced strategies can continue to design the various Fe-N-C SASCs with excellent enzyme-like activity. The unique structure and special properties will endow them exhibit outstanding biosensing performance. Also, the newly developed enzyme-like SASC will lead to a significant leap in the combined efforts in different research fields, which will provide more personalized disease diagnosis and treatment opportunities and high-precision biosensors and nanoprobes.

APPENDIX

APPENDIX A

Acronyms and Abbreviations

SASCs	Single-atomic site catalysts
HRP	Horseradish peroxidase
IIT	Ion-imprinting technology
NIM	Non-imprinted nanomaterial
IIM-Fe-SASC	Fe-based single-atomic site catalyst
A-Tri-EOS	[3-(2-Aminoethylamino)propyl]trimethoxysilane
CTAB	Cetyltrimethylammonium bromide
TEOS	Tetraethyl orthosilicate
SCN^-	Thiocyanate ions
TA	Terephthalic acid
UA	Uric acid
ADP	Adenosine-5-diphosphate
fMLP	N-formylmethionyl-leucyl-phenylalanine
PMA	Phorbol-12-myristate-13-acetate
MeIM	2-Methylimidazole
BSA	Bovine serum albumin
H_2O_2	Hydrogen peroxide
TMB	3,3′,5,5′-tetramethylbenzidine
ABTS	2,2′-azino-bis (3-ethylbenzothiazoline-6-sulfonic acid)
ALP	Alkaline phosphatase
OPD	1,2-diaminobenzene

ELISA	Enzyme-linked immunosorbent assay
LFIA	Lateral-flow immunoassay
POC	Point-of-care
AD	Alzheimer's Disease
Aβ 1-40	Amyloid beta 1-40
SA	Streptavidin
SASC-LISA	SASCs-linked immunosorbent assay
LOD	Limit of detection
EDC	N-(3-dimethylaminopropyl)-N′-ethylcarbodiimide hydrochloride
NHS	N-hydroxysuccinimide
FePc	iron (II) phthalocyanine
2,4-D BSA	2,4-Dichlorophenoxyacetic acid antigen
ROS	Reactive oxygen species
NC	Nitrocellulose
TEM	Transmission electron microscopy
APS	Advanced Photon Source
XRD	X-ray diffraction
STEM	Scanning TEM
HAADF-STEM	Aberration-corrected high-angle annular dark-field STEM
HAADF-STEM	High-angle annular dark-field STEM
HRTEM	High-resolution TEM
BF-STEM	Bright-field scanning TEM
EDS	Energy-dispersive X-ray spectroscopy

XAS	X-ray absorption spectroscopy
XANES	X-ray absorption near edge structure
EXAFS	X-ray absorption fine structure
FT	Fourier-transformed
XPS	X-ray photoelectron spectroscopy
BET	Brunauer-Emmett-Teller
NLDFT	Nonlocal density functional theory
WT	Wavelet transform
SAED	Selected area electron diffraction

APPENDIX B

Publications

1. **Zhaoyuan Lyu,** Shichao Ding, Maoyu Wang, Xiaoqing Pan, Zhenxing Feng, Hangyu Tian, Chengzhou Zhu, Dan Du, Yuehe Lin[*]. Iron-imprinted single-atomic site catalyst-based nanoprobe for detection of hydrogen peroxide in living cells. *Nano-Micro Letters*, 2021, 13: 146.

2. **Zhaoyuan Lyu,** Shichao Ding, Nan Zhang, Yang Zhou, Nan Cheng, Maoyu Wang, Mingjie Xu, Zhenxing Feng, Xiangheng Niu, Yuan Cheng, Chao Zhang, Dan Du, Yuehe Lin[*]. Single-Atom Nanozymes Linked Immunosorbent Assay for Sensitive Detection of Aβ 1-40: A Biomarker of Alzheimer's Disease. *Research*, 2020, 2020: 4724505.

3. **Zhaoyuan Lyu,** Shichao Ding, Dan Du, Kaiyan Qiu, Jin Liu, Xiao Zhang[*], Yuehe Lin[*]. Recent advances in biomedical applications of 2D nanomaterials with peroxidase-like properties. *Advanced Drug Delivery Reviews*. 2022, 185, 114269.

4. **Zhaoyuan Lyu**, Shichao Ding, Peter Tieu, Lingzhe Fang, Xin Li, Tao Li, Xiaoqing Pan, Mark H. Engelhard, Xiaofan Ruan, Dan Du[*], Suiqiong Li[*], Yuehe Lin[*]. Single-Atomic Site Catalyst Enhanced Lateral-flow Immunoassay for Detection of 2,4-Dichlorophenoxyacetic Acid. *Submitted*.

5. Shichao Ding, **Zhaoyuan Lyu[#], (Co-first author)** Erik Sarnello, Mingjie Xu, Lingzhe Fang, Hangyu Tian, Sam Ellery Karcher, Tao Li, Xiaoqing Pan, John McCloy, Guodong Ding, Qiang Zhang, Qiurong Shi, Dan Du, Jin-Cheng Li[*], Xiao Zhang[*], Yuehe Lin[*].A MnO$_x$ enhanced atomically dispersed iron-nitrogen-carbon catalyst for the oxygen reduction reaction. *Journal of Materials Chemistry A*, 2022, 10, 5981-5989.

6. Shichao Ding, Nan Zhang, **Zhaoyuan Lyu[#], (Co-first author)** Zhaoyuan Lyu, Wenlei Zhu, Yu-Chung Chang, Xiaoling Hu, Dan Du, Yuehe Lin[*]. Protein-based nanomaterials and nanosystems for biomedical applications: A review. ***Materials Today***, 2021, 43:166-184.

7. Shichao Ding, **Zhaoyuan Lyu[#], (Co-first author)** Xiangheng Niu, Yang Zhou, Dong Liu, Mojtaba Falahati, Dan Du, Yuehe Lin[*]. Integrating ionic liquids with molecular imprinting technology for biorecognition and biosensing: A review. ***Biosensors and Bioelectronics***, 2020, 149: 111830.

8. Shichao Ding, **Zhaoyuan Lyu**, Lingzhe Fang, Tao Li, Wenlei Zhu, Suiqiong Li, Xin Li, Jin-Cheng Li[*], Dan Du[*], Yuehe Lin[*]. Single-Atomic Site Catalyst with Heme Enzymes-Like Active Sites for Electrochemical Sensing of Hydrogen Peroxide. ***Small***, 2021, 17(25): 2100664.

9. Shichao Ding, **Zhaoyuan Lyu**, Hong Zhong, Dong Liu, Erik Sarnello, Lingzhe Fang, Mingjie Xu, Mark H Engelhard, Hangyu Tian, Tao Li, Xiaoqing Pan, Scott P Beckman, Shuo Feng, Dan Du, Jin-Cheng Li[*], Minhua Shao, Yuehe Lin[*]. An Ion-Imprinting Derived Strategy to Synthesize Single-Atom Iron Electrocatalysts for Oxygen Reduction. ***Small***, 2021, 17(16): 2004454.

10. Shichao Ding, **Zhaoyuan Lyu**, Suiqiong Li, Xiaofan Ruan, Mingen Fei, Yang Zhou, Xiangheng Niu, Wenlei Zhu, Dan Du, Yuehe Lin[*]. "Molecularly imprinted polypyrrole nanotubes based electrochemical sensor for glyphosate detection." ***Biosensors and Bioelectronics***, 2021, 191: 113434.

11. Chenxi Huyan, Shichao Ding, **Zhaoyuan Lyu**, Mark H Engelhard, Yuhao Tian, Dan Du, Dong Liu[*], Yuehe Lin[*]. Selective Removal of Perfluorobutyric Acid Using an

Electroactive Ion Exchanger Based on Polypyrrole@ Iron Oxide on Carbon Cloth. *ACS Applied Materials & Interfaces*, 2021, 13(41): 48500.

12. Xiangheng Niu, Xin Li, **Zhaoyuan Lyu**, Jianming Pan, Shichao Ding, Xiaofan Ruan, Wenlei Zhu, Dan Du, Yuehe Lin[*]. Metal-organic framework based nanozymes: promising materials for biochemical analysis. *Chemical Communications*, 2020, 56(77): 11338.

13. Mansour Mahmoudpour, Shichao Ding, **Zhaoyuan Lyu**, Ghasem Ebrahimi, Dan Du, Jafar Ezzati Nazhad Dolatabadi[*], Mohammadali Torbati[*], Yuehe Lin[*]. Aptamer functionalized nanomaterials for biomedical applications: Recent advances and new horizons. *Nano Today*, 2021, 39: 101177.

14. Xiaoli Cai, Shichao Ding, Qiurong Shi, **Zhaoyuan Lyu**, Dong Liu, Wen-ji Dong, Min Du, Prashanta Dutta, Yang Song[*], Dan Du[*], Yuehe Lin[*]. Eyeball-Like Yolk–Shell Bimetallic Nanoparticles for Synergistic Photodynamic-Photothermal Therapy. *ACS Applied Bio Materials*, 2020, 3(9): 5922.

15. Dong Liu, Jin-Cheng Li, Shichao Ding, **Zhaoyuan Lyu**, Shuo Feng, Hangyu Tian, Chenxi Huyan, Mingjie Xu, Tao Li, Dan Du, Peng Liu, Minhua Shao, Yuehe Lin*. 2D Single-Atom Catalyst with Optimized Iron Sites Produced by Thermal Melting of Metal–Organic Frameworks for Oxygen Reduction Reaction. *Small Methods*, 2020, 4(6): 1900827.

16. Juan Liu, Yanming Cai, Rongbin Song, Shichao Ding, **Zhaoyuan Lyu**, Yu-Chung Chang, Hangyu Tian, Xiao Zhang, Dan Du, Wenlei Zhu[*], Yang Zhou[*], Yuehe Lin[*]. Recent progress on single-atom catalysts for CO_2 electroreduction. *Materials Today*, 2021, 48: 95.

17. Shichao Ding, Aminul Islam Khan, Xiaoli Cai, Yang Song, **Zhaoyuan Lyu**, Dan Du, Prashanta Dutta, Yuehe Lin[*]. Overcoming blood-brain barrier transport: Advances in nanoparticle-based drug delivery strategies. *Materials Today*, 2020, 37: 112.

18. Dong Liu, Jin-Cheng Li, Qiurong Shi, Shuo Feng, **Zhaoyuan Lyu**, Shichao Ding, Leiduan Hao, Qiang Zhang, Chenhui Wang, Mingjie Xu, Tao Li, Erik Sarnello, Dan Du, Yuehe Lin*. Atomically isolated iron atom anchored on carbon nanotubes for oxygen reduction reaction. *ACS Applied Materials & Interfaces*, 2019, 11(43): 39820.

19. Xiaofan Ruan, Victoria Hulubei, Yijia Wang, Qiurong Shi, Nan Cheng, Limin Wang, **Zhaoyuan Lyu**, William C Davis, Jordan N Smith, Yuehe Lin, Dan Du[*]. Au@PtPd enhanced immunoassay with 3D printed smartphone device for quantification of diaminochlorotriazine (DACT), the major atrazine biomarker. *Biosensors and Bioelectronics*, 2022, 208, 114190.

20. Hangyu Tian, Wenlei Zhu, Qiurong Shi, Shichao Ding, **Zhaoyuan Lyu**, Mingjie Xu, Xiaoqing Pan, Mark H Engelhard, Dan Du, Yuehe Lin[*]. Bimetallic Ir_xPb nanowire networks with enhanced electrocatalytic activity for oxygen evolution reaction. *Journal of Materials Chemistry A*, 2022, DOI: 10.1039/D2TA00870J.

21. Jin-Cheng Li, Xueping Qin, Fei Xiao, Caihong Liang, Mingjie Xu, Yu Meng, Erik Sarnello, Lingzhe Fang, Tao Li, Shichao Ding, **Zhaoyuan Lyu**, Shangqian Zhu, Xiaoqing Pan, Peng-Xiang Hou, Chang Liu[*], Yuehe Lin[*], Minhua Shao[*]. Highly dispersive cerium atoms on carbon nanowires as oxygen reduction reaction electrocatalysts for Zn-air batteries. *Nano Letters*, 2021, 21, 4508-4515.

22. Mojtaba Falahati, Parvaneh Ahmadvand, Shahriar Safaee, Yu-Chung Chang, **Zhaoyuan Lyu**, Roland Chen[*], Lei Li[*], Yuehe Lin[*]. Smart polymers and nanocomposites for 3D and 4D printing. *Materials Today*, 2020, 40, 215-245.

23. Jin-Cheng Li, Hong Zhong, Mingjie Xu, Tao Li, Liguang Wang, Qiurong Shi, Shuo Feng, **Zhaoyuan Lyu**, Dong Liu, Dan Du, Scott P Beckman, Xiaoqing Pan, Yuehe Lin[*], Minhua Shao[*]. Boosting the activity of Fe-N$_x$ moieties in Fe-NC electrocatalysts via phosphorus doping for oxygen reduction reaction. *Science China Materials*, 2020, 63, 965-971.